Study of unconventional compensated spin structures and textures towards unmatched spintronics properties

Miina Leiviska

THÈSE

Pour obtenir le grade de

DOCTEUR DE L'UNIVERSITÉ GRENOBLE ALPES

École doctorale : PHYS - Physique
Spécialité : Nanophysique
Unité de recherche : Spintronique et Technologie des Composants

Étude de structures et de textures de spin compensées non-conventionnelles en vue d'obtenir des propriétés spintroniques inégalées

Study of unconventional compensated spin structures and textures towards unmatched spintronics properties

Présentée par :

Miina LEIVISKA

Direction de thèse :

Vincent BALTZ — Directeur de thèse
CHARGE DE RECHERCHE HDR, CNRS DELEGATION ALPES

Rapporteurs :

AURELIEN MANCHON
PROFESSEUR DES UNIVERSITES, AIX-MARSEILLE UNIVERSITE
YOSHICHIKA OTANI
FULL PROFESSOR, THE UNIVERSITY OF TOKYO

Thèse soutenue publiquement le **11 septembre 2023**, devant le jury composé de :

AURELIEN MANCHON PROFESSEUR DES UNIVERSITES, AIX-MARSEILLE UNIVERSITE	Rapporteur
YOSHICHIKA OTANI FULL PROFESSOR, THE UNIVERSITY OF TOKYO	Rapporteur
TOMAS JUNGWIRTH FULL PROFESSOR, The University of Nottingham	Examinateur
RICHARD EVANS ASSOCIATE PROFESSOR, YORK UNIVERSITY	Examinateur
JEAN-PHILIPPE ATTANE PROFESSEUR DES UNIVERSITES, UNIVERSITE GRENOBLE ALPES	Examinateur
STEFANIA PIZZINI DIRECTEUR DE RECHERCHE, CNRS DELEGATION ALPES	Présidente

Acknowledgements

Finishing this manuscript marks the end of my three-year doctoral journey that would not have been possible without the input of various people. First, however, I would like to acknowledge the journey itself. During these three years I have not only acquired new knowledge on physics and magnetism but also learnt valuable lessons on the non-linearity of research (arriving from a plan to meaningful results will definitely involve both downhills and uphills) and the impermanence of challenges (one day of measuring unclear data does not mean three years of measuring unclear data). I hope that these lessons will serve me also in my future path.

I would like to thank my supervisor, Vincent Baltz, for giving me the opportunity to take on this exciting PhD project, for guiding me through it with patience (even at the occasion of broken sample holders), and for always being available for questions and assistance. I've learnt a lot from your meticulous and thorough way of conducting research and I hope to be able to follow your example in the future, too. I would also like to thank Rafael Lopes Seeger, from whom I inherited this project, for spending countless hours teaching me the secrets and quirks of the spin pumping set-up as well as other aspects of experimental work.

Next, I would like to thank Daria Gusakova and Richard Evans, who also kindly hosted me for some weeks at the University of York, for their support and guidance in the simulation work and for repeatedly helping me get unstuck. Moreover, our experimental work would not have been possible without the supply of high-quality samples from Patrick Warin here at SPINTEC and the team of Lisa Michez at CINaM, or without the technical support from Isabelle Joumard on the various set-ups used and from Serge Gambarelli, Christian Lombard, and Vincent Maurel from SYMMES-lab on the spin pumping set-up. A special thanks also to Jean-François Jacquot who introduced me to the delicate world of the SQUID magnetometer.

I would also like to thank my jury: Aurélien Manchon, YoshiChika Otani, Tomáš Jungwirth, Richard Evans, Jean-Philippe Attané, and Stefania Pizzini for taking the time to read this manuscript.

During these three years I had also a pleasure of interacting with various external collaborators, whose input helped me progress considerably. First, I would like to thank everyone in the Mn_5Si_3 collaboration for the active discussions and regular feedback during the monthly meetings, with a special mention to Helena Reichlová for inviting me to share my work at various workshops and conferences. Second, I would like to thank Prof. Yasuhiro Niimi and Mori Watanabe for the fruitful discussions on spin fluctuations, for the ongoing efforts on advancing the PdNi project, and for hosting me for a couple of days at the University of Osaka.

I also want to acknowledge the administration team Adriana Stoenescu, Catherine Broisin, Céline Bellavia, and Sandra Ingrassia, and thank them for their patience with all the administrative work that allowed me to even begin this doctoral work and also to visit many places in the framework of my research.

A big part of why this PhD journey was so memorable and meaningful are my fellow voyagers both at and outside SPINTEC. I want to thank Samuel, with whom I shared an office and an apartment, for making every day a bit more fun; Aurélie for being the best possible partner for sharing the super fun 6:30am workouts; Alvaro for pulling me into the rabbit hole that is crossfit; Javi for all the scientific and non-scientific discussions, and for being the designated social activity coordinator; everyone who was part of the train crew when travelling to conferences around Europe; and for everyone who was there along the way during the board game evenings, climbing sessions, house parties, and extended lunch breaks.

Finally, I would like to thank my family for their endless support and endless efforts in trying to understand what exactly it is that I am doing. On the same note, I'm grateful to my chosen family of dear friends (a special shout-out to Hendrik, Gwen, Jenna, Adèle, Genevieve, and Roosa) who have been there for me through thick and thin.

Contents

Introduction

The field of spintronics explores phenomena relating to the spin degree of freedom of electrons. The spin refers to the intrinsic angular momentum an electron carries, giving rise to the intrinsic magnetic moment of an electron. Understanding the behavior of the electron spins (e.g. transport, dynamics, relaxation) plays a central role in both fundamental studies focusing on comprehending the quantum nature of matter and in the search for practical applications where manipulating spins and the emerging magnetisation are of interest. The work presented in this thesis is in the realm of fundamental research but in order to place the thesis in the context of societal relevance as well as highlight the importance of fundamental research in arriving at practical applications, we will begin with an overview of the spintronic applications and how they materialized from basic research on spintronic properties.

Currently, one of the main promises spintronics holds is in the domain of information technology [5]. This promise is founded on the spintronic devices called *spin valves*, comprising of two ferromagnetic layers separated by a non-magnetic layer as illustrated in Figure 1. The resistance across these heterostructures depends on the relative orientation of the two magnetic layers (parallel or antiparallel) - an effect referred to as giant magnetoresistance (GMR) when the non-magnetic layer is metallic and tunneling magnetoresistance (TMR) when it is insulating. The GMR effect was discovered in the late 1980s by the groups of Albert Fert [6] and Peter Grünberg [7] who were independently studying the transport properties of magnetic multilayers. The TMR effect, on the other hand, was first demonstrated by Michel Jullière [8] and later the strength of the effect was greatly improved upon through careful material optimization [9][10][11].

In contemporary devices the insulating barrier and thus TMR is more commonly utilized as the resistance change can exceed that by GMR by an order of magnitude. Such devices are commonly referred to as magnetic tunnel junctions (MTJ) and they have a number of practical applications owing to their two states distinguished by resistivity. First, these devices can be used to store information, as the state (0 - antiparallel, 1 - parallel) can be read utilising TMR and written utilising the torque from a spin-polarized current [12]. This is the operating principle of magnetic random access memories (MRAMs), which are not only non-volatile and more scalable but can also operate faster and with lower power than many of the competing RAMs [13]. Second, MTJs can also act as magnetic field sensors as fields inflict changes to the state of the MTJ, which then translates to

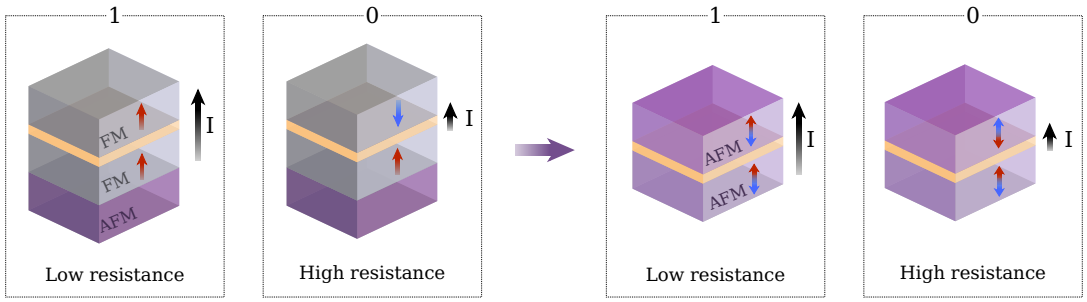

Figure 1: Operation principle of spin valves - two magnetic layers separated by a non-magnetic layer show two resistance states depending on their relative magnetisation orientations. In contemporary applications of spin valves, the magnetic layers are ferromagnetic but due to the limitations caused by the net magnetisation there is a strong drive in replacing the ferromagnets with compensated magnets.

a resistance change. This effect is employed for example in the read heads of hard drive disks.

The discovery of GMR is often referred to as the beginning of the field of spintronics, but this discovery was preceded by decades of fundamental research on spin-dependent transport. For example, spin-dependence of the electron scattering in ferromagnetic materials was proposed by Mott [14] and experimentally demonstrated by Fert and Campbell already in the 1960s [15], while the spin-polarization of a current passing through a ferromagnet and spin-dependent tunneling were a subject of various works in 1970s [16][17][18][19]. In addition to this, the theory of the two important spin transport effects playing a central role in today's spintronics research, namely the anomalous Hall Effect (AHE) and spin Hall effect (SHE), were predicted in the 1950s [20] and 1970s [21], respectively. In AHE, a longitudinal spin polarized current is converted to a transversal spin polarized current, while in SHE a charge-to-spin conversion takes place as a longitudinal charge current generates a transversal pure spin current. SHE (and its reciprocal effect) is not only a powerful tool for studying the spin transport properties of various materials but also a critical ingredient of spin-orbit torque [22][23], which in the recent decade has emerged as a contender for the writing mechanism of MRAMs among other applications [24].

Until recently, the headliner of spintronics has largely been ferromagnetic materials, in which the effects described above were first demonstrated. However, the use of ferromagnets poses certain limits to the development of the field of spintronics in terms of stability, scalability, and operational speed. The main drawback is the consequences of the net magnetisation: the magnetic states are vulnerable to external field perturbations, and stray fields can cause cross-talk between the bits when increasing the storage density. Naturally, the removal of these obstacles would require the use of materials with zero net magnetisation. Moreover, the dynamics of ferromagnets are in the GHz range, which limits the writing speed. Antiferromagnets, predicted by Louis Néel in 1930s [25] and experimentally confirmed in 1950s [26], comprise of (minimum) two sublattices with

opposite magnetisation orientations and therefore fulfill this criteria. However, when it comes to the lack of net magnetisation the other side of the coin is that controlling the order parameter for example with external fields becomes more challenging. Moreover, the spatial symmetries of antiferromagnets render their band structure spin-degenerate so that writing and reading their state appeared elusive, resulting in general impression that antiferromagnets are unsuitable as an active component of spintronic applications. As a passive component, however, antiferromagnets have found use as a pinning layer of MTJs, ensuring that only one of the magnetic layers switches upon writing [27]. This layer is also included in Figure 1.

The recent decade has witnessed a considerable research efforts in identifying ways for manipulating and probing the antiferromagnetic order [28][29]. This search was driven not only by the advantages of vanishing net magnetisation but also the dynamics of antiferromagnets being in the THz range compared to the GHz range of ferromagnetic dynamics. Antiferromagnets are also more abundant than ferromagnets and contain metallic, semiconducting, insulating, and superconducting compounds in their ranks. In order to demonstrate their viability as active spintronic components, however, a demonstration of electrical writing and reading of an antiferromagnetic state is necessary. To this end, relativistic effects turned out to be a fruitful path: current-induced switching of the antiferromagnetic order parameter can be realized through the generation of staggered spin-orbit fields [30][31] and the orientation of the order parameter can be read through the anisotropic magnetoresistance effect [32]. In addition to the electrical control, also optical [33][34] as well as strain [35] control of the antiferromagnetic order parameter has been demonstrated.

Another exciting avenue in the research on spintronic properties of compensated magnets is the discovery that the vanishing net magnetisation can coexist with a spin-split band structure [36][37][38][39]. This unconventional band structure originates from the lowered spatial symmetry of compensated magnets and allows many spintronic effects previously considered exclusive to ferromagnets to arise, such as AHE [36][40][41][42][43], GMR [44], and TMR [45][44][46][47], while also exhibiting novel properties like pure spin current generation [48][49][50], chiral magnons [51], and spin-triplet super currents [52]. The combination of these properties makes the discovery of these spin-split compensated magnets (dubbed as altermagnets in the collinear case, or chiral antiferromagnets in the non-collinear case) a springboard for further fundamental research on the different facets of their various properties (electrical, optical, thermal, mechanical) while maintaining the vision of spintronic devices composed of compensated magnets only. An MTJ based on compensated magnets playing the active role is illustrated in Figure 1, and excitingly, experimental demonstrations of the viability of such a device were recently provided by both Quin *et al.* [47] and Chen *et al.* [46].

The focus of this thesis is the understanding of the spintronic properties and their nuances in compensated magnets. More specifically, we will study how the global spin

structures and local spin textures affect these properties through their symmetries. For this purpose, we will utilize both experimental techniques that probe magnetic and magnetotransport properties as well as numerical methods that capture the evolution of (compensated) magnetic states under various conditions. The structure of the thesis is as follows:

Chapter 1 discusses the emergence of the spin-splitted band structure in collinear, compensated magnets (or altermagnets) and how this allows for novel magnetotransport properties to arise. We will consider the epitaxial Mn_5Si_3 films, which are predicted to have the correct symmetry for the spin-split, compensated phase. We show that the magnetotransport properties of these films are agree with the predicted phase. We will especially highlight the intrinsic anisotropy of these properties. In addition to this, we will explore indirect, electrical methods for gaining information about the antiferromagnetic order parameter orientation and dynamics. To this end, we will use methods developed for ferromagnets, which so far have not been applied to compensated magnets.

Chapter 2 shifts the focus from compensated magnets with spin-split bands (altermagnets) to those with spin-degenerate bands (antiferromagnets) and from global spin structures to localized spin textures. Using numerical methods, we demonstrate how topological spin textures can be imprinted from a ferromagnet to an antiferromagnet during a thermal cycling procedure, thus realizing the experimentally elusive nucleation of compensated, localised spin textures. We will discuss the properties of these imprinted spin textures in terms of their field-stability, topological and microscopic nature, and dependence on material parameters.

Chapter 3 is dedicated to the description of a powerful experimental tool for spin transport studies, namely ferromagnetic resonance induced spin pumping. We explain the operational principle of this tool and how it can be applied to probing of both linear and non-linear spin susceptibilities and their anomalous behavior across phase transitions, relating to spin fluctuations. We then apply this tool on the phase transitions in $Pd_{1-x}Ni_x$ thin films, which show complex magnetic behaviour with features indicative of irreversibility and frustration. We will also characterize the structural, magnetic, and magnetotransport properties of these films in search of a better understanding of their magnetic phase. The intention of this Chapter is to demonstrate and optimize this experimental method for future studies on spin transport in compensated magnets.

Conclusion summarizes the findings presented in this thesis and draws some general conclusions on how this thesis adds to the increasing efforts of pushing the boundaries of spintronics beyond ferromagnets.

Chapter 1

Anisotropic anomalous Hall effect in the unconventional compensated d-wave magnet candidate Mn_5Si_3 films [1][2][3]

In this Chapter, we will introduce a candidate material for the new emerging group of collinear compensated magnetic materials, dubbed as altermagnetism [39], where the macroscopic time-reversal symmetry is broken by the absence of translation and inversion symmetry operations. This material is Mn_5Si_3 in its epitaxial thin film format. The magnetotransport properties of these materials are strongly dependent on the relative orientation of the magnetic order parameter and the underlying crystal structure, and therefore show unique, anisotropic behavior, which will be discussed in detail here. We will also discuss how we can extract information about the static and dynamic properties of the magnetic order parameter through magnetotransport measurements by applying techniques developed for ferromagnets and previously considered inapplicable to compensated magnets.

The work presented in this Chapter is a result of a large collaboration between theoretical and experimental groups in France (SPINTEC Grenoble, CINaM Marseille), Germany (TU Dresden, JGU Mainz, Univ. of Konstanz), and Czech Republic (FZU Czech Academy of Sciences, Charles University) in the framework of the ANR and DFG grants. This work is a continuation on the results presented in the PhD thesis of Dr. Rafael Lopes Seeger [53], conducted in the AF spintronics team at SPINTEC. The contribution of our AF spintronics team is largely on the magnetic and magnetotransport measurements while the contributions from our collaborators on the work presented in this Chapter will be mentioned in connection with the relevant results.

The results presented here have been/will be reported in three separate publications. The optimization of the epitaxial Mn_5Si_3 thin film growth, led by the team of Prof. Lisa Michez in Aix-Marseille University, has been reported in the article:

- I. Kounta, H. Reichlova, D. Kriegner, R. Lopes Seeger, A. Badura, M. Leiviskä, A. Boussadi, V. Heresanu, S. Bertaina, M. Petit, E. Schmoranzerova, L. Smejkal, J. Sinova, T. Jungwirth, V. Baltz, S. Goennenwein, and L. Michez, *Competitive actions of MnSi in the epitaxial growth of Mn_5Si_3 thin films on Si(111)*, Phys. Rev. Materials 7, 024416, (2023).

The magnetic and magnetotransport properties of these films strongly akin to those expected for altermagnetic materials will be reported in the following articles:

- H. Reichlova, R. Lopes Seeger, R. Gonzalez-Hernandez, I. Kounta, R. Schlitz, D. Kriegner, P. Ritzinger, M. Lammel, M. Leiviskä, V. Petricek, P. Dolezal, E. Schmoranzerova, A. Badura, S. Bertaina, A. Thomas, V. Baltz, L. Michez, J. Sinova, S. Goennenwein, T. Jungwirth, and L. Smejkal, *Observation of a spontaneous anomalous Hall effect in acandidate material of an unconventional d-wave magnetic phase*, arxiv:2012.15651

- M. Leiviskä, R. Lopes Seeger, I. Kounta, H. Reichlova, A. Badura, J. Rial, S. Beckert, D. Kriegner, I. Joumard, E. Schmoranzerova, J. Sinova, T. Jungwirth, S. Goennenwein, L. Michez, L. Smejkal, H. Gomonay, and V. Baltz, *Anisotropic anomalous Hall effect in the unconventional compensated d-wave magnet candidate Mn_5Si_3 films*, in preparation

1.1 Symmetry tools for classifying matter

Symmetry is a powerful tool in condensed matter physics [54][55]. As Curie-Neumann's principle states, symmetries that apply to a structure of a crystal will also apply to its macroscopic properties, meaning that symmetry plays an important role in governing the physical properties of materials. Symmetry can also be used for classification purposes as each material can be described by a set of symmetry operations (operations that leave the material unchanged) that distinguishes it from other materials that have a different appearance and thus behaviour. In this Section, we will first introduce the various spatial symmetry operations that describe crystal structures and then move on to discussing the symmetries of magnetic ordering that also contain the time-reversal symmetry, which adds an important nuance to the classification of magnetic materials.

1.1.1 Classification based on crystal symmetry

Each crystal contains a set of *symmetry elements* (points, lines or planes) about which *symmetry operations* occur. Here we discuss the four basic symmetry elements: identity, mirror plane, axis of rotation, and centre of inversion, which are all illustrated in Figure 1.1a for the case of a simple square lattice.

Identity is the entire unit cell of the crystal and the corresponding symmetry operation is doing nothing to the crystal. This means that all crystals contain the identity operation and therefore it doesn't aid in the classification of materials.

Mirror planes are planes that divide the unit cell into two parts so that they are mirror images of each other. The basic symmetry operation taking place about a mirror plane is the mirror reflection.

Axis of rotation is a line about which a rotation by a given angle can be carried out. The notation for the rotation axis is C_n where n specifies the angle of rotation as $360/n$. Note that the identity operation is equivalent to a C_1 rotation.

Centre of inversion is a point through which (x,y,z) $\rightarrow$ (-x,-y,-z) transformation can take place for all points of the unit cell and the corresponding symmetry operation is the inversion operation.

The set of symmetry operations the crystal has (excluding translations) will define its *point group* (32 possibilities in three-dimensions if rotational symmetries are limited) where the number of operations is referred to as the order of the group. However, for an extended crystal we must consider also symmetry operations containing a translational component, where a displacement of the unit cell is also a symmetry of the system as illustrated in Figure 1.1b. This will give the *space group* (230 possibilities in three-dimensions) of the crystal.

The way in which atoms are arranged in ordered crystals depends on the underlying crystal lattice, i.e. the Bravais lattice. In Bravais lattice, each lattice point is connected

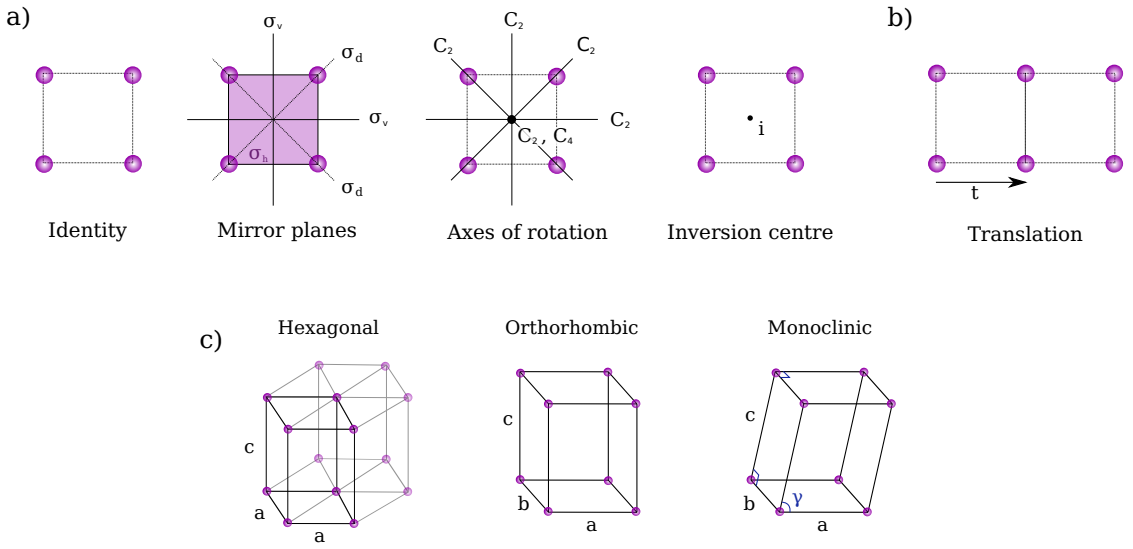

Figure 1.1: a) The four basic symmetry elements about which symmetry operations take place applied to a 2D square. b) Illustration of a translation symmetry operation, where all points of the object can be translated by the same distance in a given direction while leaving the object unaltered. c) The Bravais lattices relevant to this Chapter. Note that all of them belong to the primitive type of the respective crystal families.

to each other by a translation symmetry operation. In three dimensions, there are only 14 distinct Bravais lattices, each belonging to one of the crystal families: cubic, hexagonal, tetragonal, orthorhombic, monoclinic or triclinic. Within the families, there are also different types of lattices, such as primitive, body-centered, and face-centered lattices. In this Chapter, only three Bravais lattices are relevant with respect to our material of interest: hexagonal, orthorhombic, and monoclinic, which are all illustrated in Figure 1.1c. In essence, there's a lowering of symmetry when going from hexagonal to orthorhombic to monoclinic lattice - such a structural transition occurs in our material of interest as a function of temperature as will be discussed in Section 1.4.1.

1.1.2 Classification based on magnetic ordering

So far we have only considered the spatial arrangement of atoms in a crystal and neglected the magnetic moments associated with the atoms. Accounting for the magnetic ordering requires an introduction of an additional symmetry, namely the time-reversal symmetry ($\mathscr{T}$). As the name implies, this theoretical symmetry reverses the arrow of time: angular momentum, current density, and magnetic fields break $\mathscr{T}$ while for example position and electric field do not. The relevance to magnetic materials stems from the relation of the electron angular momentum to its magnetic moment meaning that reversing time will effectively reverse the magnetic moment direction. Para- and diamagnetic materials where the magnetic moments do not exhibit long-range ordering are $\mathscr{T}$-symmetric while ferro- and ferrimagnetic materials with long-range magnetic ordering break $\mathscr{T}$-symmetry. In antiferromagnets, $\mathscr{T}$-symmetry is restored globally by spatial symmetry operations as will be discussed in greater detail in the next Section. It is therefore evident that in order to efficiently classify magnetic materials we must include the $\mathscr{T}$-symmetry in addition to the spatial symmetries [56].

Two different approaches can adopted to the classification of magnetic materials: i) relativistic magnetic space groups where the coordinate and spin space are coupled [57], and ii) non-relativistic spin-symmetry groups where the coordinate and spin space are decoupled [58]. In a coupled coordinate and spin space any spatial symmetry operation applied to the magnetic crystal will simultaneously act on the atomic coordinates and the magnetic moment components, while in a decoupled space this is not the case. The former is a good description for materials with strong spin-orbit coupling but it is not sufficient for describing any non-relativistic phenomena. Being generally restricted to the relativistic phenomena, the magnetic space groups suffer from a lack of generality and are not able to for example distinguish between a ferromagnet and an antiferromagnet or a collinear and non-collinear magnet [56]. The spin-symmetry groups, in turn, can make this distinction and have in fact recently revealed the possibility of having a spin-split band structure in a compensated magnet [59][39], which have properties distinct from both ferromagnets and collinear antiferromagnets. This class of materials (dubbed altermagnetic [39] after the alternating spin-splitting) will be our focus for the remaining of this Chapter.

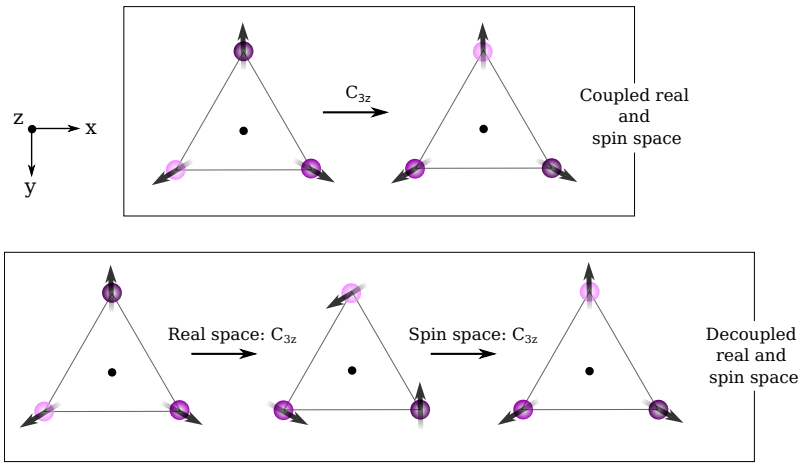

Figure 1.2: The two different approaches when classifying magnetic materials based on symmetry: (Top) symmetry operations (here 120 deg rotation around z-axis) act simultaneously on the atomic coordinates and the spin components or (Bottom) symmetry operations act separately on the atomic coordinates and the spin components.

1.2 Emergence of spin-splitting in the band structure of collinear compensated magnets

Various theoretical predictions of the existence of spin-split collinear compensated magnets, previously considered symmetry-forbidden, have surfaced in recent years. These reports have shown that a strong spin-orbit coupling is not necessary but rather the key requirement is a sufficient lowering of the spatial symmetries of the compensated magnet: Hayami *et al.* arrived at this conclusion using microscopic multipole descriptions [37][60], Yuan *et al.* delineated the magnetic space groups that could host spin-split compensated magnets using symmetry arguments [38], and Smejkal *et al.* and Liu *et al.* adopted a third approach of utilizing spin-symmetry groups rather than magnetic space groups.

In this Section we follow the approach of Šmejkal *et al.* [39] and briefly summarize how collinear magnetic materials can be classified using the spin-symmetry groups. Here, the notation for the spin group has the format $[R_i \parallel R_j]$, where R_i is a symmetry operation acting on the spin space while R_j acts on the coordinate space. This classification yields three non-relativistic, distinct groups illustrated in Figure 1.3:

- **Type I** has the spin group $\mathbf{R}_s^I = [E||\mathbf{G}]$, meaning that it contains symmetries that combine identity E in the spin space with all crystallographic point groups having a centre of symmetry in the coordinate space ($\mathbf{G}$). This group therefore implies non-zero net magnetisation and spin-split band structures, meaning that it contains the collinear ferromagnets.

- **Type II** has the spin group $\mathbf{R}_s^I = [E||\mathbf{G}] + [C_2||\mathbf{G}]$, so it contains again E in the spin space combined with $\mathbf{G}$ and, in addition, C_2 in the spin space combined with $\mathbf{G}$. Here the latter term contains the combination of C_2 in spin space and E in the coordinate space meaning that the system is invariant upon spin inversion, which forces the band structure to be spin degenerate throughout the Brillouin zone. This group corresponds to collinear antiferromagnets.

- **Type III** has the spin group $\mathbf{R}_s^I = [E||\mathbf{H}] + [C_2||\mathbf{G} - \mathbf{H}]$, where $\mathbf{H}$ contains the spatial symmetry operations that connect the same-spin sublattices, while $\mathbf{G} - \mathbf{H}$ contains rotation operations that connect the opposite-spin sublattices (note that translation and inversion are excluded). This third group contains collinear magnets, which have a compensated magnetic ordering and alternating spin-split band structures in the momentum space. This group has been dubbed as altermagnets [39].

In simple terms this means that i) ferromagnets can be distinguished from antiferromagnets and altermagnets because their symmetries allow for a time-reversal symmetry breaking both in the real and momentum space and ii) the difference between antiferromagnets and altermagnets, (which both contain symmetries that ensure vanishing net magnetisation in the real space) is that in antiferromagnets the time-reversal symmetry is not broken in the momentum space while in altermagnets this is the case, manifesting in an alternating, spin-split band structure. The implication of this is that altermagnets possess the favorable properties of both ferromagnets (strong magnetotransport effects like AHE [43][1][61], GMR, TMR [44]) and antiferromagnets (robust against field perturbations, fast dynamics [29]) while also having additional unique properties (pure spin current generation [50], chiral magnons [51]). We will now discuss real-life examples of altermag-

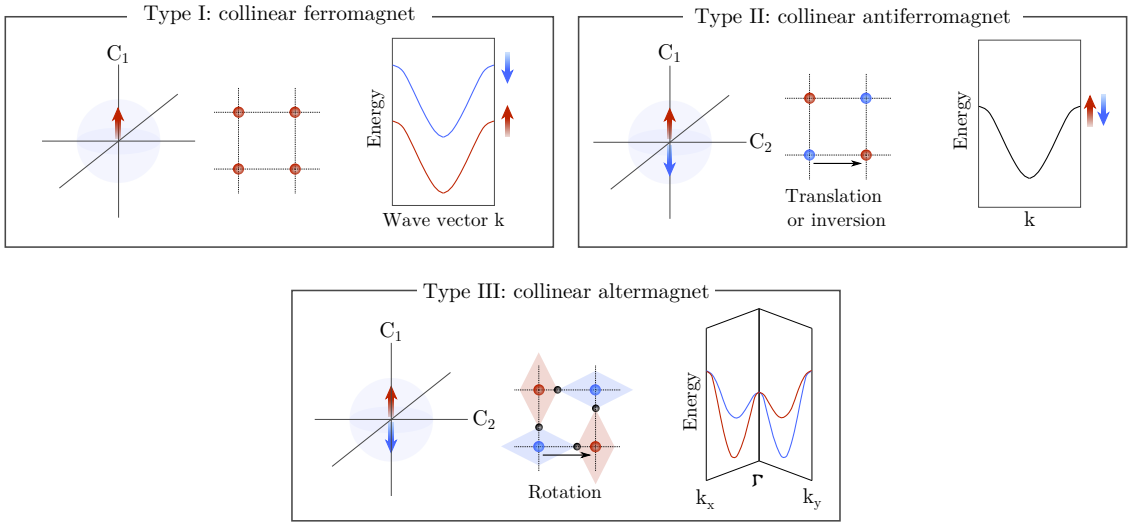

Figure 1.3: The three groups of collinear magnets classified by their non-relativistic spin symmetry groups. Transformations in the spin space and in the coordinate space, as well as the energy dispersion are shown for each type. The figure has been adapted from [62] and [63].

netic materials and the experimental verifications of their belonging to the altermagnetic group.

First altermagnetic material candidates - RuO_2, MnTe

The key for realizing an altermagnetism is lowering the symmetry of the system so that the opposite-spin sublattices are not connected by translation or inversion. This can be realized in various ways, such as through the configuration of the non-magnetic atoms or multisublattice arrangements. The first candidate material where the altermagnetism has been theoretically predicted [42] and experimentally verified [43][50] is RuO_2. As illustrated in Figure 1.4a, the two opposite-spin sublattices of RuO_2 are connected by a four-fold rotation around the z-axis (C_{4z}). Here, for the evaluation of the correct symmetry of RuO_2 it is critical to consider the non-magnetic oxygen atoms, which are causing the magnetisation densities of the Ru atoms to be anisotropic, effectively lowering the symmetry of the system. Figure 1.4b shows the Fermi surface cut of RuO_2 obtained through *ab initio* calculations [42] where the expected alternating and momentum-locked

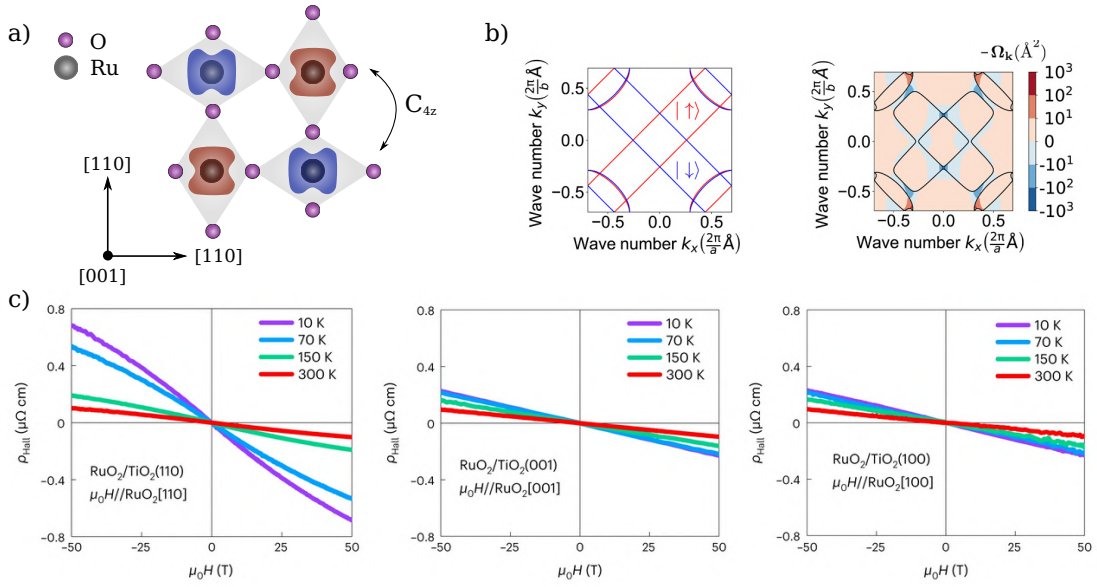

Figure 1.4: a) The crystal structure of RuO_2 with the spin density isosurfaces obtained from *ab initio* calculations shown as red and blue pinched cylinder shapes for the two opposite-spin sublattices. These sublattices are connected by a four-fold rotation about the [001] axis in the real space. Figure adapted from Ref. [43]. b) (Left) The Fermi surface cut of RuO_2 with spin-orbit coupling omitted showing the spin-splitting of the band structure, and (Right) the corresponding Berry curvature in atomic units. Both plots are obtained through *ab initio* calculations. Figure obtained from Ref. [42]. c) The experimentally observed AHE in RuO_2 with the three plots corresponding to the Néel vector ($\mathbf{L}$ = M_1-M_2) being oriented along different crystal axes showing the unique anisotropy of the effect. The only direction along which the AHE is allowed by symmetry is [110], which is evidenced by the experimental data. Note that the linear contribution is from ordinary Hall effect and the AHE originating from the weak magnetisation. Figure obtained from Ref. [43].

spin-splitting is observed and which results in a non-zero Berry curvature. Based on the band structure, the theory also predicts a sizable anomalous Hall effect and the ability to generate a pure spin current [49], which have both been recently verified experimentally [43][50]. The notion of Berry curvature and how it connects to AHE will be described in the next Section. RuO_2 is not the only compensated magnet showing altermagnetic properties - also MnTe has been predicted to be altermagnetic due to the configuration of the non-magnetic atoms [39] and this was indeed supported by the experimental observation of AHE [61].

The experimental difficulty in studying altermagnetic materials is the fact that they have to be of high crystalline quality and preferably single-domain. This is because the magnetotransport effects of altermagnets are strongly dependent on how the order parameter is oriented relative to the crystal structure and therefore samples with multiple crystal orientations and/or order parameter orientations result in the vanishing of these effects. Given that the magnetotransport properties are so far the most efficient tool for identifying and probing the altermagnetism, this is a considerable obstacle. Moreover, materials with strong magnetocrystalline anisotropy pose further experimental issues due to the large fields required for the manipulation of the order parameter. For example, in order to orient the Néel vector ($\mathbf{L}$ = M_1-M_2) of RuO_2 along the (hard) crystal axis that also yields the strongest AHE amplitude fields of 50 T are required, necessitating the use of specialized high-field facilities [43]. In the case of MnTe, more reasonable fields of ~ 6 T are sufficient [61]. In order to further study the different magnetotransport properties of altermagnets and their potential in spintronic applications, it is therefore of considerable research interest to seek for more material candidates. Later in Section 1.4, we will introduce Mn_5Si_3, the compensated magnet of interest for our studies, which in the strained epitaxial thin film format shows strong indications of the altermagnetism.

1.3 Anomalous Hall effect in spin-split compensated magnets

We will now move on to discussing the novel magnetotransport properties of altermagnets in more detail. More specifically, we are interested in the anomalous Hall effect (AHE), which is only allowed in systems with broken time-reversal symmetry ($\mathscr{T}$) and therefore has been typically considered forbidden in compensated magnets. As we have learnt, however, in altermagnets $\mathscr{T}$ is broken in the momentum space and thus AHE becomes symmetry-allowed.

The family of Hall effects convert a longitudinal charge current into a perpendicular (Hall) voltage across the sample, as illustrated in Figure 1.5a. In the conductivity tensor of a material, the Hall conductivity is described by the antisymmetric part (a_{ik}; $\sigma_{ij} = -\sigma_{ji}$), while the longitudinal conductivity is described by the symmetric part (s_{ik}; $\sigma_{ij} = \sigma_{ji}$). The conductivity tensor divided into the two parts is given by

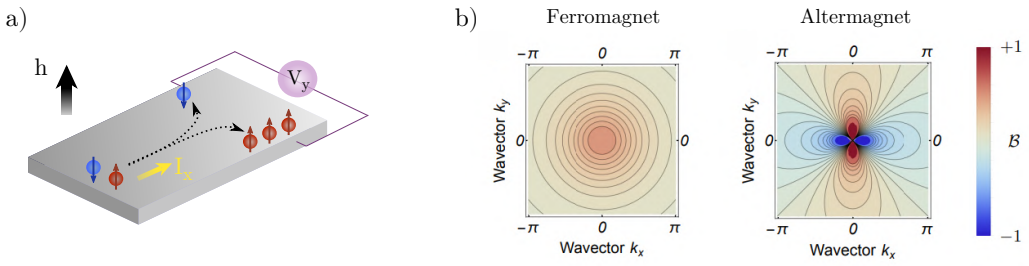

Figure 1.5: a) Schematics of an anomalous Hall effect where a longitudinal current is converted to a transversal voltage. b) Berry curvature of a ferromagnet with a strong spin-orbit coupling and an altermagnet around a band crossing point. For the former the Berry curvature is isotropic while for the latter it is strongly anisotropic, which results in inherently different properties of the AHE. Figure obtained from Ref. [64].

$$\sigma_{ik} = s_{ik} + a_{ik} = \begin{bmatrix} \sigma_{xx} & 0 & 0 \\ 0 & \sigma_{yy} & 0 \\ 0 & 0 & \sigma_{zz} \end{bmatrix} + \begin{bmatrix} 0 & \sigma_{xy} & \sigma_{xz} \\ -\sigma_{xy} & 0 & \sigma_{yz} \\ -\sigma_{xz} & -\sigma_{yz} & 0 \end{bmatrix}, \tag{1.1}$$

where the first term is the symmetric and the second term is the antisymmetric part. The latter only contains three components and can therefore be expressed as an axial (i.e. no sign change upon inversion) Hall vector $\mathbf{h} = (\sigma_{yz}, \sigma_{zx}, \sigma_{xy})$. Ohm's law can then also be expressed in terms of the two parts: $J_i = s_{ik}E_k - (\mathbf{h} \times \mathbf{E})_i$. Since current is $\mathcal{T}$-odd and the electric field is $\mathcal{T}$-even, the system must somehow break the $\mathcal{T}$-symmetry to ensure that the two sides of the Ohm's law have the same symmetry. For the symmetric part relating to the longitudinal current $\mathcal{T}$-symmetry is broken by dissipation through Joule heating ($\propto \mathbf{j} \cdot \mathbf{E}$) while for the anti-symmetric part the $\mathbf{h}$ must be $\mathcal{T}$-odd as the transversal current is dissipationless ($\mathbf{j}_H = \mathbf{h} \times \mathbf{E}$).

In order for a system to have a non-zero $\mathbf{h}$, it is necessary for the system to have a broken $\mathcal{T}$-symmetry (as per Curie-Neumann's principle, see Section 1.1). This can be realized in any material by applying an external field, which results in the observation of an ordinary Hall effect (OHE) where the transversal voltage increases linearly with field. In ferromagnetic materials with a net magnetisation, the $\mathcal{T}$-symmetry is also broken and therefore a transversal voltage proportional to the magnetisation can be measured even in the absence of an external field, dubbed as the anomalous Hall effect (AHE) [65]. These are not the only $\mathcal{T}$-odd systems, however, as we have seen in Section 1.2 - $\mathcal{T}$-symmetry breaking in the momentum space can also be realized in collinear magnets without net magnetisation if they belong to a specific spin symmetry group, i.e. the altermagnetic group [37][38][39]. This is not limited to collinear compensated magnets only but AHE has been theoretically predicted [40][36] and experimentally observed [41][66] in various non-collinear antiferromagnets with favorable symmetries (i.e. $\mathcal{T}$-odd). A more detailed review on the anomalous Hall antiferromagnets can be found in Ref. [64].

Intrinsic microscopic origin of anomalous Hall effect

Microscopically, AHE can have various origins relating to either the topology of the band structure of the material or to the asymmetric impurity scattering of the electrons [65]. The former (intrinsic) contribution is more relevant here as the spin-orbit coupling in Mn_5Si_3 is weak and therefore will be discussed in more detail while the latter (extrinsic) contribution will be covered in Chapter 3.

The intrinsic contribution relates to the geometric Berry phase that the electron wavefunctions acquire when making a closed loop in the momentum space [67], giving a transversal contribution to the electron velocity:

$$\mathbf{v}_n(\mathbf{k}) = \frac{\partial \varepsilon_n(\mathbf{k})}{\hbar \partial k} - \frac{e}{\hbar}\mathbf{E} \times \Omega_n(\mathbf{k}). \tag{1.2}$$

Here, the first term is the usual group velocity of Bloch electrons, where n is the band index and ε is the energy of the Bloch state. The second term is the transversal velocity, where $\mathbf{E}$ is the electric field and $\Omega_n(\mathbf{k})$ is the Berry curvature of the nth band. The Berry curvature can be viewed as a fictitious magnetic field in the momentum space and is defined as:

$$\Omega_n(\mathbf{k}) = i\langle \nabla_k u_n(\mathbf{k})| \times |\nabla_k u_n(\mathbf{k})\rangle, \tag{1.3}$$

where $u_n(\mathbf{k})$ is the wavefunction of a Bloch electron in band n. It is important to note that a non-zero Berry curvature can only be realized in systems lacking the $\mathscr{P}\mathscr{T}$-symmetry as follows from $\mathscr{P}\mathscr{T}\Omega_n(\mathbf{k}) = -\mathscr{P}\Omega_n(-\mathbf{k}) = -\Omega_n(\mathbf{k}) = 0$. Here our focus is on the broken $\mathscr{T}$-symmetry.

In the framework of the Boltzmann transport, the current density is linked to the electron velocity through $\mathbf{j} \propto \int f(\mathbf{k})\mathbf{v}(\mathbf{k})d\mathbf{k}$ and thus the non-zero transversal velocity originating from the non-vanishing Berry curvature results in AHE conductivity (σ_{xy}) given by:

$$\sigma_{xy} = \frac{e^2}{\hbar}\int \frac{d\mathbf{k}}{(2\pi)^d} f(\varepsilon_\mathbf{k})\Omega_{k_x,k_y}, \tag{1.4}$$

where $f(\varepsilon_\mathbf{k})$ is the Fermi-Dirac distribution function and d is the system dimension. It should be noted that here the integration is over the entire Brillouin zone and therefore regardless of the presence of non-zero 'hotspots' of Berry curvature, it is possible that the integral of the Berry curvature vanishes. This will be the case in altermagnets where some orientations of Néel vector result in a complete switching off of the AHE due to cancelling out of the Berry curvature, as illustrated in Figure 1.5b. This kind of symmetry prohibition and the resulting intrinsic anisotropy of the AHE is a characteristic feature of altermagnets and not observed in ferromagnets where any orientation of the magnetisation allows the AHE to arise. This anisotropy of AHE inherent to altermagnets will be discussed extensively later in this Chapter.

1.4 A new altermagnetic candidate - epitaxial films of Mn_5Si_3 [1][2]

Mn_5Si_3, a compensated collinear magnet with a hexagonal crystal structure shown in Figure 1.6a, in its epitaxial thin film form is a potential candidate for hosting an altermagnetism as indicated by a symmetry analysis and DFT calculations [1]. In this Section, we will first briefly discuss the properties of bulk Mn_5Si_3, which is an extensively studied antiferromagnet, and then move on to the epitaxial thin films of Mn_5Si_3, the properties of which greatly vary from those of the bulk Mn_5Si_3. The epitaxial nature of the films stabilizes a particular crystal structure and spin configuration that leads to the system exhibiting the characteristic transport properties of an altermagnetic rather than antiferromagnetic phase.

1.4.1 Properties of antiferromagnetic bulk Mn_5Si_3

Bulk Mn_5Si_3 is an extensively studied antiferromagnetic intermetal hosting both collinear and non-collinear antiferromagnetic (AFM) phases as verified by various neutron diffraction experiments [68][69][70][71] and supported by DFT calculations [72][73]. The first magnetic phase transition from the paramagnetic (PM) to collinear AFM phase at $T_{N1} \sim$ 100 K is accompanied by a structural phase transition from a hexagonal to an orthorhombic crystal structure [71] as shown later in Figure 1.8. The second magnetic phase transition to the non-collinear AFM phase occurs at $T_{N2} \sim 66$ K and the symmetry of the structure is further lowered down to monoclinic [70].

In the PM phase with a hexagonal crystal structure (a = 6.910 Å and c = 4.814 Å [75]) the Mn atoms have two distinct crystallographic positions (Mn1 and Mn2, indicated in Figure 1.6a), but the structural changes accompanying the formation of long-range magnetic ordering results in a splitting of the Mn2 positions, yielding a variety of different environments for the Mn atoms. It is well-known that the Mn moments are highly sensitive to their local environment, especially the distance between two Mn moments [76][77], which explains why the crystal structure of Mn_5Si_3 results in a highly non-trivial spin configuration. Neutron diffraction measurements have shown that in the collinear phase none of the Mn1 atoms and two thirds of the Mn2 atoms are magnetically ordered [71] as highlighted in Figure 1.6a. In the non-collinear phase, on the other hand, all Mn1 acquire a magnetic moment and two thirds of the Mn2 atoms remain magnetic, while the spin structure is more complicated and controversial as various configurations have been proposed [70][74][73]. An additional complexity is added by the sensitivity of the spin configuration to a magnetic field - further magnetic phase transitions can be induced by the application of an external field [74][78][73].

Besides neutron diffraction measurements, the assignment of collinear and non-collinear AFM phases has been corroborated by magnetotransport measurements - in polycrys-

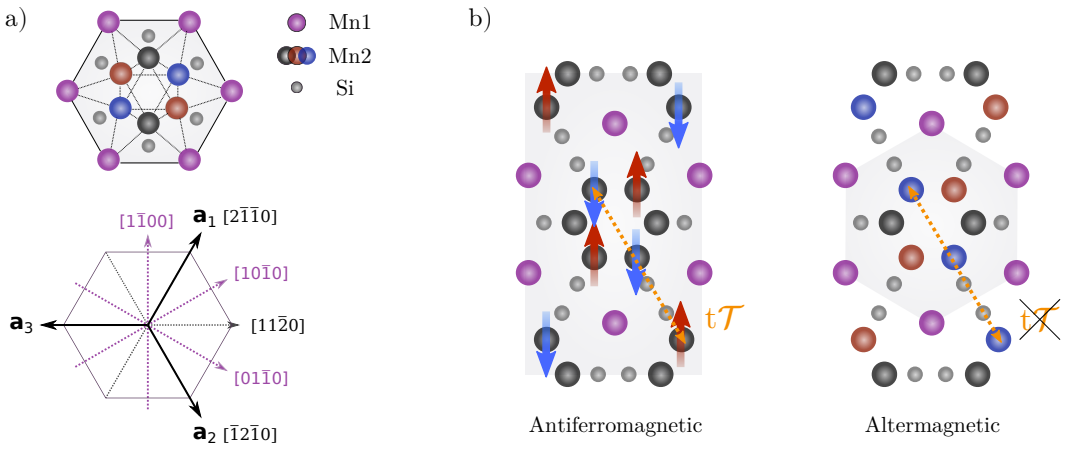

Figure 1.6: a) (Top) The hexagonal unit cell of Mn_5Si_3 with two crystallographically distinct positions for the Mn atoms denoted as Mn1 and Mn2. (Bottom) A generic hexagonal unit cell where some of the main crystal axes have been noted. These axes will be relevant later in this Chapter. b) The collinear, antiferromagnetic spin configuration of Mn_5Si_3 after Refs. [71][74][72], hosted by the orthorhombic crystal structure. Two-thirds of the Mn2 atoms show long-range magnetic ordering and the two opposite-spin sublattices are highlighted with red and blue. Here, the opposite-spin sublattices are connected by a $t\mathcal{T}$-symmetry. c) Spin configuration of Mn_5Si_3 with hexagonal unit cell that is predicted by DFT calculations to belong to the altermagnetic group [1]. Here, the $t\mathcal{T}$-symmetry connecting the two opposite-spin sublattices is broken.

talline films of Mn_5Si_3 in the collinear phase no AHE is observed, while in the non-collinear phase THE is observed suggesting a non-collinear spin arrangement [79]. Note that in polycrystalline films the possible strain from the substrate can relax at the grain boundaries and moreover, even if the individual grains had a correct symmetry for altermagnetism the AHE would vanish regardless due to averaging out by the different crystal orientations. In this work, the focus is on the collinear phase of Mn_5Si_3 and therefore the discussion on the non-collinear phase will be limited.

1.4.2 Growing epitaxial thin films of Mn_5Si_3 [2]

Our films are grown by the group of Prof. Lisa Michez (Aix-Marseille University, CINaM) in the framework of ANR – DFG consortium and the details of the growth are discussed in detail in Ref. [2]. We will summarize the growth procedure here followed by a discussion on the crystal structure and quality of the films.

The films are grown via co-deposition of Mn and Si on Si(111) substrates using molecular beam epitaxy (MBE), which enables highly controlled layer-by-layer growth of thin films [81]. The silicon substrates are treated chemically and physically prior to the deposition in order to realize high-quality starting interfaces free of impurities and with a correct surface reconstruction (7x7). During the growth, depending on the growth parameters such as ratio of deposition rates (V) ($R_{Mn/Si} = V_{Mn}/V_{Si}$) and growth temperature

(T_G), two different phases Mn_5Si_3 and MnSi can form in different proportions. These proportions can be further modified using a post-annealing process where the annealing temperature (T_A) is a crucial factor for determining which phase is favored. For our purpose, highly crystalline films of pure Mn_5Si_3 are desired. However, it was observed that the MnSi layer that forms between the Si(111) substrate and the Mn_5Si_3 layer actually acts as a seed layer and promotes the nucleation of Mn_5Si_3, thereby being a seemingly unavoidable component of the epitaxial Mn_5Si_3 films. As a compromise, the epitaxial films used for obtaining the results in this Chapter contain 96% Mn_5Si_3 and 4 % MnSi and were realized under the growth and post-growth conditions of $R_{Mn/Si} \sim 1.6$, $T_G \sim 443$ K, and $T_A \sim 493$ K. The optimization of the parameters for highest Mn_5Si_3 content is shown in Figure 1.7b.

The epitaxial films used in this work are ~ 17 nm thick and of high crystalline quality as shown by the TEM image in Figure 1.7c. The epitaxial relationship between the Si(111) substrate and the MnSi and Mn_5Si_3 phases is Si(111)$[1\bar{1}0]$//MnSi(111)$[\bar{2}11]$//Mn_5Si_3(0001) $[01\bar{1}0]$ (see Figure 1.7a,c) as observed by means of reflection high-energy electron diffrac-

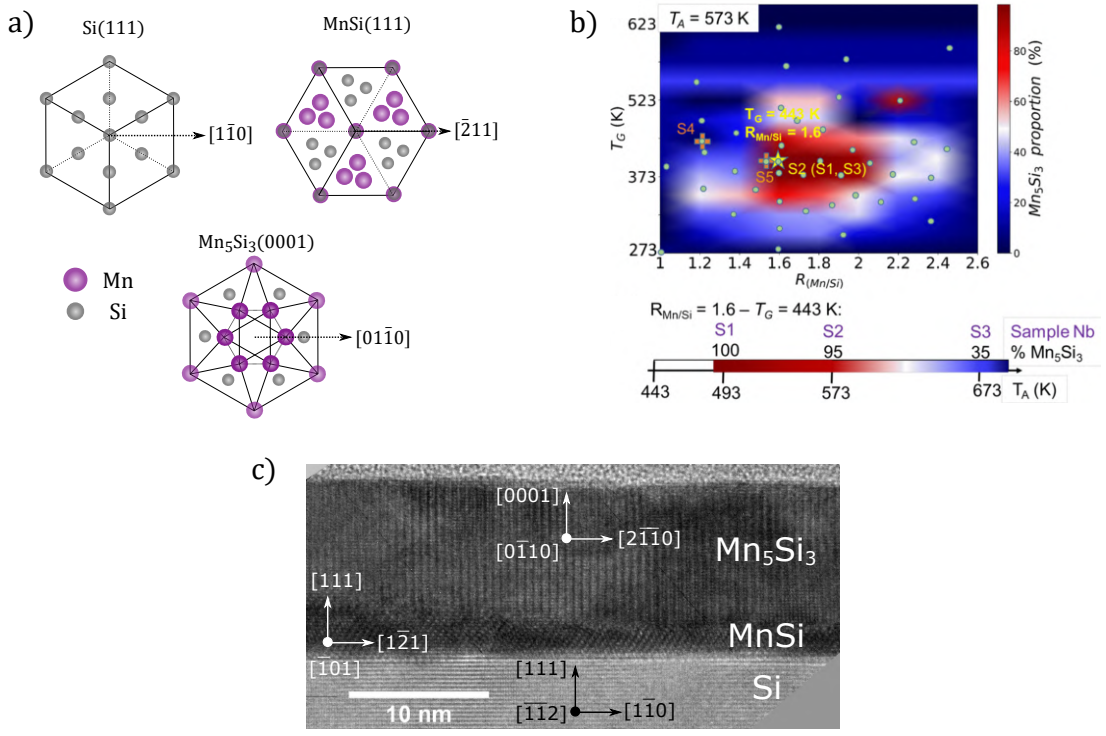

Figure 1.7: a) The schematic structures of Si (111), MnSi (111), and Mn_5Si_3 (0001) surfaces, which are the planes perpendicular to the growth direction in our samples. Figure adapted from Ref. [2]. b) The optimisation of the growth of pure epitaxial Mn_5Si_3 films as a function of the growth temperature, deposition rate, and annealing temperature. Optimal conditions for highest Mn_5Si_3 content are $R_{Mn/Si} \sim 1.6$, $T_G \sim 443$ K, and $T_A \sim 493$ K. Figure obtained from Ref. [2]. c) Transmission electron microscopy image of the epitaxial Mn_5Si_3 film on Si(111) substrate with a thin MnSi seed layer. The crystal orientation of each layer is indicated.

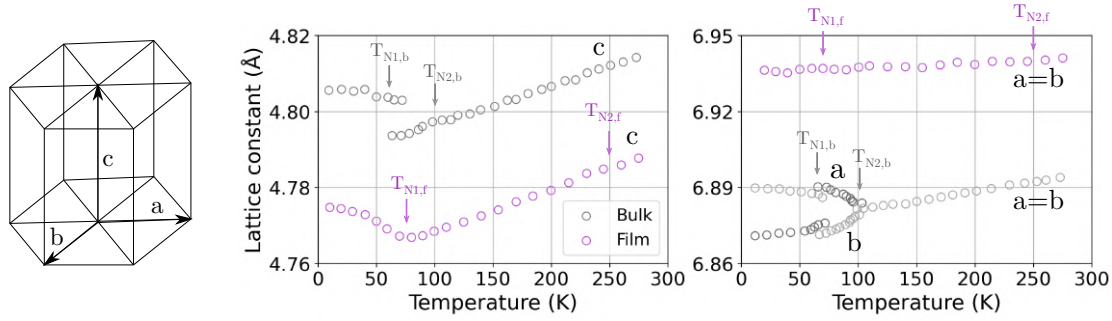

Figure 1.8: a) The temperature-dependence of the hexagonal lattice parameters a,b, and c for bulk (dark gray) and epitaxial films (purple) of Mn_5Si_3. The bulk data is extracted from Ref. [80]. For the bulk sample, clear structural changes coinciding with the magnetic phase transitions are observed. For the epitaxial films, besides the monotonous decrease, only an increase in c around 70 K is observed.

tion (RHEED), x-ray diffraction (XRD), and high-resolution tunneling electron microscopy (HRTEM) [2]. The lattice parameters in the paramagnetic hexagonal phase are a = 6.94 Å, and b = 4.79 Å, which slightly deviate from those of the bulk samples [75].

The temperature-dependence of the lattice parameters was recorded through XRD in order to follow any structural transformations accompanying the magnetic phase transitions and is shown in Figure 1.8 along with the data for bulk Mn_5Si_3 obtained from Ref. [80]. In the bulk, the transition from paramagnetic to collinear AFM ordering coincides with a structural transition to an orthorhombic phase (as indicated by the a and b lattice constants taking up unequivalent values) while the transition from collinear to non-collinear phase is accompanied by a jump in the c as well as a and b parameters. In comparison, for our epitaxial films there is no change in the a (= b) parameter throughout the temperature range while the jump in the c parameter is again observed around 70 K. These changes will be further discussed later in relation to the changes in the magneto-transport properties indicating magnetic phase transitions.

1.4.3 Verification of the compensated magnetic ordering

The magnetic ordering of our Mn_5Si_3 epitaxial films can be studied with a SQUID magnetometer, which is a highly sensitive tool for probing small magnetic moments (detection limit of the SQUID is $\sim 10^{-8}$ emu). First we measured the temperature-dependence of the magnetisation by sweeping the temperature from 300 to 5 K in steps of 5 K under zero-field and +2 T field that is either in-plane or out-of-plane. These temperature scans are shown in Figure 1.9 for a continuous sample containing the Mn_5Si_3 layer, MnSi seed layer, and a Si(111) substrate. For the field-cooled measurements we observe a roughly constant diamagnetic signal down to 100 K and below that there is first a gradual and then steeper increase in the magnetisation parallel to the field direction. This behavior is identical for the two cases of field parallel and perpendicular to the sample surface.

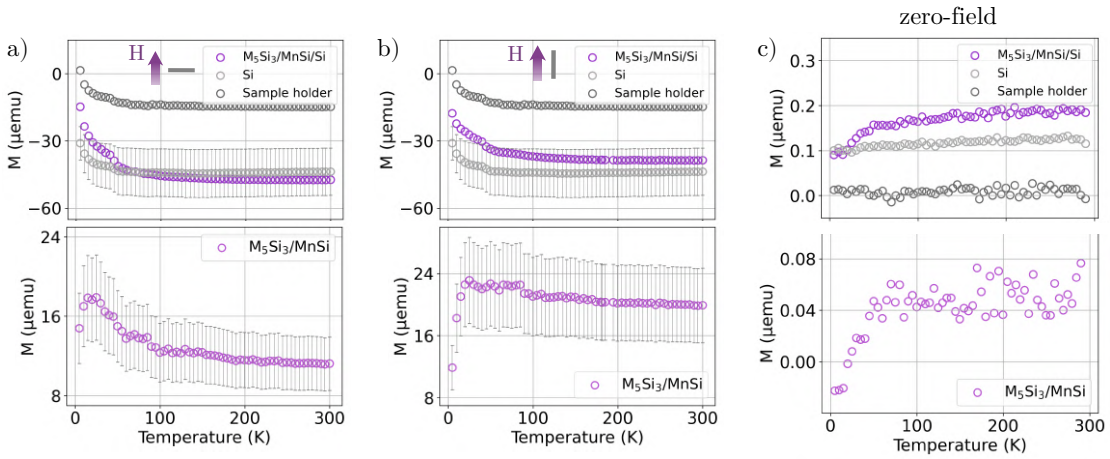

Figure 1.9: Total magnetisation of the Mn_5Si_3/MnSi/Si stack as a function of temperature a) under an external field of 2 T with the field out-of-plane and b) in-plane, and c) under zero-field. The signal contributions from the bare Si substrate (the error of $\sim 24\%$ originates from the area calculation of the two samples and the normalization of the substrate data to the Mn_5Si_3/MnSi/Si area) and the sample holder are also shown and have been subtracted from the total signal in order to find out the residual signal for the Mn_5Si_3/MnSi layer. This weak residual signal likely originates from the MnSi seed layer ($T_c \sim 50$ K) and magnetic impurities.

Surprisingly, the signal is non-zero yet very small, which is in contrast with the expected compensated magnetic ordering. However, the magnetic signal is originating from the entire Mn_5Si_3/MnSi/Si stack as well as the quartz sample holder, where epitaxial MnSi is known to be ferromagnetic below 50 K [82] while the Si substrate and the quartz sample holder are diamagnetic. Therefore in Figure 1.9 we also show the same temperature-scans for a bare Si substrate and for the quartz sample holder in order to disentangle the Mn_5Si_3/MnSi signal from the total signal. Note that the substrate signal has been normalized to the match the area of the Mn_5Si_3/MnSi/Si sample (Mn_5Si_3/MnSi/Si and Si sample areas are 0.12 and 0.16 cm^2, respectively). We can see that the signal from the bare substrate is similar order of magnitude while the signal from the sample holder is weakly diamagnetic but also non-monotonous.

The residual signal after the removal of these spurious contributions is weakly ferromagnetic and monotonous down to 100 K, below which there is a slight increase and a maximum around 10 K. The low-temperature non-monotonous behavior likely originates from the MnSi seed layer becoming ferromagnetic while the non-zero monotonous background extending to 300 K is likely relates to a presence of some ferromagnetic impurities as neither Mn_5Si_3 or MnSi is expected to be magnetic at room temperature. It should be noted that due to the high sensitivity of the SQUID magnetometer and the small signal of the Mn_5Si_3 layer of interest it is difficult to measure vanishing magnetisation as any magnetic contamination during the sample preparation will be detected [83]. Note also that the bare Si substrate we have measured is not strictly identical to the one below the Mn_5Si_3/MnSi layer as the latter has undergone additional cleaning procedures. It is

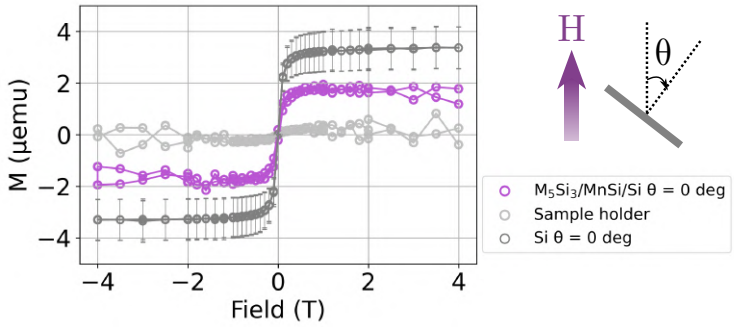

Figure 1.10: Magnetisation as a function of field at 110 K for the Mn_5Si_3/MnSi/Si stack, bare Si substrate, and the sample holder. The signal of the stack is comparable to that of the normalized Si substrate (the error of $\sim 24\%$ originates from the area calculation of the two samples and the normalization of the substrate data to the Mn_5Si_3/MnSi/Si area), their difference being of the order of 1 μemu, which corresponds to 0.02 μ_B/Mn showing a vanishing net magnetisation of our sample at 110 K.

therefore highly likely that above 100 K the magnetisation in the Mn_5Si_3/MnSi stack is negligible. For the zero-field cooled measurement in Figure 1.9c we observe a negligibly small residual signal for the Mn_5Si_3/MnSi layer with a monotonous behavior down to $\sim$ 70 K below which there is a sharp decrease. This could again relate to the ferromagnetic ordering of the MnSi with a non-zero component antiparallel to the field direction.

To supplement the temperature-dependent measurements, we have also measured the field-dependence of the magnetisation at 110 K, which is shown in Figure 3.15. We have again repeated the measurement for the Mn_5Si_3/MnSi/Si stack, bare Si substrate and the quartz sample holder. Both the stack and substrate signals show an S-shaped curve with a vanishing coercivity and similar saturation magnetisations (M_s), suggesting that a majority of the signal is again coming from the substrate. In fact, M_s of the Si substrate is slightly larger than that of the stack, which likely results from the fact that the substrate is not exactly the same as the one in the stack and has not been treated for the removal of impurities, which is the case for the Si substrate below the Mn_5Si_3/MnSi stack. Note again that the signal is in the order of 1 μemu so any spurious impurity signal will have a significant impact. We can nevertheless consider the difference between the M_s of the stack and the substrate as an indication of the upper limit of the net magnetisation of the Mn_5Si_3/MnSi layer. This difference is around 1 μemu, which we can convert to 0.02 μ_B/Mn, which again shows that at 110 K the net magnetisation of our sample is negligibly small indicating a compensated magnetic ordering of the Mn_5Si_3 epitaxial films.

1.4.4 *Ab initio* calculations showing the alternating spin-split band structure

The band structure of the epitaxial Mn_5Si_3 can be calculated using density-functional theory (DFT), a computational method where the properties of a material are calculated using

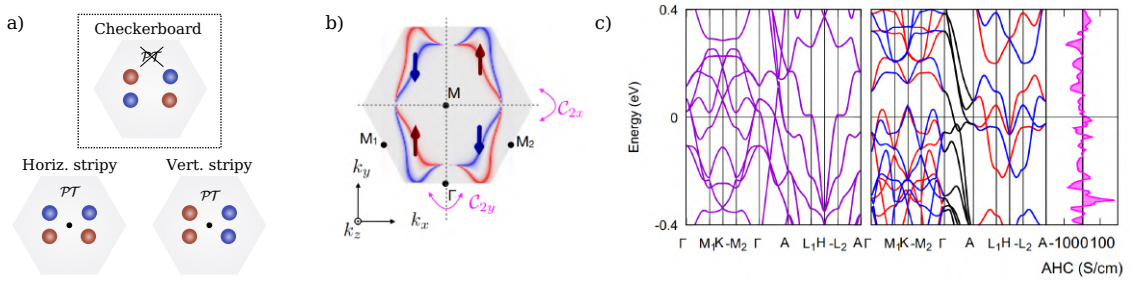

Figure 1.11: a) The possible arrangements of the opposite-spin sublattices in Mn_5Si_3 where only four Mn atoms are magnetically ordered. Of these arrangements, the checkerboard one is altermagnetic due to the absence of $\mathscr{P}\mathscr{T}$-symmetry while the other two are antiferromagentic. b) The Fermi surface cut of Mn_5Si_3 with a checkerboard arrangement of the sublattices and hexagonal unit cell as obtained by DFT calculations, showing alternating spin-splitting. Figure obtained from Ref. [1]. c) The calculated non-magnetic (first panel) and magnetic (second panel) band structures of Mn_5Si_3 along with the calculated anomalous Hall conductivity (AHC, σ_{AHE}) (third panel). Figure obtained from Ref. [1].

functionals of its electron density. The calculations in this Section have been conducted by Dr. Libor Šmejkal and co-workers at Mainz University and FZU Czech Academy of Sciences, and the technical details can be found in Ref. [1]. The calculations use the hexagonal crystal structure of Mn_5Si_3. We have first verified that the checkerboard-like compensated ordering of the four Mn atoms is the most energetically favorable one compared to a ferromagnetic, paramagnetic, and the two possible antiferromagnetic orderings (see Figure 1.11a). The calculated band structure of Mn_5Si_3 with a hexagonal unit cell (stabilized experimentally by epitaxy, see Section 1.4.2) and a checkerboard multi-sublattice arrangement reveals alternating spin-split energy bands even in the absence of spin-orbit coupling, as shown in Figure 1.11bc. This is as expected from the symmetry arguments, and supports the assigning of epitaxial Mn_5Si_3 to the altermagnetic group. Further calculations with the Néel vector (**L**) oriented along $[11\bar{2}1]$ direction predict a non-zero Berry curvature and thus non-zero intrinsic AHE conductivity, as shown in Figure 1.11c. Recall that the connection between Berry curvature and AHE was discussed in Section 1.3. The theoretical prediction for the AHE conductivity near the Fermi level is σ_{AHE} is 5-20 S cm^{-1}, which turns out to be in good agreement with the experimental observation as will be shown next.

1.4.5 Magnetotransport properties characteristic of altermagnetism [1]

Here we show the characterisation of the magnetotransport properties of our epitaxial Mn_5Si_3 films. We have patterned the epitaxial Mn_5Si_3 thin films into the standard Hall bar geometry (see Figure 1.12) using optical lithography and subsequent ion beam etching. For the magnetotransport measurements, we use Quantum Design Physical Property Measurement System (PPMS) equipped with a cryostat and a superconducting magnet,

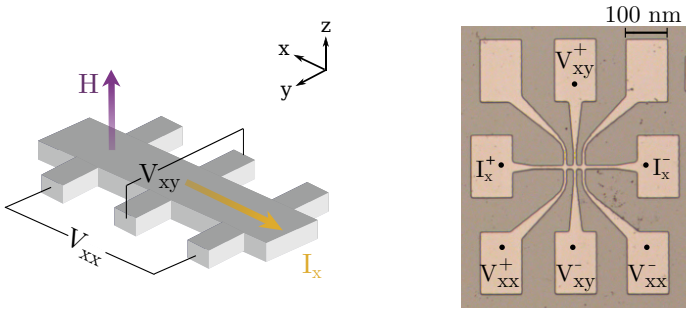

Figure 1.12: The Hall bar measurement configuration - (left) illustration and (right) an optical image of the actual devices.

which allow the application of temperatures ranging from 1.9 to 400 K and magnetic fields ranging from 0 to 9 T. We measure the longitudinal and transversal voltage signals (V_{xx} and V_{xy}, respectively, shown in Figure 1.12) as a function of either temperature, external field strength and/or orientation, or field sweeping rate. The exact measurement type will be specified in each relevant section. From here on, the voltage signals V_{xx} and V_{xy} are expressed in terms of resistivities ρ_{xx} and ρ_{xy} as defined by:

$$\rho_{xx} = \frac{V_{xx} w t}{I_x l} \qquad \rho_{xy} = \frac{V_{xy} t}{I_x}, \tag{1.5}$$

where w is the Hall bar width, l is the Hall bar length, t is the film thickness, and I_x is the applied current. Here, l = 45 μm, w = 10 μm, $t = 17$ nm, and $I = 0.5$ mA.

Identifying the magnetic phase transitions

First, we have measured ρ_{xx} as a function of temperature in order to identify the magnetic phase transitions. The resistivity of a magnetic solid is often expressed as a sum of contributions from the impurity scattering (temperature-independent), phonon scattering (temperature-dependent), and scattering from the localised magnetic moments (temperature-dependent):

$$\rho = \rho_0 + \rho_{ph} + \rho_{sd} \tag{1.6}$$

Both temperature-dependent terms decrease with lowering temperature, ρ_{ph} due to the presence of fewer phonons and ρ_{sd} due to decreased spin disorder. As ρ_{sd} is different for different magnetic phases, non-monotonous changes in ρ as a function of temperature can indicate magnetic phase transitions.

For the epitaxial Mn_5Si_3 films, the temperature-dependence of ρ_{xx} and its derivative are shown in Figure 1.13. Globally, the ρ_{xx} decreases when the temperature is decreased but exhibits a hump-feature around $\sim$ 50 K, which is consistent with previous observation on polycrystalline samples [84] and crystalline thin films [85]. The two magnetic phase transitions can be identified from the $d\rho_{xx}/dT$ plot: T_{N2} is characterized by a local minimum around $\sim$ 70 K, which is in good agreement with the previous reports [70][74][85],

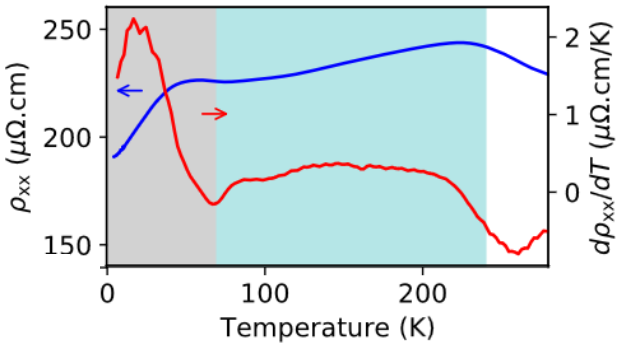

Figure 1.13: The temperature dependent longitudinal resistivity (ρ_{xx}) shows global decrease and a local maximum around 50 K below the lower Néel temperature T_{N2}. The measurement is repeated under zero-field and a positive 2 T out-of-plane field and both measurements show a similar trend. Plotting the derivative $d\rho_{xx}/dT$ reveals two magnetic phase transitions: $T_{N,2}$ at 70 K and $T_{N,1}$ at $\sim$ 250 K. Figure obtained from Ref. [1].

while the second transition temperature, T_{N1}, is around $\sim$ 250 K as indicated by another slope change. Remarkably, this is significantly larger than the 100 K identified in previous studies on bulk and thick film samples [71][74][85]. We attribute the enhanced T_{N1} in our epitaxial films to the stabilization of the structure favorable for the collinear ordering by epitaxy: in the bulk samples the T_{N1} phase transition is known to be accompanied by a structural phase transition from a hexagonal to an orthorhombic phase as was shown in Figure 1.8, while in our epitaxial films this structural transition does not take place but rather the hexagonal unit cell persists over the entire temperature range. It is therefore possible that in our epitaxial films the Mn distances favor the long-range magnetic ordering over a wider temperature range.

Next, we have measured the spontaneous ρ_{xy} as a function of temperature in order to obtain information about the magnetic ordering in terms of the $\mathscr{T}$-symmetry breaking - if the symmetry of the magnetic phase is such that it breaks $\mathscr{T}$ we expect to observe a sizable, non-zero spontaneous ρ_{xy}. As discussed above, for the epitaxial Mn_5Si_3 films a collinear, checkerboard magnetic ordering with a hexagonal unit cell would enable this. We have already shown that the hexagonal unit cell is preserved over the entire temperature range (recall Figure 1.8) so that the onset of non-vanishing ρ_{AHE} is predicted to coincide with a collinear, compensated magnetic phase transition. In Figure 1.14a we plot the transverse conductivity ($\sigma_{xy} = \rho_{xy}/\rho_{xx}^2$) as a function of temperature and it can be observed that a rapid increase in σ_{xy} is indeed observed at a temperature that corresponds to T_{N1} identified in Figure 1.13.

Anomalous Hall effect in epitaxial Mn_5Si_3 [1]

In order to understand the origin of this signal, we can take a closer look at the field-dependence of ρ_{xy} at different temperatures as shown in Figure 1.14b. The raw data (ρ_{xy}) comprises of various contributions: i) the ordinary Hall effect (OHE), where the electron

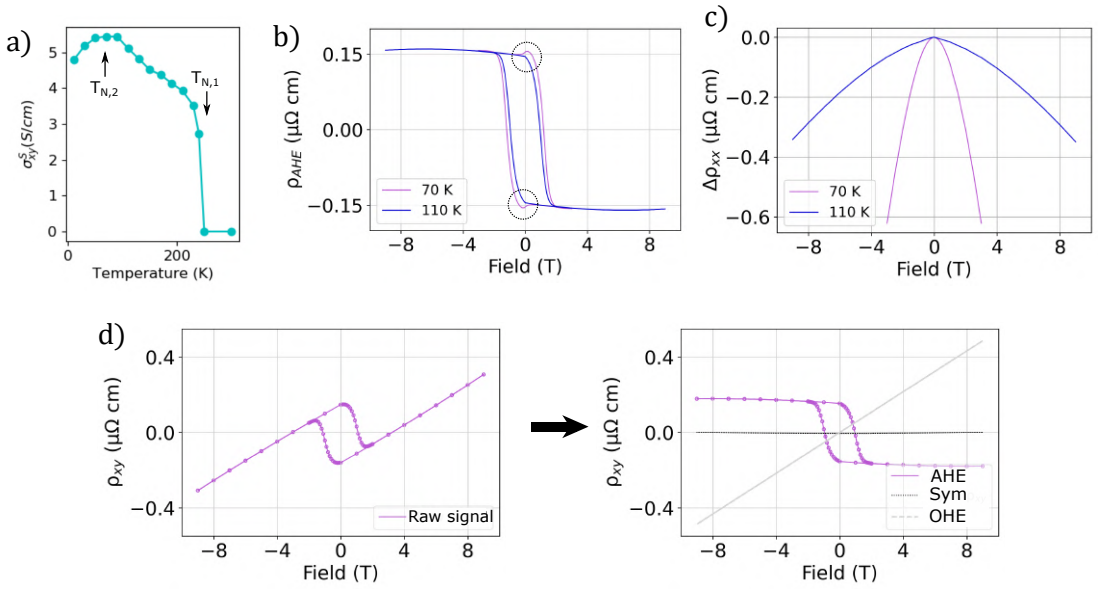

Figure 1.14: a) Temperature dependence of the transverse conductivity σ_{xy}. b) Field-dependence of ρ_{AHE} at 70 and 110 K showing hysteresis behavior typical for the compensated magnetic phases below $T_{N,2}$ and between $T_{N,2}$ and $T_{N,1}$, respectively. The sizable amplitude at 110 K corresponds well to the theoretically predicted value on the collinear phase while the topological-like features at 70 K can indicate a non-collinear phase. c) Field-dependence of $\Delta\rho_{xx}$ ($\Delta\rho_{xx} = \rho_{xx} - \rho_{xx,max}$) at 70 and 110 K. Typical anisotropic magnetoresistance behavior is observed. d) Processing of the raw field-dependence of the ρ_{xy} signal. We remove a linear slope relating to the ordinary Hall effect (OHE) and then separate the antisymmetric (relating to AHE) and symmetric parts of the signal.

paths are curved by the Lorentz force, is linear with field strength, ii) AHE, which is odd (antisymmetric) and non-linear with field, and iii) spurious even signal originating from e.g. slight misalignment of the Hall bar 'arms' (vanishingly small in our samples) [86]. We separate these different signals from the raw data as shown in Figure 1.14d and only retain the antisymmetric signal that relates to the AHE (ρ_{AHE}).

The processed data reveals a sizable spontaneous AHE with a relatively square shape and large coercivity of ~ 1 T, as shown in Figure 1.14b. Being in agreement with the theoretical predictions [1], the observation of AHE as well as the amplitude of the signal (~ 5 Scm^{-1}) points towards a collinear, checkerboard arrangement of the magnetic sublattices in our Mn_5Si_3 epitaxial films at this temperature of 110 K. This would also be analogous to the bulk Mn_5Si_3, where such a collinear, checkerboard spin configuration was identified between T_{N1} and T_{N2} by neutron scattering experiments [71]. The hysteresis loop at a temperature below T_{N2} exhibits additional bumps and dips between the saturation and coercive fields i.e. right before the switching of the Néel-vector direction (**L**) (indicated by circles in Figure 1.14b). Such features have been observed also in the non-collinear phase of the thick films and bulk samples of Mn_5Si_3, where it was attributed to the topological Hall effect (THE) arising from the real-space Berry phase induced by the non-collinear spin structure [79]. The fact that we observe these topological-like features below T_{N1}

might indicate that in analogy to the bulk samples the compensated phase below T_{N2} in our films is also non-collinear. However, in the absence of a direct observation of the spin structure this is not conclusive as the topological-like features could also originate from a coexistence of two phases with different magnetotransport properties [87].

Also the longitudinal resistivity ρ_{xx} strongly depends on the field strength as shown in Figure 1.14c (expressed as $\Delta\rho_{xx} = \rho_{xx} - \rho_{xx,max}$). The behavior is characteristic of anisotropic magnetoresistance (AMR) where the re-orientation of the **L**-vector by the field changes the sd-scattering cross-section. The AMR behavior in our Mn_5Si_3 epitaxial films will be discussed in more detail in the next Section.

1.5 Unconventional anisotropic magnetotransport properties of epitaxial Mn_5Si_3 [3]

An interesting property of the AHE in altermagnets is its inherent dependence on the underlying crystal structure. More specifically, the orientation of the Néel vector **L** relative to the crystal axes will change the symmetry of the system and some **L**-orientations allow a non-vanishing Hall vector **h**, while others may forbid it by symmetry. As a result, the AHE is expected to be strongly anisotropic upon reorienting the **L**-vector along different crystal axes. This is in contrast with the AHE in ferromagnets, where AHE is allowed by symmetry for any orientation of the net magnetisation so that the effect is largely isotropic. However, the Hall resistivity can be anisotropic with respect to the crystal structure also in crystalline ferromagnets [88] but the AHE cannot be switched off in a way similar to altermagnets but rather the Hall current direction varies with the magnetisation direction. The anisotropic AHE in altermagnets has been experimentally demonstrated in the case of RuO_2 (recall Figure 1.4c) where the **L**-orientation was manipulated using different growth directions of the crystal and the subsequent measurement of the AHE revealed a non-zero amplitude only for the sample where **L** was along a crystal axis for which symmetry analysis predicted a non-zero **h** [43]. The switching on and off of the AHE by the **L**-orientation has also been observed in the altermagnetic MnTe [61].

Having demonstrated that our epitaxial Mn_5Si_3 films exhibit a sizable AHE that can be switched and saturated with experimentally well-accessible fields of a few Teslas, we will move on to exploring the anisotropy of the AHE. The motivation for such a study is two-fold:

1. To obtain further information on the magnetic phase of the films. In other words, we can probe AHE as a function of the **L**-orientation in order to see whether the behavior matches that predicted for an altermagnetic material. This is useful given that it is complicated to experimentally elucidate the spin configuration of our films. This idea is akin to the initial discovery of antiferromagnets where the identification of the new magnetic phase was initiated by the study of their unconventional

macroscopic properties such as the vanishing net magnetization and unconventional temperature-dependence of the susceptibility, and only later on followed by the experimental verification of the spin structure.

2. To obtain further information about the **L**-orientation relative to the crystal structure. It is generally known that the magnetotransport properties vary with the **L**-orientation, and therefore systematic studies on changing its relative orientation and following the changes in ρ_{xy} and ρ_{xx} can provide useful information when combined with theoretical models.

In this Section we study two different ways of controlling the relative **L**-orientation in our films and how the changing relative orientation influences the magnetotransport properties. We will compare and contrast our results to the typical behavior of ferromagnets and antiferromagnets and argue that the unconventional anisotropic AHE in our films agrees well with the predicted altermagnetic group.

1.5.1 Néel vector control in compensated magnets

Compensated magnets are notoriously robust against external fields perturbations due to their vanishing net magnetisation and therefore controlling the order parameter **L** is less trivial than in ferromagnets. In uniaxial bipartite antiferromagnets the field-control of **L** is well-known [89][29]: the sensitivity to the field as well as the resulting behavior strongly depends on the relative orientations of the external field **H** and **L**, as illustrated in Figure 1.15. If **H** is perpendicular to **L**, it will induce a slight canting of the sublattice magnetisations, which generates a weak magnetic moment perpendicular to **L** that increases linearly with the field strength up to a saturation point where the field strength compensates for the exchange energy cost of the sublattice magnetisation aligning parallel to each other. The

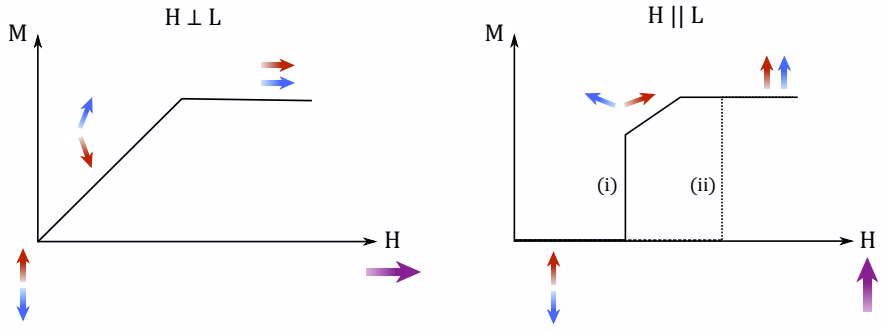

Figure 1.15: Illustration of the external field control of the Néel vector orientation in uniaxial bipartite antiferromagnets. (Left) When the field is perpendicular to the Néel vector it induces a small canting of the sublattice moments, which eventually results in the parallel alignment of the moments. (Right) A field parallel to the Néel vector can induce either a spin-flop transition (i) or a spin-flip transition (ii) depending on the strength of the anisotropy in the system.

field-induced magnetisation favors a $\mathbf{H} \perp \mathbf{L}$ configuration so that a re-orientation of $\mathbf{H}$ can result in a re-orientation of $\mathbf{L}$ if allowed by the magnetocrystalline anisotropy. If $\mathbf{H}$ is parallel to $\mathbf{L}$, on the other hand, the system is virtually insensitive to the field until it overcomes the anisotropy energy - this threshold is marked by a so-called spin-flop transition where $\mathbf{L}$ can rotate away from the easy axis and align perpendicular to the external field. Further increase in the field strength will result in a canting of the sublattice moments towards the applied field, which again induces a weak magnetic moment that increases linearly with the field up to saturation. If the system has a strong magnetocrystalline anisotropy, it will not exhibit a spin-flop transition but rather at a sufficiently strong field will transition directly from the antiparallel alignment of the sublattice magnetisations to a parallel one. Note that in addition to the external field the control of $\mathbf{L}$ has also been demonstrated by optical [34][33][90] and electrical [31][91][92][93][94] means.

In altermagnets the research on the $\mathbf{L}$ control is at very early stages as only two materials have been experimentally verified as altermagnetic. In RuO_2, where the crystal axis allowing for AHE is [110] and the easy axis is [001], a continuous re-orientation of $\mathbf{L}$ from [001] in the (110) plane towards [110] axis is realized by applying an external field along [110] [95][43]. However, this requires relativistic DMI terms, and therefore is not applicable to systems lacking them. In MnTe, $\mathbf{L}$ can be re-oriented through the spin-flip transition occurring around 2 T [61], indicating that the field-control of $\mathbf{L}$ models applying to antiferromagnets may also apply to altermagnets. It should be noted, however, that in altermagnets $\mathbf{L}$ is not the only order parameter but there is also a second order parameter relating to the anisotropy of the spin-split bands. The mechanisms through which the external field can couple to this anisotropy order parameter are a completely unexplored field of research and further investigations on it might reveal novel, unconventional switching mechanisms of $\mathbf{L}$.

Here we will demonstrate the external field control of the relative $\mathbf{L}$-orientation in our Mn_5Si_3 films using field strengths of the order of a few T through the systematic changes it inflicts on the magnetotransport properties of the films. However, drawing conclusions on the mechanisms through which the order parameter(s) couple to the field and switch are beyond the scope of this thesis and exciting topics for future research.

1.5.2 Anisotropic AHE demonstrated through external field rotation

In Section 1.4.5 the AHE resistivity (ρ_{AHE}) was measured in the standard Hall geometry where the external field is along the film normal. Here, we will investigate how the ρ_{AHE} varies when we rotate the field away from the film normal but still in the plane perpendicular to the current channel. The field orientation is defined by θ shown in Figure 1.16a and during the measurements θ is varied from 0 to 360 back to 0 deg in 2 deg steps. The Hall bar used has its current channel along the $[2\bar{1}\bar{1}0]$ crystal axis so that the field is rotated in the $(2\bar{1}\bar{1}0)$ crystal plane. The first field strength selected is 2 T because in Figure 1.14c we observed that this is sufficient for reversing and saturating the Néel vector, as

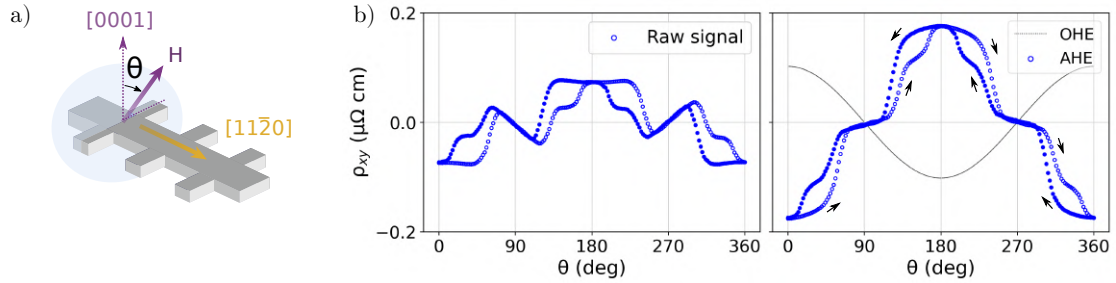

Figure 1.16: a) Illustration of the measurement geometry in the field-orientation dependent measurements. The angle θ denotes the orientation of the external field relative to the film normal in the plane perpendicular to the current channel (denoted as light blue area). Here, the current channel is along the $[2\bar{1}\bar{1}0]$ direction. (b) The AHE resistivity ρ_{AHE} as a function of θ with a 2 T external field at 110 K for a measurement geometry shown in (a). The raw signal contains a contribution from OHE, which can be removed to obtain the AHE contribution. The sweep direction is indicated by the small arrows and by the empty circles for the forward sweep and filled circles for the backward sweep.

indicated by a reversal of the ρ_{AHE} sign. The temperature is again 110 K, meaning that we are in the magnetic phase of Mn_5Si_3 showing altermagnetic properties.

The resulting field orientation dependence of ρ_{AHE} is shown in Figure 1.16b. The raw signal again contains a contribution from OHE, as was the case for the field-dependent data in Figure 1.14d. We have removed this OHE background by assuming it has a $\cos\theta$ dependence with an amplitude extracted from the field-dependent data as the OHE slope when $\theta = 0$ deg (in Figure 1.14d, OHE slope is $\sim 0.05\ \mu\Omega\text{cmT}^{-1}$). The processed signal exhibits strongly step-like behavior with wide plateaus when the field is oriented close to out-of-plane or close to in-plane direction, separated by sharp transitions. Moreover, the backward sweep does not trace the forward sweep resulting in a hysteretic behavior.

To further elucidate the origin of this unconventional θ-dependence, we have measured the field strength sweeps at selected θ as shown in Figure 1.17. In accordance with the θ-dependence in Figure 1.16b, we see maximum saturation ρ_{xy} ($\rho_{xy,sat}$) when the field is along the film normal and a nearly vanishing $\rho_{xy,sat}$ when the field is in-plane. Moreover, it can be seen that 2 T is not sufficient for saturating the ρ_{xy} at all θ (see e.g. $\theta = 30$ or 150 deg in Figure 1.17), which could explain the hysteresis in the θ-dependence. Another contribution to the θ-dependent hysteresis can be the humps that appear in the hysteresis loops at some θ (see e.g. $\theta = 60$ or 120 deg in Figure 1.17). The origin of these humps is unknown, but possible explanations include i) field-induced non-collinear spin structures that can allow the electrons to acquire a geometric phase in the real space, ii) during the reversal, the Néel vector temporarily orients along a crystal axis with higher AHE conductivity compared to the starting position, and iii) coexistence of two phases with different ρ_{AHE} hysteresis loops.

We have repeated the θ-dependence measurements for stronger fields of 4, 7, and 9 T. Based on the hysteresis loops in Figure 1.17 at 7 and 9 T we expect to be at the

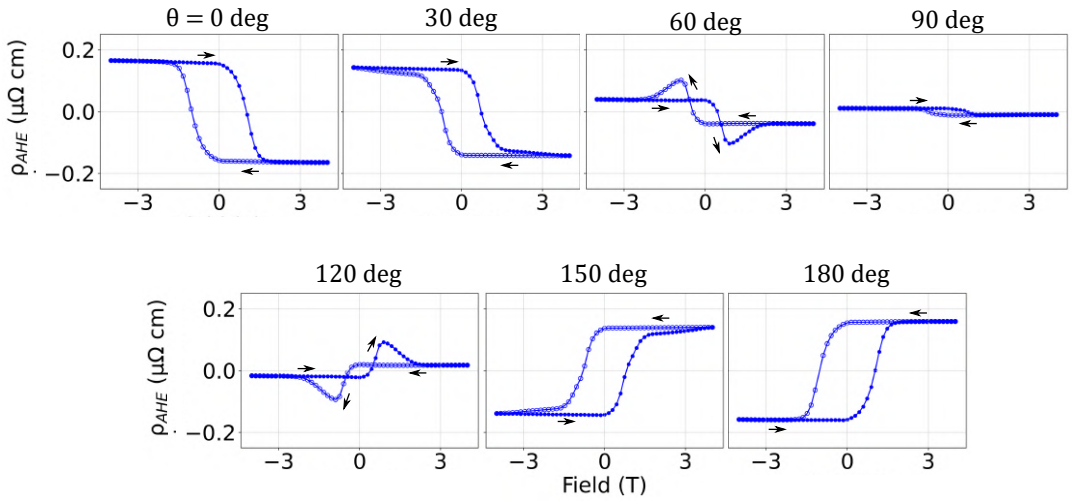

Figure 1.17: The hysteresis loops at selected θ at 110 K with the current channel along the $[2\bar{1}\bar{1}0]$ direction. The sweep direction is again indicated by the small arrows and by the empty circles for the forward sweep and filled circles for the backward sweep. In accordance with Figure 1.16, the AHE resistivity at saturation is at maximum when the field is out-of-plane and decreases when the field rotates away from the out-of-plane, almost vanishing when the field reaches in-plane orientation.

saturation ρ_{AHE} for all θ while at 4 T this should be the case for most θ except for a few (see $\theta = 30$ and 150 deg in Figure 1.17). If the hysteresis in Figure 1.16 relates to the unsaturated **L** or the appearance of the humps at some θ, the 4 T scan should exhibit significantly less hysteresis, and 7 and 9 T vanishing hysteresis. The step-like behavior, on the other hand, we would expect to persist as for all θ the $\rho_{AHE,sat}$ is not significantly different between 2, 4 and 7 T in Figure 1.17. The θ-scans for 4, 7 and 9 T fields are shown in Figure 1.18a but instead of ρ_{AHE} we have plotted $\sigma_{AHE} = \rho_{AHE}/\rho_{xx}^2$ to normalize the signal with respect to field-induced changes in ρ_{xx}. The behavior is as expected from the predictions based on the hysteresis loops - the plateaus around the in-plane and out-of-plane directions of the field separated by the steep steps persist, while the hysteretic behavior disappears when the field strength is increased. Moreover, there are slight changes in σ_{AHE} amplitude for the different field strengths, which likely is an artefact originating from slight differences in the experimental conditions between the measurements (Hall bar orientation, wirebonding, temperature) and/or from the extraction of the OHE background.

All in all, our measurements on the θ-dependence show two important features. First, since the AHE resistivity is strongly varying with the field orientation we can infer that the **L**-orientation is varying, too. The mechanism through which the field can couple to the **L**-vector is not known to us but for our purposes it suffices to know that we are able to re-orient the **L**-vector using a field of the order of a few Tesla, which is easily reachable with our measurement set-up. This enables a more detailed study of the AHE anisotropy in our Mn_5Si_3 films, which for example in RuO_2 is less accessible due to the field strengths

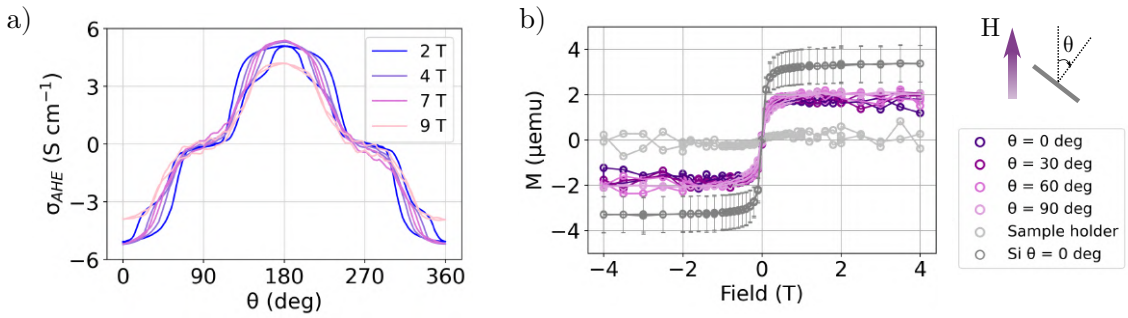

Figure 1.18: a) The θ-dependence of σ_{AHE} with different external field strengths at 110 K. Here, the current channel is along the $[2\bar{1}\bar{1}0]$ direction. The step-like behavior persists while the hysteresis vanishes and the amplitude decreases when the field is increased. b) The magnetisation of a continuous stack of Mn_5Si_3/MnSi/Si (purple tones) as a function of the field strength and orientation θ, as well as the signal from a bare Si substrate (the error of $\sim 24\%$ originates from the area calculation of the two samples and the normalization of the substrate data to the Mn_5Si_3/MnSi/Si area) and the sample holder. The θ here is the same as for the magnetotransport data but subject to more uncertainty as the field alignment is realized manually rather than automatically.

of the order of 60 T required for re-orienting the **L**-vector. Second, the anisotropic and unconventional θ-dependence suggests altermagnetism in our Mn_5Si_3 thin films rather than a weakly ferromagnetic phase, which could also cause the observation of AHE in compensated magnets. Typical soft and polycrystalline ferromagnets typically exhibit a $\cos\theta$ behaviour as the AHE amplitude can be approximated as being proportional to the out-of-plane component of the magnetisation. There are, however, a few exceptions. Ferromagnets with a strong magnetocrystalline anisotropy can show a more step-like θ-dependence as the magnetisation prefers to remain aligned with the easy axes and hence lags behind the field. However, a strong field overcoming the anisotropy energy restores the $\cos\theta$-dependence. In single crystalline ferromagnets, the intrinsic AHE conductivity can depend on the magnetisation orientation relative to the crystal axes as has been shown both experimentally [96][97] and theoretically by *ab initio* calculations [88]. This variation has been attributed to changes in the band structure near the Fermi level upon rotating the magnetisation direction [88]. However, as the Hall vector is allowed by symmetry for any magnetisation orientation, the AHE conductivity cannot be 'switched off'. This is contrary to what we observe in our films: for θ ranging roughly from 0 to 40 deg, $70-110$ deg, $180-210$ deg and so on as shown in Figure 1.16, $\rho_{AHE} \sim 0$. Note that ρ_{AHE} saturates at the field strengths used for the θ-dependence as shown in Figure 1.17 implying that it is unlikely that the **L**-vector is lagging behind the field. As discussed earlier, in altermagnets the switching off of the AHE is allowed [39][64][43][61] for more orientations than exactly $\theta = 90$ deg as is the case with ferromagnets, meaning that the θ-dependence we observe adds to the evidence that Mn_5Si_3 epitaxial films are altermagnetic.

Control measurement I: Magnetisation as a function of field orientation

In order to further show that the weak magnetisation (discussed previously in Section 1.4.3) is not the origin of the AHE in our samples we have measured the magnetisation as a function of θ with the SQUID magnetometer. The measurement set-up allows for temperatures ranging from 2 to 400 K and fields upto 7 T, enabling the magnetic measurements to be run under similar conditions to the magnetotransport measurements. The field-dependence of the magnetisation in the continuous unpatterned Mn_5Si_3/MnSi films on Si substrate is shown in Figure 1.18b for different orientations θ of the field. The definition of θ here is the same as for the magnetotransport measurements. It should be noted, however, that here the change in the field orientation is realized through manual re-orientation of the sample relative to the sample holder while in the magnetotransport measurements an automatized rotator is used, meaning that the accuracy in the θ may differ. However, as we can see in Figure 1.18b, the θ has virtually no influence on the weak magnetisation of the Mn_5Si_3/MnSi stack so that the slight inaccuracies in setting the θ in the magnetic measurements are not critical. Recall from Section 1.4.3 that the non-zero magnetic signal has contributions from both the Mn_5Si_3 film and the Si(111) substrate and as the signal is very small it can also contain other spurious magnetic signals [83]. Comparing the substrate signal to the Mn_5Si_3/MnSi/Si signal (former has been normalized to the area of the Mn_5Si_3/MnSi/Si sample; Mn_5Si_3/MnSi/Si and Si sample areas are 0.12 and 0.16 cm^2, respectively) implies that the signal from the Mn_5Si_3/MnSi is likely of the order of 0.02 μ_B/Mn for all θ, showing that there is no variation in the magnetisation with θ that would resemble the variation of ρ_{AHE} with θ, making a strong case against the weak magnetisation being the origin of the AHE in our Mn_5Si_3 epitaxial films.

Control measurement II: θ-dependence of AHE in antiferromagnetic Mn_5Si_3

As a second control measurement we have probed the magnetotransport measurements of Mn_5Si_3 epitaxial films with a larger proportion of MnSi (75 % of Mn_5Si_3, 25 % of MnSi). When the MnSi content is increased the crystallinity of the Mn_5Si_3 deteriorates and becomes more textured [2], which in effect will prohibit the altermagnetism as the strain can relax at the grain boundaries. Even if the different grains were altermagnetic, the emergent magnetotransport properties would average out due to the different grain orientations. We would therefore expect these films to exhibit a conventional antiferromagnetic phase, making them relevant control samples as they should not show any AHE. This is demonstrated in Figure 1.19 where the field dependence of σ_{AHE} of the 75:25 sample shows a significantly reduced amplitude as well as a vanishing coercivity. Note that here we are plotting $\sigma_{AHE} = \rho_{AHE}/\rho_{xx}^2$ instead of ρ_{AHE} in order to draw a more direct comparison between the two samples. The θ-dependence of the σ_{AHE}, on the other hand, shows roughly a $\cos\theta$ behavior, which is in stark contrast with that of the 96:4 sample as

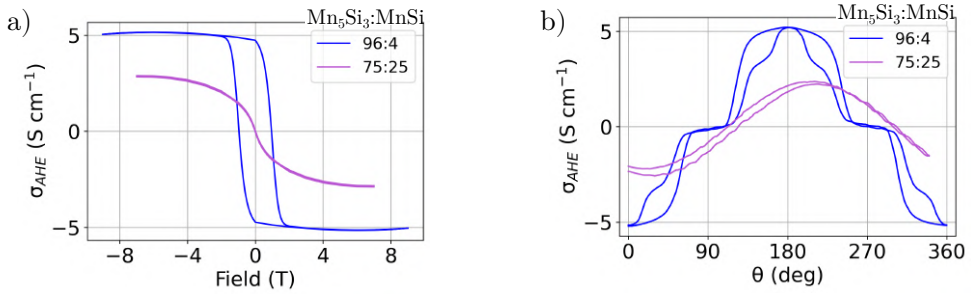

Figure 1.19: a) AHE conductivity as a function of the field in epitaxial films of different proportions of Mn_5Si_3 and MnSi. The AHE amplitude and coercivity become suppressed when the MnSi content is increased. b) The unconventional behavior of AHE as a function of the external field orientation disappears when the MnSi content increases and is replaced with a more conventional $\cos\theta$ behavior. Note that the data for the 75:25 sample is slightly shifted due to a slight mechanical hysteresis during the sample rotation.

shown in Figure 1.19b. This non-zero signal could originate from a ferromagnetic component in the films, which has to be verified with further magnetic measurements on the 75:25 sample. These results demonstrate that the anisotropic AHE requires a high crystal quality of the Mn_5Si_3 epitaxial films, which is consistent with the origin of the altermagnetism being in the underlying crystal structure. Moreover, if the origin of the AHE signal in the 96:4 sample was the ferromagnetic MnSi (given that its T_c was increased from 50 to at least 110 K by the epitaxy), we would expect the σ_{AHE} to be higher for the 75:25 sample, which here is not the case.

1.5.3 Further anisotropy revealed by external field rotation in different crystal planes

Next we explore the anisotropic AHE further by adding an additional degree of freedom to our measurements, namely the orientation of the current channel of the Hall bars relative to the underlying crystal structure. Previously, the measurements corresponded to a Hall bar along the $[2\bar{1}\bar{1}0]$ direction meaning that the field is rotated in the $(2\bar{1}\bar{1}0)$ plane. We have, however, patterned our epitaxial films in such a way that they contain Hall bars along the various high-symmetry axes of the hexagonal crystal structure, namely those including and equivalent to the $[01\bar{1}0]$ and $[2\bar{1}\bar{1}0]$ axes (recall Figure 1.6a). The Hall bar orientation is defined by the angle α between the $[01\bar{1}0]$ and the current channel direction as shown in Figure 1.20a. During the measurements, the field is again maintained in the plane perpendicular to the current channel, meaning that for the different Hall bars the field rotates in different crystal planes and in effect, so does the **L**-vector. This allows us to further study how the AHE evolves as a function of the **L**-orientation.

The θ-dependence (with a 2 T field, at 110 K) of the different Hall bars is shown in Figure 1.20. We again observe strongly step-like behavior for all α but the exact details of the behavior divide the α into two sets: 1) θ-dependence is virtually identical to that

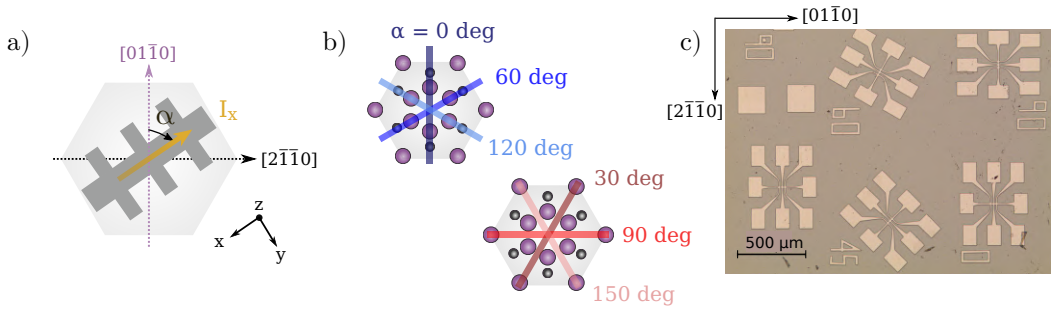

Figure 1.20: a) The Hall bar orientation is defined by α, which is the angle between the crystal axis $[01\bar{1}0]$ and the current channel direction. b) The α selected for this work reflecting the hexagonal crystal symmetry of the Mn_5Si_3 films. They can be divided into two sets based on the crystal axes along which the current channel is - for $\alpha = 0$, 60, and 120 deg along $[01\bar{1}0]$ or equivalent and for $\alpha = 30$, 90, and 150 deg along $[2\bar{1}\bar{1}0]$ or equivalent (see also Figure 1.6a). c) Optical image of the nanofabricated Hall bars after optical lithography and ion beam etching steps showing the Hall bars with $\alpha = 0$, 45, 60, and 90 deg.

observed in the previous Section i.e. wide plateaus when the field is out-of-plane or in-plane and sharp transitions in-between, and 2) θ-dependence contains small additional steps when the field is around the in-plane direction. Recall that even without probing the θ-dependence we could divide the α into two sets based on the crystal plane in which we rotate the field, so the fact that we observe different θ-dependence for these two sets of α strongly supports our earlier conclusion that along with the field we are also rotating the **L**-vector in different crystal planes. This also provides further evidence on the anisotropy of the ρ_{AHE} with respect to **L**-orientation and its relation to the crystal structure. Also, note that we are rotating the field in a plane perpendicular to the current channel so that the non-crystalline contributions to the signal are minimized.

Next, we elucidate whether the anisotropy in the θ-dependence for the different Hall bars relates to the change in the crystal axis along which the current channel is oriented or to the change in the crystal plane in which the external field rotates. In order to do so, we have conducted additional measurements where two perpendicular Hall bars are measured simultaneously while the external field is rotated in a given crystal plane as illustrated in Figure 1.22. These measurements have been carried out by Antonin Badura at the Czech Academy of Sciences in Prague. The outcome of these measurements, shown in Figure 1.22, clearly demonstrates that the shape of the θ-dependence stems from the different crystal planes in which the field (and in effect, **L**-vector) is rotated and is virtually independent of the exact orientation of the current channel with respect to the crystal structure.

Finally, we conduct a measurement where we rotate the external field in the plane of the film, which supports the earlier observations while revealing additional peculiarities: ρ_{xy} is vanishingly small as expected from Figure 1.21 where $\rho_{xy} \sim 0$ when $\theta = 90$ deg but interestingly shows sharp peaks at $\phi \sim 0$, 60, 180, and 240. Similar sharp peaks have

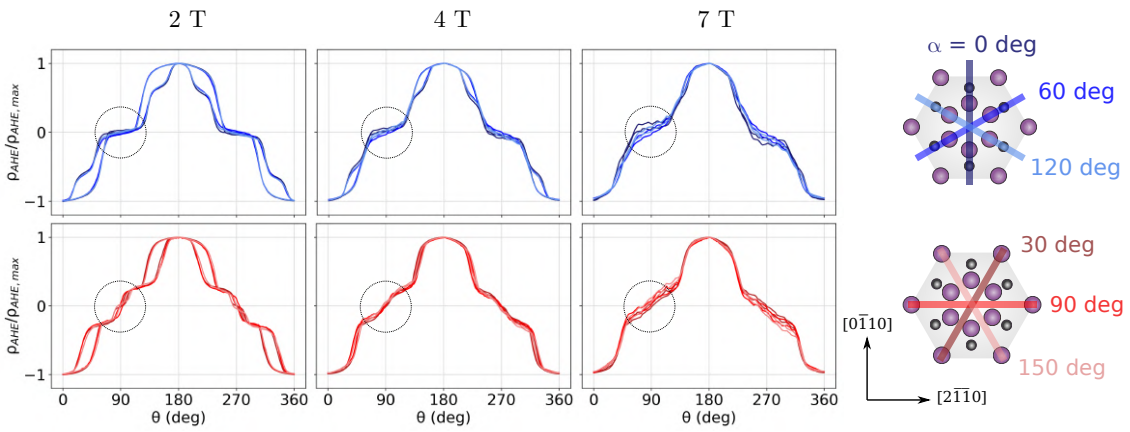

Figure 1.21: The θ-dependencies of the Hall bars with different α (at 110 K) using varying field strengths. The α can be divided into two sets based on the crystal axis along which the current channel is oriented (which determines the crystal plane in which the field rotates) and the exact details of the θ-dependency - some show a wide plateau when the field is in-plane (top, blue tones) while the others show additional steps at the same field orientation (bottom, red tones). Increasing field strength results in a disappearing of the hysteresis behaviour.

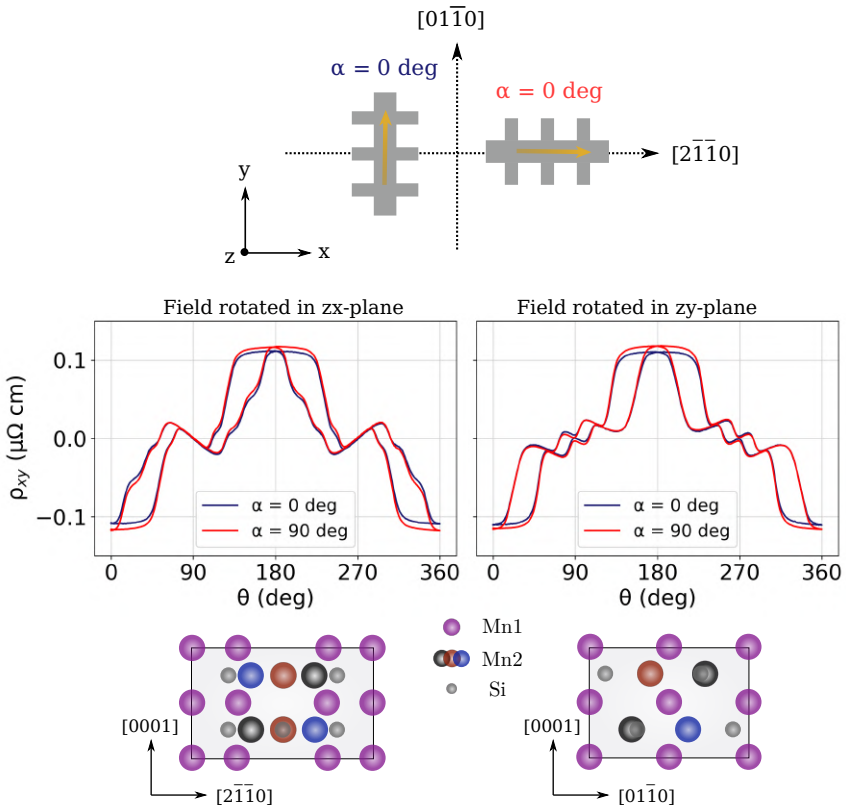

Figure 1.22: Simultaneous measurement of two perpendicular Hall bars at 100 K with 2 T field reveals that the anisotropic θ-dependence relates to the crystal plane in which the field rotates (shown below the corresponding plots) rather than the crystal axis along which the current channel is. Note that the data presented here still contains the OHE-background, hence the y-axis is ρ_{xy} rather than ρ_{AHE}.

been theoretically associated with the opening and closing of Dirac points in CuMnAs upon **L**-vector rotation [98], but in our system the origin of these peaks remains a point of further investigation. The $AMR_{||}$ (defined in Equation 1.7), on the other hand, shows six-fold symmetry and based on previous reports of the in-plane $AMR_{||}$ in hexagonal systems [99][100], this is in good agreement with the hexagonal symmetry of the crystal plane in which we are rotating the field. This again indicates that **L**-vector rotates upon the external field rotation. In MnTe, where the $AMR_{||}$ was measured in a Corbino disk geometry thus eliminating the non-crystalline contributions, the peaks (dips) correspond to the **L**-vector pointing along $[1\bar{1}00]$ ($[2\bar{1}\bar{1}0]$) [100]. In our measurements, however, the non-crystalline contributions are present and have to be subtracted in order to realize a cleaner analysis of the crystalline contribution. This can be realized either through measuring perpendicular Hall bars and summing up their signals, in which case the non-crystalline contributions cancel out [101], or through measurements in the Corbino geometry [102].

1.5.4 Anisotropic magnetoresistance in different crystal planes demonstrates Néel-vector control

Studying the longitudinal resistivity (ρ_{xx}) of a magnetic material is another tool for probing information on properties such as the magnetocrystalline anisotropy or the order parameter orientation. As discussed earlier in this Chapter, ρ_{xx} is described by the symmetric part of the resistivity tensor and is an even function of the magnetisation. This means that the phenomena relating to ρ_{xx} are allowed by symmetry in ferromagnets, antiferromagnets, and altermagnets, which was not the case for the antisymmetric components of the resistivity tensor. One example of these phenomena is the anisotropic magnetoresistance (AMR) where the magnetisation orientation relative to the current direction and the crystal structure determines the longitudinal resistance of the system. The longitudinal AMR relates to ρ_{xx} as:

$$AMR_{||}(\theta) = \frac{\rho_{xx}(\theta) - \langle\rho_{xx}\rangle}{\langle\rho_{xx}\rangle}, \tag{1.7}$$

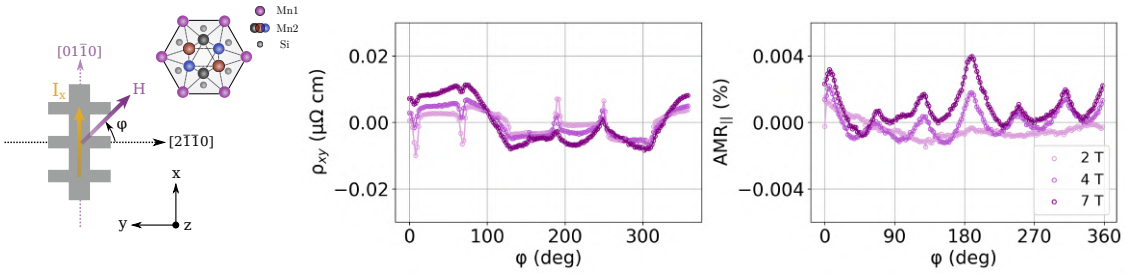

Figure 1.23: The dependence of ρ_{xy} and $AMR_{||}$ (ρ_{xx}) on the in-plane orientation of the external field quantified by the angle ϕ, which is the angle between H and $[2\bar{1}\bar{1}0]$ crystal axis. The measurements are conducted at 110 K under varying field strengths.

where $\langle \rho_{xx} \rangle$ indicates ρ_{xx} averaged over all angles. The total AMR signal can be expressed as:

$$AMR_{||} = C_I \cos 2\phi + C_2 \cos 2\theta + C_4 \cos 4\theta + C_6 \cos 6\theta + C_{I,4} \cos(4\theta - 2\phi), \qquad (1.8)$$

where ϕ is the angle between current and magnetisation, and θ is defined as the angle between magnetisation and [0001] crystal axis (in our case) [103]. These terms can be classified into crystalline, non-crystalline and mixed terms, where the crystalline terms depend on θ while the non-crystalline terms depend on ϕ. In Equation 1.7 the first term is non-crystalline, the second, third, and fourth terms are the uniaxial, cubic, and hexagonal crystalline terms, and the last term is a mixed crystalline/non-crystalline term. Microscopically, the relativistic non-crystalline contribution arises from the changing s-d scattering cross-section when the angle between the current and the magnetisation directions is changed while the crystalline contribution relates to the changing band structure when the magnetisation orientation changes relative to the underlying crystal structure. The former contribution can be eliminated by rotating the magnetisation in a plane perpendicular to the current channel ($\phi = \pi/2$), which is the case for our measurements. This leaves only the crystalline contribution in the signal, which can then be used to extract information about the crystal structure of the system.

The θ-dependence of the $AMR_{||}$ for $\alpha = 0$, 60, 120 deg and α = 30, 90, 150 deg Hall bars is shown in Figure 1.24 for 2, 4, and 7 T. At 2 T for all α the θ-dependence is roughly $\cos 2\theta$-like while at 4 and 7 T two distinct behaviors emerge for the two sets of α: for α = 0, 60, and 120 deg the θ-dependence still follows a $\cos 2\theta$ behavior but for α = 30, 90, and 150 deg higher order cos components appear. To illustrate the two different behaviors, we fit the θ-dependence of $\alpha = 0$ and 90 deg in Figure 1.25 using a fitting function:

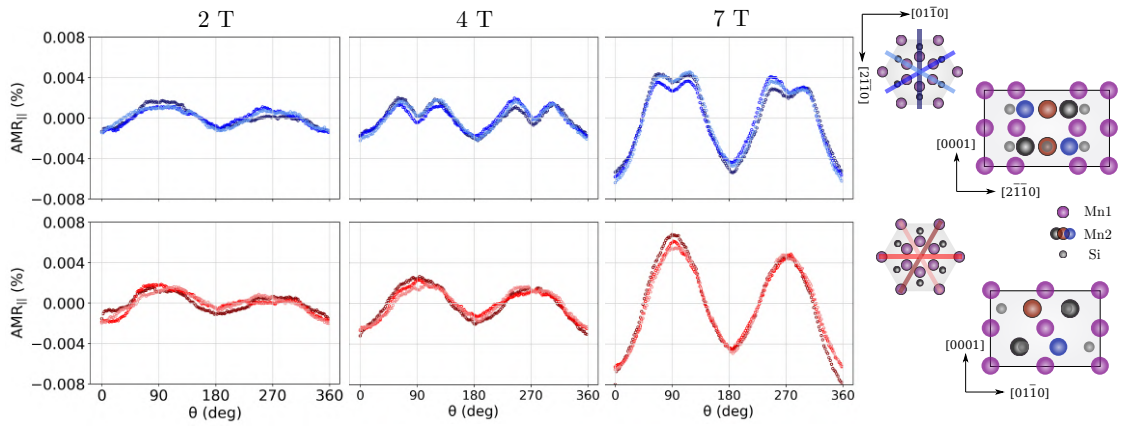

Figure 1.24: The θ-dependence of the longitudinal AMR ($AMR_{||}$) at 110 K and under varying field strengths (2, 4, and 7 T). Two distinct behaviors can be distinguished above 4 T, one with (blue tones) and one without (red tones) sizable higher order cos-components. The two sets correspond well to the two sets of crystal axes along which the current channels are oriented.

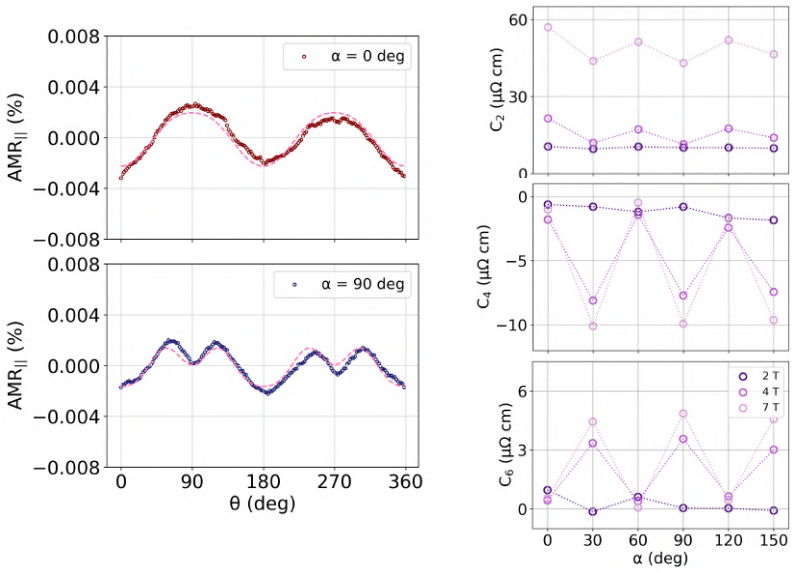

Figure 1.25: The fitting of the $AMR_{||}$ as a function of θ using the fitting function containing cosines of different orders as introduced in the main text. This highlights the evidently different behaviors of $\alpha = 0$ and 90 deg. The fitting parameters obtained from the fits illustrated on the left as a function of α. For each α the C_2 component is constant while C_4 and C_6 oscillate from virtually zero to non-zero with a 60 deg periodicity.

$$AMR_{||}(\theta) = C_0 + C_2 \cos 2\theta + C_4 \cos 4\theta + C_6 \cos 6\theta, \tag{1.9}$$

where C_n are the fitting parameters for the different cosines and the terms running up to $n = 6$ reflect the hexagonal symmetry of our system. Plotting the C_n as a function of α as shown in Figure 1.25b clearly shows the 60 deg periodicity in the (dis)appearance of the higher order cos-components in the AMR signal, which agrees with the hexagonal symmetry. Given that the crystalline component of the AMR (which is expected to dominate here) reflects the crystal plane in which the order parameter is rotating, this once more supports the conclusion drawn from the previous measurements on ρ_{AHE} that for the different α we rotate the **L**-vector in different crystal planes. An interesting observation is that the two different behaviors emerge only above 2 T, whereas previously in Section 1.4.5 we have seen that 2 T is sufficient for reversing the **L**-vector orientation.

The main findings described so far are two-fold. First, changing the plane in which the external field is rotating influences both the AHE and AMR, which indicates that by changing the field orientation we are also changing the **L**-vector orientation. Secondly, as AHE depends on the Néel vector orientation even when saturation has been reached, our results suggest that AHE in our epitaxial Mn_5Si_3 films is intrinsically anisotropic. This adds to the evidence that the films indeed belong to the altermagnetic group. For a better understanding of these results, our collaborators Dr. Libor Smejkal and Prof. Helen Gomonay *et al.* are conducting calculations on the Berry curvature on the different crystal planes as well as on the possible reversal mechanisms of the **L**-vector. A publication on our experimental results with the supporting theoretical calculations is currently under preparation.

1.6 Unfolding the Néel vector switching dynamics in epitaxial Mn_5Si_3 through further transport measurements

The broken $\mathscr{T}$-symmetry of altermagnets and the consequent magnetotransport properties thought to be exclusive to ferromagnets open up new opportunities for studying the properties of compensated magnets. In this Section we illustrate this point by showing transport measurements based on AHE that have been previously possible only in ferromagnets. First, we obtain more information on the switching mechanism through minor-loop measurements and then discuss the possibility of extracting the energy barrier for **L**-vector reversal using dynamic switching measurements.

1.6.1 Obtaining information on intermediate switching states through minor loop measurements

Here we study the microscopic details of the switching of the **L**-vector more closely using the minor loop measurement technique. So far the field sweeps shown in this Chapter have all been major loops, meaning that the saturation field is exceeded in both forward

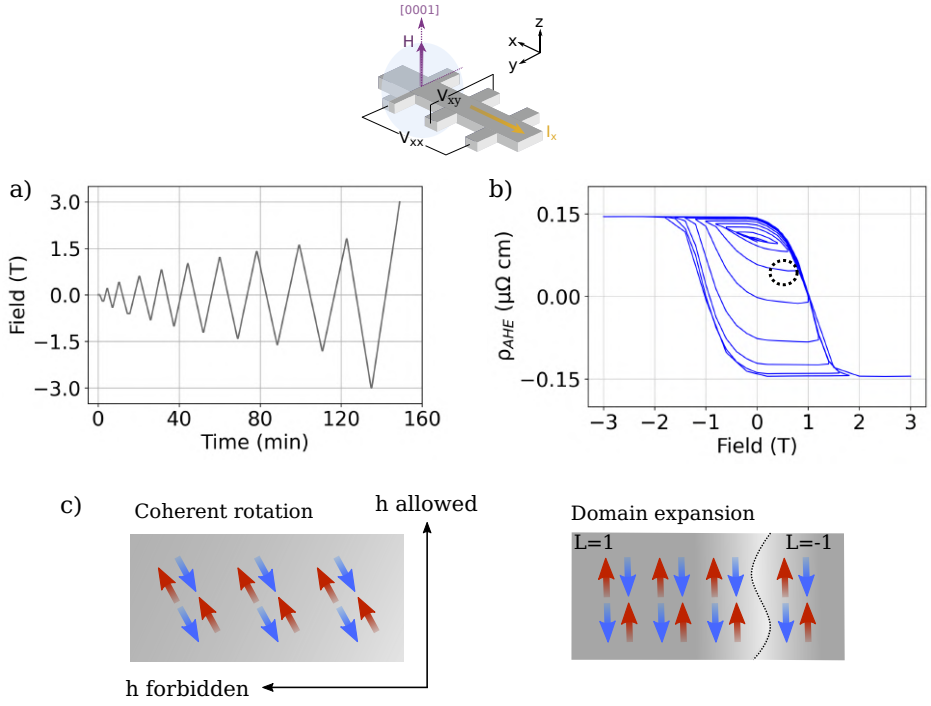

Figure 1.26: a) The field-sweep sequence starting from 0 T and gradually increasing up to 3 T at each field sweeping cycle. b) The resulting hysteresis loop with various minor loops at intermediate ρ_{AHE} accessed at each cycle. c) Two possible scenarios of the spin configuration that could correspond the intermediate states circled in (b): i) coherent rotation of **L**-vector results in a change in the **L**-vector components along crystal axes with allowed and forbidden **h**, and ii) Fraction of the sample has switched completely giving ρ_{AHE} of opposite polarity while the rest remains unswitched.

and backward sweeps so that a complete reversal of the **L**-vector is likely. We can, however, obtain more information about the switching mechanism by measuring minor loops where the extreme sweeping fields stay below the saturation field and therefore only a partial **L**-vector switching will be realized. In ferromagnets the presence of minor loops often relates to magnetisation switching through domain nucleation and subsequent domain wall propagation [104][105][106] while in altermagnets the minor loop behavior has not been reported until now. Recall that it is so far unknown to us how the **L**-vector reverses, but the different options include the spin-flop mechanism common for antiferromagnets, continuous rotation relying on the DMI terms as was the case with RuO_2 [43], or through an unconventional coupling of the field to the d-wave anisotropy order parameter. Moreover, whether the reversal takes place coherently or through a domain expansion is an open question. Ideally, the answer to these questions could be found using domain imaging techniques [107] and/or vector magnetometry in order to study the field-induced canting of the sublattice moments [43], but we can obtain clues to these question through minor loop measurements as shown in this Section.

In order to study the minor loops, we carry out a field sweep with the maximum field gradually increasing after each loop as shown in Figure 1.26ab. Here the field is always along the film normal, the current channel is parallel to the $[2\bar{1}\bar{1}0]$ crystal axis ($\theta = 0, \alpha =$ 90 deg) and the temperature is 110 K. As shown in Figure 1.26b, we observe that this field sequence allows us to access at each loop a different intermediate state characterized by ρ_{AHE} in-between the two saturation values. The nature of these intermediate states is unclear but two possible scenarios are illustrated in Figure 1.26c: i) the **L**-vector rotates coherently so at the progressive intermediate states the component along a crystal axis that allows a non-zero **h**-vector (recall that **h** contains the Hall conductivities) decreases while the component along a crystal axis that forbids the **h**-vector increases, or ii) the **L**-vector reversal propagates through domain expansion so that at the intermediate states a fraction of the sample has the opposite **L**-vector orientations and hence opposite ρ_{AHE} polarity. This results in a partial cancellation of the net ρ_{AHE} signal. More information on the viability and likelihood of these two scenarios could be obtained by studying the dynamic properties of the minor loops through for example measurement at varying sweep rates [106] or measurement of successive loops with the same extreme field [105]. The stability of the intermediate states as well as the time-scale of their dynamics could help support and/or exclude one of the proposed scenarios.

1.6.2 Understanding the switching dynamics via rate-dependent coercivity

The coercivity of ferromagnets is known to depend on the rate at which the external field is swept as illustrated in Figure 1.27. Qualitatively this can be understood as follows: in order to switch its direction the magnetisation has to overcome an energy barrier with a

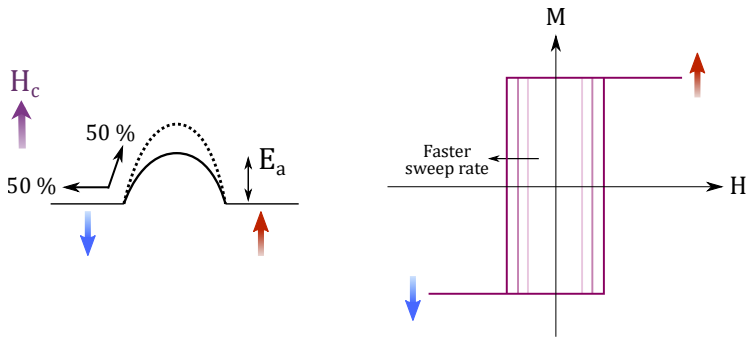

Figure 1.27: Illustration of the dynamic switching measurements. Switching of the magnetisation direction requires surmounting an energy barrier E_a, which can be lowered with an external field. At a coercive field (H_c) half of the switching attempts are successful. The H_c depends on the time the system is allowed to attempt the switching and therefore faster sweeping rate will increase the H_c while the opposite is true for slower sweep rate.

height that depends for example on the magnetocrystalline anisotropy and the switching mechanism of the system. An external field will assist in the switching by lowering the energy barrier and the field strength at which the probability of overcoming the barrier is 50 % is referred to as the coercive field. However, this probability does not only depend on the height of the barrier but also on how long the overcoming can be attempted - when the rate at which the field is swept is slow the system will spend more time at each field step, which will allow more attempts at overcoming the energy barrier for switching whereas the opposite is true for a faster sweeping rate. This means that a faster sweeping rate will result in a larger coercive field and vice versa.

Originally, the dynamic switching measurements were applied for the net magnetisation measurements at different field sweep rates but they are equally applicable to magnetotransport measurements at varying sweep rates as has been shown for the ferromagnetic complex oxide $SrRuO_3$ [108]. Here, we follow the example of Ref. [108] and measure the AHE as a function of the field strength under varying field sweep rates (between 3 and 100 Oes^{-1}). For the sake of consistency and in order to remain in the phase showing AHE, the measurement temperature is 110 K. Note that instead of recording the entire hysteresis loop, here it is sufficient to only record the forward sweep (3 to -3 T) in order to see the change in the coercive field. As shown in Figure 1.28 we run the measurements on a Hall bar with a current channel along the $[2\bar{1}\bar{1}0]$ and the external field along the film normal ([0001]) ($\alpha = 90$ deg, $\theta = 0$ deg). The field is swept from 0 to -2 T in steps of 0.1 T and at each step the ρ_{xy} and ρ_{xx} are measured during a fixed measurement time (t_M) of 1 s unless otherwise stated.

The effect of the field sweeping rate on the field dependence of ρ_{AHE} is shown in Figure 1.28a where we observe a widening of the forward loop with an increasing sweep rate as expected. This is even more apparent in Figure 1.28b where we plot the coercive field (H_c) as a function of the sweep rate. As also shown in Figure 1.28b, we have checked that there is no systematic influence of t_M on H_c since for the fastest sweeping rates the

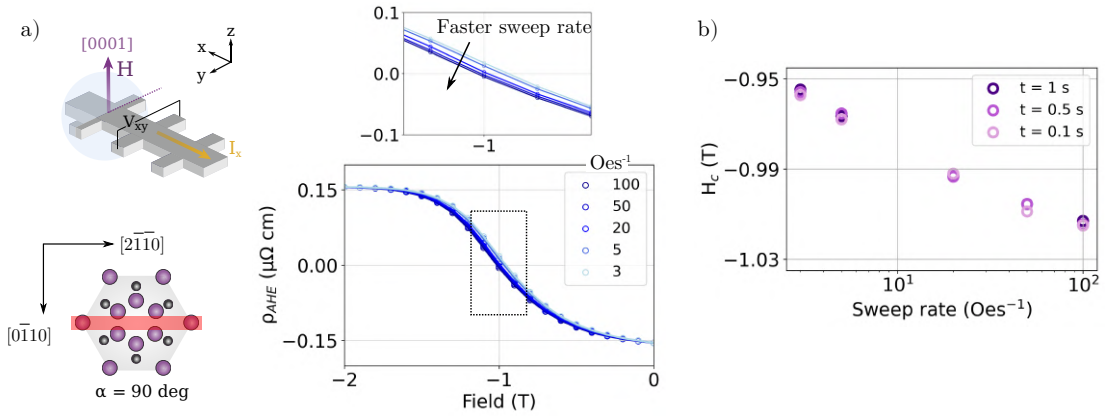

Figure 1.28: a) Measurement of the dynamic coercive field at varying field sweep rates at 110 K for a Hall bar along the $[2\bar{1}\bar{1}0]$ crystal axis ($\alpha = 90$ deg) with the external field along [0001] axis ($\theta = 0$ deg). A faster sweep rate results in a larger coercive field as expected based on the theory developed for ferromagnets - faster sweeping allows the system less time for attempting overcoming the energy barrier for switching. b) The impact of measurement time on the sweep rate dependence of the coercive field. Compared to the effect of the sweep rate the effect of the measurement time is negligible indicating that the trend we observe is not an experimental artefact.

t_M of 1 s is more comparable to the sweeping time between steps (t_S=10 s) than for the slowest sweeping rate (t_S = 333 s). The trend in Figure 1.28b contains useful information about the energy barrier of switching in our Mn_5Si_3 epilayers but in order to access this information, an appropriate fitting function has to be devised. Next, we will discuss the fitting function derived for generic ferromagnets and its applicability to our system.

In search of a fitting function for the dynamic coercivity

The relationship between the sweeping rate and the coercive field has been derived for example by Peng and Richter in Ref. [109] for a step field and their derivation is briefly summarized here.

We consider a system with N_0 macrospins in total, all of which are initially magnetized in the positive (+) direction. The rate at which the spins are reversed to point away from the positive direction (so towards the negative direction) is given by

$$\frac{dN_+}{N_+} = -P(f_0)dt, \tag{1.10}$$

where N_+ is the number of moments along the positive direction, P is the probability of switching, f_0 is the attempt frequency, and dt is the time step. For antiferromagnets, the f_0 has been estimated to be of the order of 10^{12} s^{-1} [110][111]. In the framework of the Arrhenius-Néel formalism, the switching probability can be expressed as:

$$P = f_0 \exp\left(\frac{-\Delta E}{k_B T}\right), \tag{1.11}$$

where ΔE is the switching energy barrier. This barrier depends on the details of the system as well as the reversal mechanism. If we assume a Stoner-Wohlfarth type of field-assisted switching via coherent rotation for a system with uniaxial anisotropy, we can use

$$\Delta E = K_u V \left(1 - \frac{H}{H_0}\right)^n. \tag{1.12}$$

Here, K_u is the uniaxial anisotropy constant, V is the switching volume, and H_0 is the intrinsic coercivity in the absence of thermal fluctuations. The power n depends on the orientation of the easy axis of the system - for a material with perpendicular magnetic anisotropy $n = 2$ while for an in-plane easy axis $n = 3/2$. It should be noted that these values assume that the field is parallel to the easy axis direction [112].

For a case of a 'step field' (i.e. applying a field for a specific duration of time) the time-dependent magnetization is:

$$m(t) = \frac{N_+ - N_-}{N_0} = \frac{N_+ - (N_0 - N_+)}{N_0} = \frac{2N_+}{N_0} - 1 \tag{1.13}$$

Recalling Equations 1.10 and 1.11, we obtain

$$m(t) = 1 - 2\exp[-P(f_0)t_S]. \tag{1.14}$$

We can find an expression for the coercive field using Equation 1.12 and recalling that at $H = H_c$ half of the moments have switched so that $m(t) = 0$:

$$H_c = H_0 \left(1 - \left[\frac{k_B T}{K_U V} \ln \frac{f_0 t_S}{\ln 2}\right]^{1/n}\right). \tag{1.15}$$

The experimentally relevant sweeping rate R_H can be introduced in the equation through the substitution $t_S = \Delta H / R_H$, where ΔH is the field step size:

$$H_c = H_0 \left(1 - \left[\frac{k_B T}{K_U V} \ln \frac{f_0 \Delta H}{R_H \ln 2}\right]^{1/n}\right). \tag{1.16}$$

Applying Equation 1.16 to our system is not trivial as its derivation is based on various assumptions that might not be applicable. Firstly, the anisotropy of our Mn_5Si_3 epitaxial films is so far not well understood - the *ab initio* calculations indicate an easy axis along the $[11\bar{2}1]$ direction while the [0001] is the hard axis and $[1\bar{1}00]$ and $[11\bar{2}0]$ axes are intermediate axes. Similar results were obtained in the collinear phase of the bulk Mn_5Si_3: *ab initio* calculations suggest a biaxial anisotropy with a primary easy axis along the b-axis ($[1\bar{1}00]$) and secondary easy axis along the c-axis ([0001]), and a hard axis along the a-axis $[11\bar{2}0]$ [73]. Note that there can be differences between the exact magnetocrystalline anisotropies of the bulk and epitaxial Mn_5Si_3 due to the different crystal structures, but the main observation is that the anisotropy of the system is unlikely to

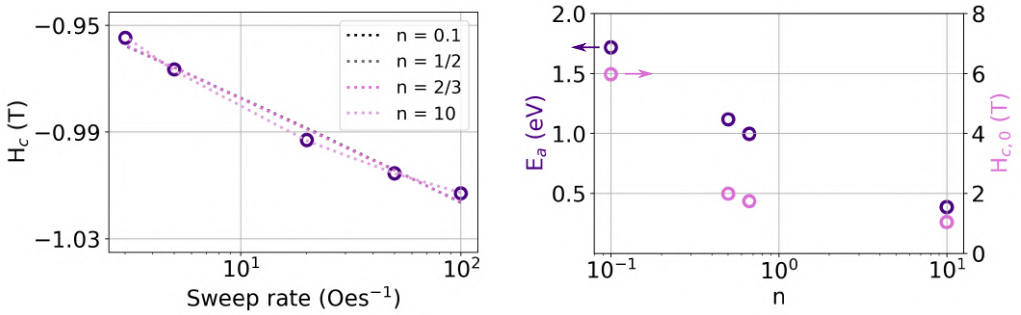

Figure 1.29: The effect of external field sweeping rate on the coercive field H_c fitted with Equation 1.16 using different values of n. The fitting parameters, namely the activation energy E_a and the intrinsic coercive field $H_{c,0}$ extracted using these fitting functions are shown on the right. The fitting functions equipped with different n all fit the data well but return markedly different values for the fitting parameters.

be uniaxial. This means that the expression for the switching energy barrier (Equation 1.12) should be adapted to include higher-order anisotropy terms. Further adjustments to Equation 1.12 might be necessary to account for the reversal mechanism.

In order to see to what extent the Equation 1.16 is suitable for our system, we try to use it to fit the trend in Figure 1.28b. As the anisotropy of our system is unknown, it is unclear which n we should opt for - as a remedy we have attempted to fit the data with various values of n as shown in Figure 1.29. The values $n = 1/2$ and 3/2 correspond to ferromagnets with a perpendicular magnetic anisotropy and easy-plane anisotropy, respectively, while $n = 0.1$ and 1 are selected to represent extremities (that might not be physically feasible) so as to understand the range of n that return a good fit. As can be seen in Figure 1.29, each n seems to be a good fit for the trend yet yield very different values for the fitting parameters E_a and $H_{c,0}$ that are nevertheless in the same order of magnitude.

Based on how realistic the $H_{c,0}$ values that the fits return are, we can make an educated guess on the optimal choice for n: as the $H_{c,0}$ is the coercive field at zero temperature i.e. without the assistance of thermal fluctuations, it should be markedly larger than the H_c at 110 K so that we can exclude the $n = 1$ (returns $H_{c,0} = -1$ T) as an unlikely option. Similarly unlikely seems the $H_{c,0}$ that is six times larger than the H_c at 110 K and therefore $n = 0.1$ might not be the best option for the fitting function. On the other hand, $n = 1/2$ and $3/2$ return fits with realistic $H_{c,0}$ values and the difference between the values of the two fits is not drastic. The values for E_a indicating the height of the energy barrier for a switching event are in the eV range, which is in a good agreement with E_a in other magnetic systems with varying anisotropies and reversal mechanisms [108][113]. However, it should be borne in mind that these values are only indicative and not to be taken as exactly accurate for our system. We can nevertheless use the fits to obtain qualitative information about the system as will be discussed next.

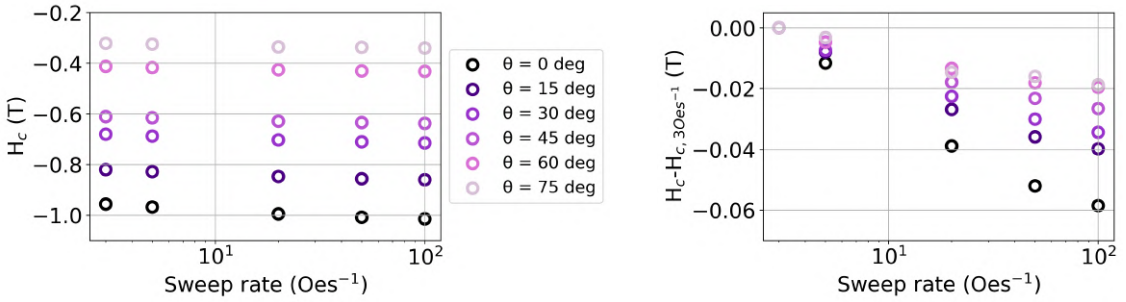

Figure 1.30: The θ-dependence of the dynamic coercivity. In general, for all sweeping rates the absolute coercive fields H_c decrease when θ is increased. In addition, the slope of the H_c vs. sweep rate decreases with increasing θ. Fitting this data would require a fitting function adapted to the situation where the switching does not occur along the easy axis.

Angular dependence of the dynamic coercivity

Here, we have repeated the measurement of dynamic coercivity for different external field orientations θ in order to further probe the anisotropy of the system by observing the evolution of E_a as a function of θ. For each θ we have again conducted the field sweep from 0 to -2 T under sweep rates ranging from 3 to 100 Oes^{-1} at 110 K, obtaining data analogous to that shown in Figure 1.28. From this we have extracted the H_c and plotted it as a function of the sweep rate for the different θ as shown in Figure 1.30. We observe that in general the absolute coercive field decreases as a function of θ possibly indicating that the **L**-vector is along a harder axis compared to when the field is out-of-plane ($\theta = 0$ deg). This agrees with the evolution of the saturation fields in the hysteresis loops measured under different θ shown in Figure 1.17: away from $\theta = 0$ towards 90 deg the saturation field is increasing. Shifting the data allows observing the change in the slope with the changing θ as shown in Figure 1.30 - for a larger θ the change in coercive field with the sweeping rate is smaller than for a smaller θ. This relates partially to the fact that the exponent n in Equation 1.12 depends on the angle between the field and the easy axis [112] and therefore in order to extract the accurate field orientation dependence of the fitting parameters, the dependence of n on θ must be derived.

1.7 Summary and outlook

In this Chapter we have described the novel concept of a collinear, compensated magnetic group with a broken time-reversal symmetry both in the momentum space. The properties of this new group with a staggered spin-splitted band structure are distinctly different from those of both collinear ferromagnets and antiferromagnets, which has warranted the introduction of new terminology: altermagnets, after the alternating spin-splitting. In this Chapter we have introduced a potential candidate for this new group, namely the epitaxial thin films of Mn_5Si_3, which show all the characteristic properties of altermagnetic mate-

rials, including the vanishing net magnetisation and non-vanishing anomalous Hall effect (AHE). Here we have further studied the properties of AHE in these Mn_5Si_3 films by rotating the Néel vector in different crystal planes, which we have realized by systematically altering the external field orientation as well as the current channel orientation. We have observed strongly anisotropic behavior with the Néel vector orientation relative to the underlying crystal structure, which is unlikely to result from the magnetocrystalline anisotropy, weak magnetisation, and/or evolution of the domain structure. Being a characteristic feature of altermagnets, we therefore consider this anisotropic AHE as increasing evidence of the altermagnetism in the epitaxial Mn_5Si_3 films. We have also introduced further measurement techniques, such as minor loop measurements and dynamic coercivity measurements, for studying the Néel vector switching properties of altermagnets.

The results presented in this Chapter have provided plenty of supporting evidence on why the epitaxial thin films of Mn_5Si_3 are a strong candidate for the d-wave altermagnetism. In parallel, we have introduced a wide experimental tool set for indirectly demonstrating altermagnetism in a material where a direct observation of the spin structure is challenging. This opens up new avenues for further studies on the Mn_5Si_3 thin films in terms of their altermagnetic properties.

1.8 Further research directions

- Direct verification of the altermagnetism in the Mn_5Si_3 epitaxial films, which could be realized through angle-resolved photoemission spectroscopy (ARPES) where the spin splitting of the bands in the momentum space could be observed, or through neutron diffraction experiments, where the spin structure in real space could be observed. However, both are experimentally challenging: former due to the requirement for clean and atomically flat surfaces, and latter due to the requirement for sufficient sample volume.

- Further studies on the switching mechanism in the Mn_5Si_3 epitaxial films. This could be realized through continuation of the minor loop studies, where rate-dependent and/or consecutive loop measurements could be fruitful. For understanding how the system couples to the external field, vector magnetometer measurements could provide useful information but access to such a set-up can be challenging. Understanding better the switching mechanism would also aid in the derivation of the fitting function for the dynamic coercivity that has to be specific to altermagnets with magnetocrystalline anisotropy beyond uniaxial. However, this would also require further studies on the magnetocrystalline anisotropy of the Mn_5Si_3 thin films. On the theoretical side, an expression for the switching energy barrier has to be derived where the switching mechanism and the anisotropy are taken into account.

- Further investigations on the altermagnetic properties of the epitaxial Mn_5Si_3 thin

films. Examples include pure spin current generation [50], GMR/TMR effect [44], chiral magnons [51], and superconducting spin-triplet currents [52], which is currently under investigation in the AF spintronics team at SPINTEC in the framework of the post-doctoral fellowship of Dr. Javier Rial and the AMR-DFG consortium. This is based on our earlier work on the propagation of spin-singlet currents in a conventional antiferromagnet [114].

Chapter 2

Dynamic imprinting of nanoscale topological phases into an antiferromagnet [4]

In the previous Chapter we have explored the impact of the global symmetry of a compensated magnet on the topology of its band structure in the momentum space. Here, we continue on the topic of how symmetries play a role in giving rise to unique magnetotransport properties in compensated magnets. However, we will shift the focus from altermagnets to antiferromagnets (AFM) and from the global spin structures to local spin textures. This work was done in the framework of Hubert Curien collaboration with University of York where I had the opportunity of doing several short research stays. The work presented in this Chapter will be reported in an article:

M. Leiviskä, S. Jenkins, R.F.L. Evans, D. Gusakova, and V. Baltz, *'Dynamic imprinting of nanoscale topological phases into an antiferromagnet'*, arXiv:2302.08842.

As we have already established in the previous Chapter, controlling the magnetic order parameter of compensated magnets is highly non-trivial due to the vanishing net magnetisation. This restricts our ability to study topologically protected real-space states of antiferromagnets as the nucleation of such states is challenging. In this Chapter we show how to nucleate predefined, localised spin textures in a thin film antiferromagnet, γ-$IrMn_3$, using atomistic simulation software VAMPIRE. This is illustrated in Figure 2.1. Our method utilises the exchange bias coupling between a ferromagnet (FM) and an antiferromagnet, allowing us to imprint the topological states on the former onto the latter by means of a thermal cycling procedure. We will show that these imprinted antiferromagnetic spin textures are stable against field perturbations. We will also discuss how the various material parameters affect the efficiency of the spin texture imprinting and the characteristics of the imprinted textures. This work paves way for further studies on topologically protected real-space phases in antiferromagnets and can promote the development of denser and faster spintronic devices.

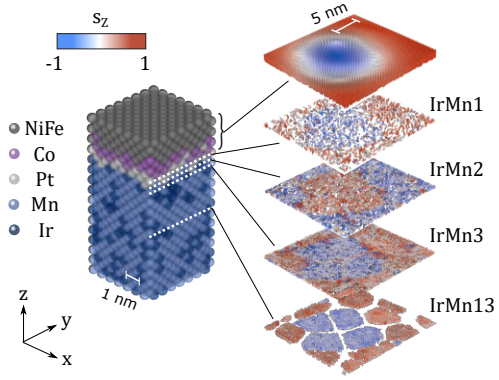

Figure 2.1: The main finding presented in this Chapter: imprinting skyrmion spin textures from a ferromagnetic layer onto and through an antiferromagnetic layer as demonstrated by atomistic simulations. In IrMni, i refers to the ith monolayer away from the Pt/IrMn interface.

2.1 Real-space topological states in magnetic materials

Magnetic materials can host a variety of localised, non-collinear spin textures that cannot be continuously transformed into the uniformly magnetised state, making them remarkably stable. Such states are referred to as topologically protected states and in theory are separated from the topologically trivial uniform state by an infinite energy barrier. In practice, however, these energy barriers are finite due to the discrete lattices, finite-size effects, and finite magnetic anisotropies, but still large enough to make these spin textures robust against deformations and give them particle-like properties. Examples of such topological spin textures include vortices, skyrmions, and hopfions [115][116], of which skyrmions are the main focus of this Chapter. The different topological states can be classified by their winding number (a topological invariant), which for a continuous system is defined as:

$$Q = \frac{1}{4\pi} \int \mathbf{m} \cdot \left(\frac{\partial \mathbf{m}}{\partial x} \times \frac{\partial \mathbf{m}}{\partial y} \right) dx dy, \tag{2.1}$$

where $\mathbf{m}$ is the magnetisation unit vector. The winding number can be understood in terms of how many times the $\mathbf{m}$ vectors cover a sphere when mapped onto one, as illustrated in Figure 2.2a. For a skyrmion, the coverage is exactly once so $Q = \pm 1$ while for a uniformly magnetised state $Q = 0$, which explains the robustness of skyrmions against unwinding into a uniform state in terms of topology. The presence of topologically protected states will influence the physical properties of a magnetic system, making these states of interest for both studies on fundamental physics, such as spin-dependent transport effects, and industrial applications, such as novel spintronic memory and logic devices [117][118].

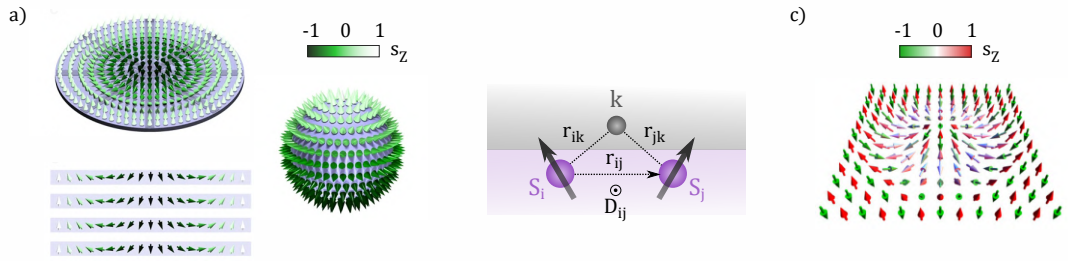

Figure 2.2: (a) A ferromagnetic Néel type skyrmion where the spins rotate from pointing down in the core and to pointing up far away from the center (or vice versa) and the rotation is in the plane perpendicular to the domain wall plane. Mapping the spins onto a surface of a sphere reveals a coverage of exactly once, which corresponds to the winding number 1 of ferromagnetic skyrmions. Figure adapted from Ref. [119]. b) Simple schematics of interfacial DMI-interaction: two spins S_i and S_j couple indirectly via a non-magnetic atom across the interface, favoring a perpendicular alignment of the two spins. In this interfacial case the DMI vector is pointing parallel to the film plane. (c) An antiferromagnetic Néel type skyrmion with the two sublattices each hosting a skyrmion with opposite polarities. Figure obtained from Ref. [120].

2.1.1 Ferromagnetic skyrmions

We will now introduce the main spin texture of interest in this Chapter, the skyrmion. Skyrmions are nanoscale axisymmetric spin textures where the spins gradually rotate from antiparallel orientation (relative to the symmetry axis) at the skyrmion core to a parallel one at the skyrmion perimeter (or vice versa), as shown in Figure 2.2a. The plane and the sense of rotation define the type and chirality of the skyrmion, respectively. In this work, we focus on the Néel type skyrmions where the spins rotate in the plane perpendicular to the domain wall plane as illustrated in Figure 2.2a.

The existence of skyrmions in real magnetic systems requires a lowering of the system symmetry, more specifically the breaking of the inversion symmetry [89][121], which can be realized for example in non-centrosymmetric bulk systems or layered heterostructures. This symmetry-breaking is also at the origin of the antisymmetric exchange interaction [122][123] (Dzyaloshinskii-Moriya interaction or DMI) between neighboring spins at sites i and j:

$$\mathscr{H}_{DMI} = \mathbf{D}_{ij} \cdot (\mathbf{S}_i \times \mathbf{S}_j). \tag{2.2}$$

Here $\mathbf{D}_{ij}$ is the DMI vector, which for the interfacial case can be expressed as $\mathbf{D}_{ij} = D_{ij} \cdot (\mathbf{z} \times \mathbf{r}_{ij})$ [124], where $\mathbf{z}$ is a unit vector perpendicular to the interface and $\mathbf{r}_{ij}$ is the distance vector from site i to j. The microscopic origin of DMI lies in the spin-orbit coupling and therefore a particularly strong DMI interaction can be observed at interfaces between magnetic materials and heavy metals, Co/Pt interface being a good example [125][126][127]. The interfacial DMI interaction is shown schematically in Figure 2.2b.

The presence of skyrmions affects the transport properties of the system through the non-vanishing geometrical phase that is acquired by the conduction electrons when their

spins follow the winding of the local spins [128][129]. This geometrical phase gives rise to a transversal velocity contribution known as the topological Hall effect (THE), where the Hall resistivity is non-linear in magnetisation and introduces additional humps and dips to the Hall signal [129]. However, THE can also originate from other sources like other non-collinear spin textures, such as in bulk Mn_5Si_3 [79], or presence of two AHE components with different magnetotransport properties [87]. Note that in the previous Chapter (Section 1.4.5) we also observed topological-like features in the AHE hysteresis loops in the second magnetic phase of the epitaxial thin films of Mn_5Si_3, but there the origin is more likely either a non-collinear global spin structure or co-existence of two AHE components.

Another notable transport phenomenon relating to skyrmions is the skyrmion Hall effect (SkHE) shown in Figure 2.3a: applying a spin-polarized current to the system will induce a skyrmion motion in curved trajectories due to the gyrotropic force that arises from the chiral topology of the skyrmions [128][130]. This effect is detrimental for the functioning of skyrmion-based spintronic devices where straight trajectories are essential for tractable and durable information retention. Finding solutions to overcome the SkHE is therefore of significant research interest. Possible solutions proposed so far include adjusting the direction along which the current is spin-polarized [131], or coupling two skyrmions of opposite polarity in order to cancel out the topological charge and hence the SkHE. The latter solution can be realized in synthetic antiferromagnets [132][133][134], where two FM layers couple antiferromagnetically through a non-magnetic layer, or in real antiferromagnets where the different magnetic sublattices can host Sks of different polarities. The drawback of the synthetic AFMs (SAF) is that the interlayer coupling is significantly weaker compared to the interatomic coupling, making the SAF Sks more vulnerable to field perturbations. In this work, we focus on Sks in real AFMs.

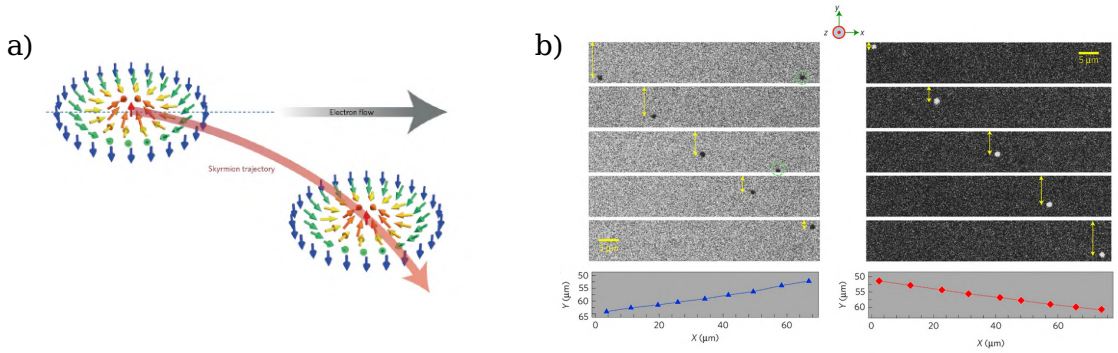

Figure 2.3: a) Illustration of the skyrmion Hall effect where the current-induced motion of skyrmions will not proceed in a straight trajectory due to the gyrotropic force. Figure obtained from Ref. [130] b) Experimental observation of the skyrmion Hall effect utilizing magneto-optic Kerr effect. The chirality of the skyrmion determines the direction in which it is deflected upon current-induced motion (here on the left panel the skyrmion has Q = -1 and on the right panel Q = +1). Figure obtained from Ref. [135].

2.1.2 Antiferromagnetic skyrmions

Antiferromagnetic materials have numerous competitive advantages over their FM counterparts [28][29][136]: they are more robust against external field perturbations, they have faster (THz) dynamics, and they are more abundant, to name a few. Moreover, they can exhibit novel, potentially strong transport properties that allow for efficient control and probing of the order parameter. As antiferromagnets are composed of two or more magnetic sublattices with antiparallel coupling, they allow the formation of intercalated skyrmions of opposite topological charges, as shown in Figure 2.2 for the two-sublattice case. This changes the symmetry of these local spin textures, giving rise to various interesting properties like vanishing net magnetisation and vanishing net winding number, which in turn allow for novel transport phenomena to arise like faster longitudinal skyrmion velocities [137][138], vanishing skHE and THE [137][138], as well as a non-vanishing topological spin Hall effect [139][140].

In general, nucleation of skyrmions requires overcoming the energy barrier created by topological protection. In FMs, this can be realized with an external magnetic field of appropriate strength [141][142], or in a more controlled manner using localised spin-polarized currents [143] or specific device geometries [144]. In AFMs, however, where the order parameter is less sensitive to external fields the nucleation of AFM Sks is more challenging. Possible nucleation techniques include combining a pair of domain walls using spin-polarized current and constricted geometry [137] or ultra-fast laser pulses [145], which both have been demonstrated by micromagnetic simulations. Experimental observations, on the other hand, include a fractional AFM Sk lattice at cryogenic temperatures [146] and AF Sk analogues at room temperature [147]. The challenging nucleation can also be circumvented by using synthetic AFMs [132][133] but as mentioned before, such synthetic AFM Sks are less stable than real AFM Sks. In the remaining of this Chapter we present a universal AFM Sk nucleation method that applies to both metallic and insulating AFMs, doesn't necessitate complex device geometries, cryogenic temperatures, or exotic materials. This opens up perspectives for future systematic research on the fundamental spintronic properties of AFM Sks and other localised spin textures.

2.2 Imprinting topological spin textures from a ferromagnet to an antiferromagnet using exchange bias

Our solution for nucleating topological spin structures in real AFMs relies on FM/AFM heterostructures and the exchange interaction across the FM-AFM interface or what is commonly known as the exchange bias effect [27].

The exchange interaction across an interface between FM and AFM layers gives rise to additional unidirectional anisotropy in these systems. A simplified understanding of the microscopic origin is illustrated in Figure 2.4a. Applying an external field at a tempera-

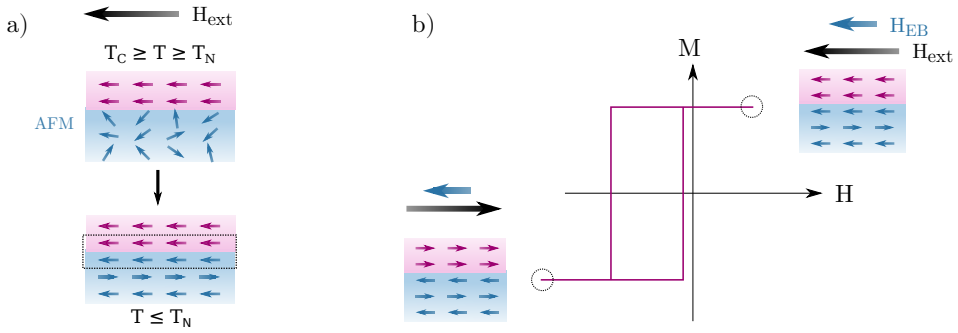

Figure 2.4: (a) Exchange bias originates from the interfacial exchange coupling between FM and AFM layers and can be set by field-cooling the system from above the Néel temperature (T_N) where the AFM is disordered down to below T_N where the AFM orders and the interfacial AFM spins align with those of the FM layer. b) Exchange bias acts like an additional unidirectional anisotropy, making the FM coercivity field direction dependent. This causes a horizontal shift of the hysteresis loop.

ture above the Néel temperature (T_N) of the AFM layer but below the Curie temperature (T_c) of the FM layer will align the FM spins with the field while the AFM spins remain disordered. The system can then be cooled down below T_N and the AFM spins adjacent to the interface will align with the FM spins and the rest of the AFM layer will set accordingly. If the system is then subjected to a field-cycling, the AFM spins being largely insensitive to external fields will provide the FM spins with an energetically favorable direction to align with, which is parallel to the interfacial AFM spins. This behavior is similar to the system containing an additional internal biasing field, hence the term *exchange bias*. A characteristic feature of this unidirectional anisotropy in an exchange biased system is the shifted hysteresis loop of the FM layer (illustrated in Figure 2.4b) - antiparallel orientation between the external and exchange fields will increase the field at which the FM layer is reversed while a parallel orientation will reduce this field compared to a non-biased system. This effect is of technological utility as it allows increasing the stability of the magnetisation direction of the adjacent FMs, allowing for example the pinning of a reference layer in the spin valve-based spintronic devices, as explained in Introduction.

The exact microscopic details of exchange bias depend strongly on the system parameters such as the interface structure, FM and AFM anisotropies, and presence of magnetic domains to name a few [27]. Recently, these details have been unravelled for a specific AFM, namely the γ-$IrMn_3$, using atomistic simulations [148][149]. γ-$IrMn_3$ is an antiferromagnet with an fcc structure where the four unique atomic positions can each host a Mn atom, meaning that there are four magnetic sublattices, as shown in Figure 2.5a. The γ-variation of $IrMn_3$ is atomically disordered meaning that the Ir atoms are equally distributed among the four sublattices so that each contains 25% Ir. However, for a real, finite-sized sample this amount is not exactly 25% but instead there is a small statistical imbalance, which results in one of the sublattices having more Mn atoms than the others

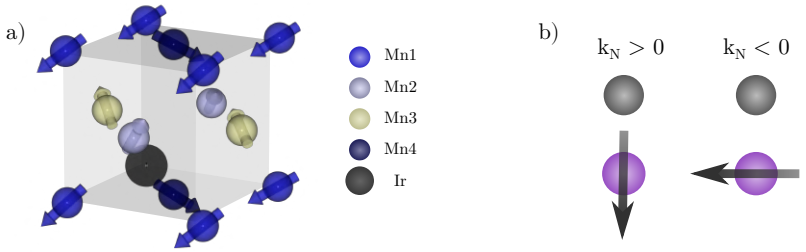

Figure 2.5: The unit cell of $IrMn_3$ containing four magnetic sublattices marked as Mn 1-4. For the γ-variation the Ir atoms fill $\sim 25\%$ of each sublattices. b) Illustration of the effect of the Néel pair anisotropy term in the spin Hamiltonian. A positive Néel pair anisotropy constant (k_N) orients the spin radially to the neighboring atom (gray sphere) while a negative k_N results in a tangential orientation.

[149]. This, in turn, means that there is a small, uncompensated and irreversible magnetic moment that is pointing in the direction of the sublattice with most Mn atoms and this can then couple to the FM layer, giving rise to the exchange bias effect [149].

The interfacial exchange coupling can be used to not only modify the FM magnetisation reversal but also to imprint spin textures from the FM layer onto the adjacent AFM layer. As discussed earlier, the ease of nucleating non-trivial spin textures such as domains, vortices and skyrmions in the FM layer is considerably easier than in the AFM layer, making this imprinting method particularly attractive. Experimentally, the imprinting of a non-uniform spin texture from $Ni_{80}Fe_{20}$ to γ-$IrMn_3$ has been demonstrated indirectly through modification of the FM transport properties [150]. This was soon followed by direct observations (through element-sensitive x-ray magnetic circular dichroism - photoemission electron microscopy (XMCD-PEEM)) of vortex imprinting from $Ni_{80}Fe_{20}$ to γ-$IrMn_3$ [151] and from Fe to NiO and CoO [152]. In the latter case the imprinting was observed to extend beyond the uncompensated interfacial AFM spins through the bulk of the 3 nm thick AFM [152]. More recently, an imprinting of FM skyrmion bubbles from $Ni_{80}Fe_{20}$ to γ-$IrMn_3$ was directly observed using magnetic imagining techniques [153]. These experimental observations are summarized in Figure 2.6.

It should be noted, however, that the spatial resolution of magnetic imaging techniques such as XMCD-PEEM is a few tenth of a nanometer meaning that the microscopic details of the imprinting method cannot be resolved. Furthermore, the penetration depth of the imprinting is challenging to resolve with this experimental tool due to its weighted depth-sensitivity. In order to gain a better understanding on the microscopic mechanism behind the spin texture imprinting method, we employ the atomistic simulation software VAMPIRE [148] in order to create a realistic FM/AFM heterostructure with exchange bias and demonstrate the imprinting of local spin textures from the FM onto the AFM through a thermal cycling procedure. In the later sections of this Chapter we will discuss the atom-

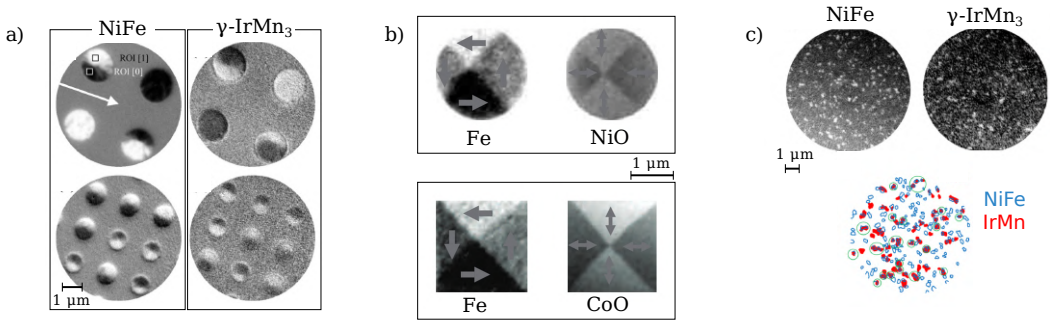

Figure 2.6: Element-specific XMCD-PEEM images showing the magnetic contrast in the different layers of an exchange-biased stack. Different contrasts indicate the orientation of the order parameter relative to the x-ray beam propagation direction and the element specificity is realized through adapting the energy of the x-ray beam. a) Vortex imprinting from NiFe to γ-$IrMn_3$, where the propagation direction of the x-ray beam is denoted with an arrow. Figure adapted from Ref. [151]. b) Vortex imprinting from Fe to NiO and CoO, Figure adapted from Ref. [152]. c) Skyrmion-texture imprinting from NiFe to γ-$IrMn_3$ with a superposition of the texture contours shown below. Figure adapted from Ref. [153].

istic details of the imprinting, including the morphology of the imprinted textures, their penetration depth and stability against field perturbations, as well as the impact of various materials parameters on the imprinting efficiency. Before that, we will introduce the concept of atomistic simulations and introduce the simulation system we have developed.

2.3 Atomistic simulations

Atomistic modelling of magnetic materials considers each magnetic atom as a localised magnetic moment rather than assuming a continuous vector field where the exchange interaction aligns the spins perfectly so that their contribution can be averaged over a finite nanoscale volume, which is the case with micromagnetic simulations. In this work, the atomistic resolution is of key importance because our simulations concern an antiferromagnetic material, intermixed interfaces, and high temperatures, each breaking the assumption of magnetisation being a continuous vector field. For our simulations, we are using an open-source atomistic simulation software VAMPIRE developed by Dr. Richard Evans *et al.* [148]. This software has been successful in modeling the non-trivial magnetic properties of γ-$IrMn_3$ [154] introduced previously in Section 2.2 as well as the microscopic details of exchange bias interaction across a CoFe/γ-IrMn3 interface [149] and is therefore an ideal choice for our simulations.

2.3.1 Spin Hamiltonian

In our simulations the energetics of the system are governed by the spin Hamiltonian $\mathscr{H}$, which includes four main interactions:

$$\mathscr{H} = \mathscr{H}_{exchange} + \mathscr{H}_{DMI} + \mathscr{H}_{Néelpair} + \mathscr{H}_{Zeeman} \tag{2.3}$$

The first term describes the Heisenberg exchange interaction between two spins $\mathbf{S}_i$ and $\mathbf{S}_j$:

$$\mathscr{H}_{exchange} = -\sum_{i<j} J_{ij}\mathbf{S}_i \cdot \mathbf{S}_j \tag{2.4}$$

For a positive exchange constant J_{ij} the spins couple ferromagnetically (parallel) while for a negative J_{ij} the coupling is antiferromagnetic (antiparallel). The J_{ij} can be obtained from *ab initio* calculations or from experimental values using

$$J_{ij} = \frac{3k_{\mathrm{B}}T_c}{\varepsilon z}[148], \tag{2.5}$$

where k_{B} is the Boltzmann constant, T_c is the critical temperature, ε is the spin wave mean-field correction, and z is the number of nearest neighbors. The J_{ij} between the different magnetic elements in our simulation system are given in Table 2.1.

The second term is the DMI interaction that drives the perpendicular alignment of two spins $\mathbf{S}_i$ and $\mathbf{S}_j$ as was illustrated in Figure 2.2b and discussed in Section 2.1.1.

$$\mathscr{H}_{DMI} = -\mathbf{D}_{ij} \cdot (\mathbf{S}_i \times \mathbf{S}_j) \tag{2.6}$$

The DMI vector $\mathbf{D}_{ij}$ is defined as $\mathbf{D}_{ij} = D_{ij} \cdot (\mathbf{r}_{ik} \times \mathbf{r}_{jk})$, where D_{ij} is the DMI strength. The D_{ij} in our simulation stack are given in Table 2.1.

The third term is the Néel pair anisotropy, where k_N is the Néel anisotropy constant and $\mathbf{e}_{ij}$ is a unit vector connecting the sites i and j.

$$\mathscr{H}_{Néelpair} = -\frac{k_{\mathrm{N}}}{2}\sum_{i\neq j}^{z}(\mathbf{S}_i \cdot \mathbf{e}_{ij})^2 \tag{2.7}$$

This term causes the spin $\mathbf{S}_i$ to orient either radially ($k_N > 0$) or tangentially ($k_N < 0$) relative to specific neighbouring atoms on site j as shown in Figure 2.5b, allowing the simulation of interfacial perpendicular anisotropy as well as the magnetocrystalline anisotropy of γ-$IrMn_3$. The k_N in our simulation system are given in Table 2.1. Other forms of magnetocrystalline anisotropy (uniaxial, cubic, etc.) are omitted in our simulations as the ferromagnetic layer is assumed to have a vanishing magnetocrystalline anisotropy in the bulk, and for the modelling of γ-$IrMn_3$ anisotropy additional terms are not necessary.

The final term is the Zeeman term, which aligns the spin $\mathbf{S}_i$ parallel to an external magnetic field $\mathbf{B}_{app}$.

$$\mathscr{H}_{Zeeman} = -\sum_i \mu_s \mathbf{S}_i \cdot \mathbf{B}_{app} \tag{2.8}$$

Here, μ_s is the atomic magnetic moment and it can be obtained again by using *ab initio* calculations or from experimental values using

$$\mu_s = \frac{M_s a^3}{n_{at}}, \tag{2.9}$$

where M_s is the saturation magnetisation, a is the lattice constant, and n_{at} is the number of atoms per unit cell. The μ_s for our simulation system are given in Table 2.1.

2.3.2 Monte Carlo method

In this work, the time-evolution of the simulation system is realized by the Monte Carlo Metropolis algorithm [158]. This algorithm uses random sampling and is the natural choice for simulating the temperature-dependence of a magnetic state as it is fast and efficient in finding the thermodynamic equilibrium state of the system.

The steps in the Monte Carlo Metropolis algorithm are as follows. First, a spin $\mathbf{S}_i$ is picked and given a new random trial orientation $\mathbf{S}_i'$. Then, the energy difference between the trial and the initial state is calculated as $\Delta E = E(\mathbf{S}_i') - E(\mathbf{S}_i)$. If the trial orientation is more energetically favorable than the initial one ($\Delta E < 0$) it is accepted unconditionally as a new orientation of the spin. If, on the other hand, ΔE is positive the move can be

Parameter	$Ni_{80}Fe_{20}$	Co	Pt	Mn
μ_s (μ_B)	1.05	1.72 [148]	–	2.6
α	1	1	–	1
k_N (10^{-22} J/atom)	–	0.025 (Pt)	–	-4.22 (Ir)[155]
Intermixing (%)	2.5	2.5	5	–
Average grain size (nm)	> 100	> 100	> 100	5 [156]

	$Ni_{80}Fe_{20}$	Co	Pt	Mn
NiFe	11 [157]	14	0.14*	0.35 [155]
Co	14	17 [148]	0.14*	0.35 [155]
Pt	0.14*	0.14*	–	–
Mn	0.35 [155]	0.35 [155]	–	-18 (NN) [155] 15 (NNN) [155]

Table 2.1: (Top) Simulation parameters used for each magnetic element that are not varied between the different simulations. (Bottom) Exchange (J_{ij}, in pJ/m) and DMI* coefficients (D, in pJ/m) for the interactions between the different elements in the stack used in our simulations. NN stands for nearest neighbors and NNN for next nearest neighbors. Note that for $Ni_{80}Fe_{20}$ we consider average properties.

accepted or rejected based on the acceptance probability P:

$$P = \exp(\frac{-\Delta E}{k_B T}) \tag{2.10}$$

Ideally, the acceptance rate should be close to 50%, which in VAMPIRE is achieved using an adaptive Gaussian phase-space sampling [158].

2.3.3 Simulation system

In this Subsection the constituents, structure and interactions of the simulation system are discussed. We have designed the system after the experimental FM/AFM heterostructure developed at SPINTEC in which the imprinting of skyrmionic textures from FM onto AFM was recently observed [153]. From substrate up, the complete stack they have used is //Ta(3)/Cu(3)/γ-$IrMn_3$(5)/Pt(0.5) /Co(0.3)/$Ni_{81}Fe_{19}$(0.87)/Al(2 nm), where the layers playing an active role in the imprinting are γ-$IrMn_3$, Pt, Co, and $Ni_{81}Fe_{19}$ (NiFe), which were also implemented in the present simulation system. The size of the entire simulation stack is 100x100x6.67 nm^3 without periodic boundaries (not allowed by the grain structure of the AFM layer) and the thicknesses of the different layers are the same as in the experimental stack. A small fraction of each layer (2.5% of NiFe and Co, 5% of Pt) is intermixed with the layer below.

Here (NiFe) is the primary FM-layer (we will discuss the role of Co later) and implemented as a continuous layer where each NiFe atom shares the same magnetic properties rather than 19% of the atoms having the properties of Fe and 81% of Ni. These magnetic properties are calculated from the macroscopic magnetic properties like the saturation magnetisation ($\sim 8.6 \times 10^5$ A/m) and Curie temperature ($\sim$ 900 K) of NiFe. In the exper-

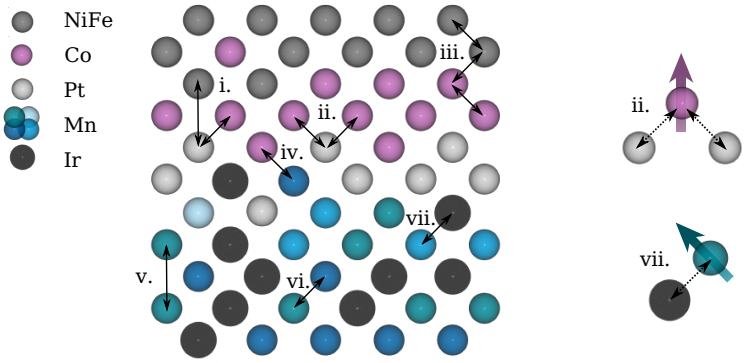

Figure 2.7: The interactions implemented in the simulation system: i. DMI interaction, ii. Néel pair anisotropy, iii-v. FM exchange, vi. AFM exchange, vii. Néel pair anisotropy. These interactions are discussed in more detail in the text. The Néel pair anisotropy causes either radial (ii.) or tangential (vii.) orientation of the spins relative to the neighboring atoms, and is here used to simulate both interfacial PMA (ii.) and magnetocrystalline anisotropy of $IrMn_3$ (vii.)

imental system, the NiFe thickness is such that it is close to the planar-to-perpendicular anisotropy transition so in the simulations we did not implement any magnetocrystalline anisotropy in the NiFe layer. The only interactions implemented within this layer are the FM exchange interactions denoted by iii. in Figure 2.7.

The ultrathin Co/Pt bilayer between the NiFe and γ-$IrMn_3$ serves as a source of both interfacial perpendicular magnetic anisotropy (PMA) [159] and DMI [124], which both promote skyrmion formation in the FM layer. In the simulations, the DMI interaction is implemented between nearest and next nearest NiFe-Pt and Co-Pt neighbors (i. in Figure 2.7), while the PMA is simulated through the Néel pair anisotropy between Co-Pt nearest neighbors (ii. in Figure 2.7). In experiments, this bilayer is thin enough to not decouple the FM and AFM layers magnetically, while in the simulations we don't implement indirect exchange interactions (e.g. RKKY) but the finite intermixing of the interfaces ensures that the FM and AFM spins are still in direct contact and hence coupled. Moreover, the interfacial intermixing is present also in the experimental systems where it enhances the magnetic coupling of the FM and AFM layers.

The AFM layer is composed of grains of γ-$IrMn_3$ with an average size of ~ 4.5 nm and spacing of 0.75 nm, which is well in line with typical experimental values [156]. In VAMPIRE a realistic grain structure is created using a Voronoi construction where the seed points are generated in a hexagonal grid and slightly moved around based on the standard deviation of the grain size distribution [154]. The resulting grain structure and

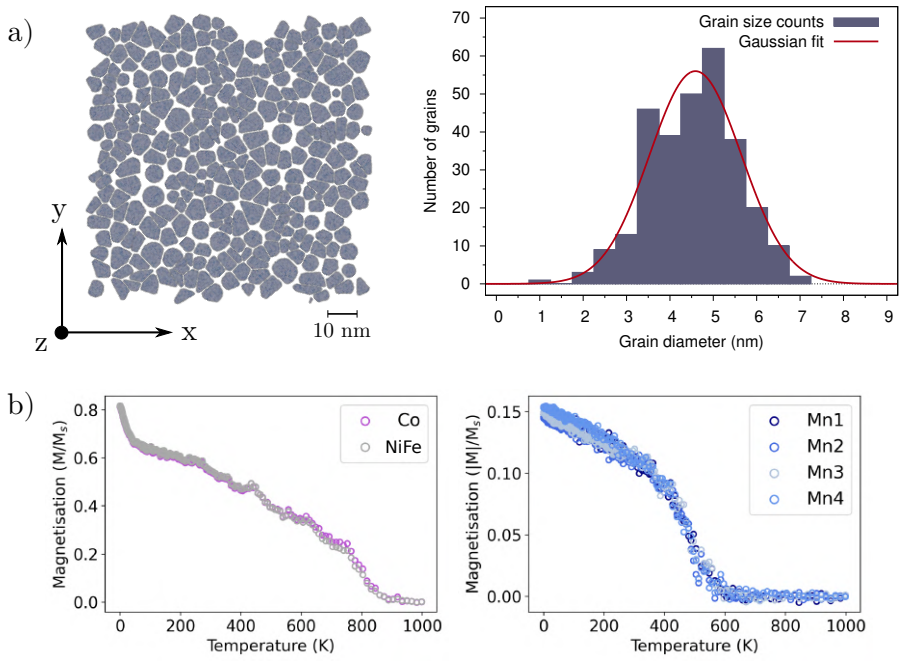

Figure 2.8: (a) The grain structure of the AFM layer created by a Voronoi construction and the distribution of the grain sizes. (b) The critical temperatures of the simulation stack for the different magnetic layers. The Curie temperature of the Co/NiFe hybrid FM layer is ~ 900 K while the Néel temperature of the γ-$IrMn_3$ layer is ~ 550 K. Note that the Mn sublattice magnetisations are plotted separately as the global magnetisation vanishes.

size distribution are shown in Figure 2.8a. It should be noted that in a real polycrystalline heterostructure, both the FM and AFM layers are granular with coincident grains but the FM grains, unlike the AFM grains [160], are magnetically coupled so that the FM layer can be modelled as a single crystal.

The correct tetrahedral 3Q ground state of γ-$IrMn_3$ (shown in Figure 2.5a) is realized by a combination of three important interactions [154] denoted as v-vii in Figure 2.7. The AFM ordering is stabilized by the AFM exchange interaction between the nearest Mn neighbors (different sublattices, vi. in Figure 2.7) and FM exchange interaction between next nearest neighbors (same sublattice, v. in Figure 2.7). Both the AFM and FM exchange coefficients are obtained from *ab initio* calculations [155]. Exchange interactions beyond next nearest neighbors are not considered in order to minimize the computational effort of the simulations. The third and final important interaction in the γ-$IrMn_3$ layer is the Néel pair anisotropy between Mn and Ir spins that forces the Mn spins to point tangentially with respect to the Ir atoms as shown by vii. in Figure 2.7. The physical origin of such behavior relates to the non-magnetic Ir atoms acting like surfaces (missing bonds) and therefore introducing additional anisotropy to the system. The Néel pair anisotropy constant is also obtained from *ab initio* calculations [155].

2.3.4 Critical temperatures of the simulation stack

We have determined the various critical temperatures of the simulation stack by running a field-cooling simulation from 1000 K down to 0 K under an out-of-plane external field of 0.5 T. The (sublattice) magnetisation as a function of temperature is shown in Figure 2.8b for the different magnetic layers Co, NiFe, and IrMn. We found that for both the NiFe and Co layers the Curie temperature is ~ 900 K, which is in agreement with both experimental values (~ 870 K [161]) and the value of exchange constant set in the simulations. We also determined that the Néel temperature of the γ-$IrMn_3$ layer is ~ 550 K, which is in a good agreement with the experimental values for a 5 nm thick γ-$IrMn_3$ [162].

2.4 Atomistic simulations on imprinting spin textures from a ferromagnet to an antiferromagnet

Having established the simulation system, we will move on to discussing the simulation steps that are necessary for demonstrating the imprinting method. The imprinting of spin textures from the FM layer onto the AFM layer is realized through the same thermal cycling procedure that is used for setting an exchange bias in an FM/AFM heterostructure (see Section 2.2). The simulations are carried out in three steps: i) setting the FM layer, ii) setting the AFM layer, and iii) returning the system to remanence. Here, the simulation system has the simulation parameters detailed in Section 2.3.1 in Table 2.1. Note that these parameters describe the main simulation stack and are used to obtain a majority of

the results presented in this Chapter. The control simulations are conducted on stacks with slight deviations to the main stack properties and these changes are explicitly mentioned in the relevant Sections.

2.4.1 Simulation steps leading to the imprinting of localised spin textures

The first simulation step realizes the setting of the FM layer (Figure 2.9i): the system is equilibrated at a temperature below the Curie temperature of the FM layer (here $\sim$ 900 K) but above the Néel temperature of the AFM layer ($\sim$ 510 K). At this temperature the FM layer is magnetically ordered while the AFM layer is completely disordered, ensuring that the imprinting of spin textures will take place from the former to the latter. In our simulations, the first step is carried out at 600 K for 10^6 Monte-Carlo steps. During this step, we also apply an out-of-plane field of $H_z = 0.5$ T in order to nucleate skyrmions in the FM layer instead of maze domains that are stabilized under zero-field conditions, as will be seen later in this Chapter in Section 2.7.2.

The second simulation step brings about the setting of the AFM layer (Figure 2.9ii): we cross the T_N by gradually cooling the system down to 0 K under the same field as before. The bulk of the AFM (exemplified by IrMn 13 in Figure 2.9, where 13 refers to the 13th monolayer away from the Pt/IrMn interface) begins to set around $T = 510$ K, which is well in line with the T_N obtained in the Section 2.3.4. At the interface of

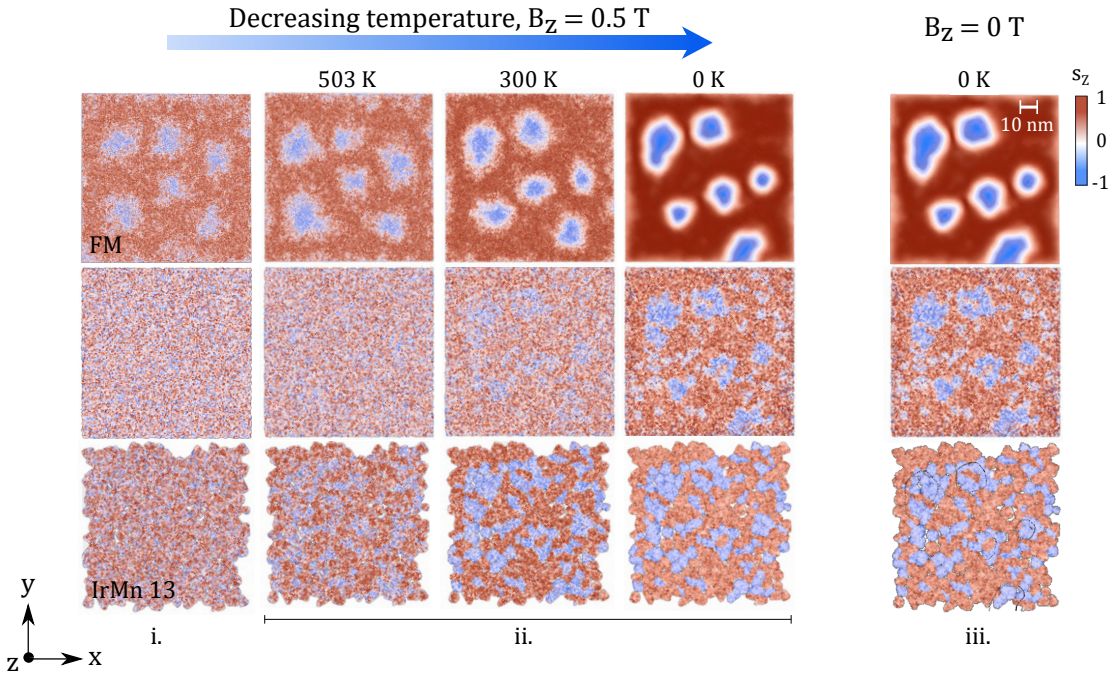

Figure 2.9: The magnetic states of the FM layer, AFM interface (IrMn1), and AFM bulk (IrMn13) during the three simulation steps: i. setting the FM layer, ii. setting the AFM layer, and iii. returning the system to remanence.

the AFM (IrMn 1 in Figure 2.9), however, the spins are still strongly disordered and the presence of any spin textures is difficult to discern. This is likely due to the fact that the uncompensated interfacial AFM spins have two components: a reversible one that is strongly coupled to the FM spins, and an irreversible one that is strongly coupled to the AFM bulk. The thermal fluctuations of the reversible component may be responsible for the increased noise at the AFM interface. At 300 K the orientations of the grains in the AFM bulk are set and their setting has clearly been guided by the FM layer as there is a strong correlation between the spin configurations of the AFM bulk and the FM layer. However, some of the grains have also set independently of the FM layer causing some discrepancies in the imprinting, which will be discussed later. The spin texture imprinting is also visible at the AFM interface, which, while still being more noisy, starts to reveal spin textures that correspond to those of the FM layer. At $T = 0$ K, all the layers are set and the imprinting of the FM spin textures onto the AFM interface and into the AFM bulk is further confirmed: the spin textures observed in the FM are largely reproduced at the interface and in the bulk of the AFM as highlighted by the contours in Figure 2.9. It should be noted that the exact shape of the imprinted textures as well as the final shape of the FM Sks is governed by the grain boundaries of the AFM.

Finally, the last simulation step shown in Figure 2.9iii is the removal of the external field, which causes only minor changes to the spin textures throughout the stack, demonstrating the zero-field stability of the imprinted localised AFM spin textures. In the Section 2.6 we will further demonstrate the robustness of these imprinted AFM textures against field perturbations by showing the effect of field cycling on the spin textures throughout the stack. This insensitivity to the external field allows the isolation of the localised AFM spin textures, which is a prerequisite for well-controlled studies on their properties. Also, note that the imprinting of the spin textures from the FM layer onto the AFM bulk is already realized at 300 K (see Figure 2.9), meaning that the imprinting method in this system does not necessitate cryogenic temperatures.

2.4.2 Discrepancies in the imprinting

As mentioned before, the overall AFM bulk spin configuration is a superposition of imprinted spin textures and some random spin textures that do not correspond to the FM spin configuration. Here we explore various possible origins for these discrepancies. The discrepancies can be divided into two categories based on their location and the extent of deviation: discrepancies exemplified by i. in Figure 2.10a are in the region of uniformly magnetised FM and some of them are accompanied by slight impressions in the adjacent FM layer. Discrepancies exemplified by ii. in Figure 2.10a are inside the imprinted skyrmion-like spin textures and deviate completely from the FM spin configuration.

First possible origin we consider relates to the fact that due to the AFM grains having a distribution of sizes there is also a distribution of T_N - the larger grains have a higher T_N while the opposite is true for the smaller grains. In order to avoid the AFM grains

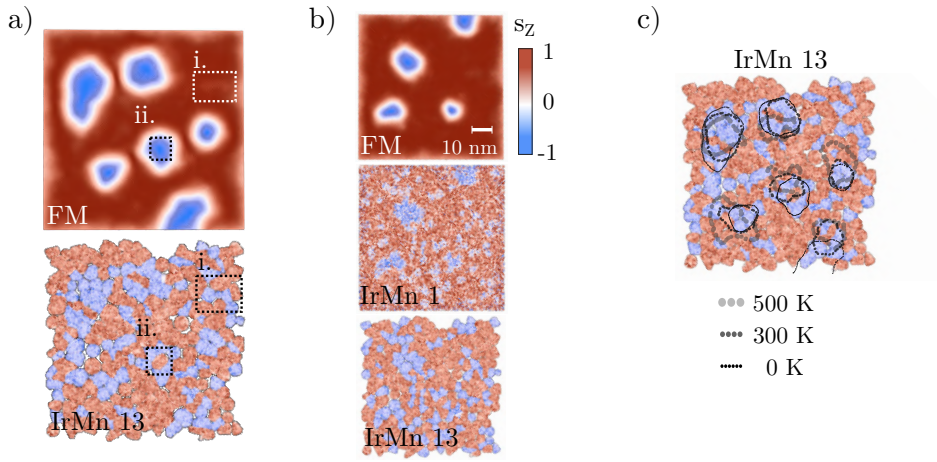

Figure 2.10: a) The two different types of discrepancies in the imprinting of spin textures. Partial discrepancies in the area of uniform FM magnetisation are exemplified by i. while total discrepancies inside the imprinted textures are exemplified by ii. b) The magnetic states in the different layers at 0 K after field-cooling from 700 K. The number of discrepancies is not different to the system shown in Figure 2.9 where the field-cooling starts from a lower temperature of 600 K. c) The trajectory of the FM Sk contours during the field-cooling overlaid with the AFM bulk spin configuration at 0 K.

setting independently from the FM layer we want to ensure that during the first simulation step the temperature is well above the T_N of every AFM grain so that all of them are completely disordered. Therefore, we have repeated the above simulation with the first step being carried out at a higher temperature of 700 K and the field-cooling of the second step running from 700 to 0 K with the intention of seeing if the number of discrepancies is reduced. The third simulation step is unaltered. The results of this simulation are shown in Figure 2.10b where the spin configurations of the different layers after the third simulation step are presented. It is apparent that the discrepancies are still present and their number has not decreased, so we can confirm that at 600 K we are likely above the T_N of even the largest grains and therefore it is a sufficient temperature for the first simulation step.

The second possible origin is that the exchange interaction between the FM and AFM spins is not strong enough to set all the grains. This can be due to either the exchange coefficient being not strong enough or the direct contact between the FM and AFM spins being not frequent enough (i.e. not enough intermixing). This can be verified by additional simulations shown in Figure 2.11: repeating the simulation steps of Section 2.4.1 on a stack with almost three times stronger exchange coefficient ($J_{ij,Mn-NiFe}, J_{ij,Mn-Co}$) relative to the main simulation stack (other properties identical) shows improved conformity between the FM and AFM spin textures and presence of fewer discrepancies. Conversely, a stack where the interfacial exchange interaction is switched off shows no imprinting of the FM spin textures and the AFM grains are set randomly. Similar results can be obtained by changing the degree of intermixing between the Pt and AFM layers as seen in Figure 2.11 - more intermixing brings more FM and AFM atoms in direct contact,

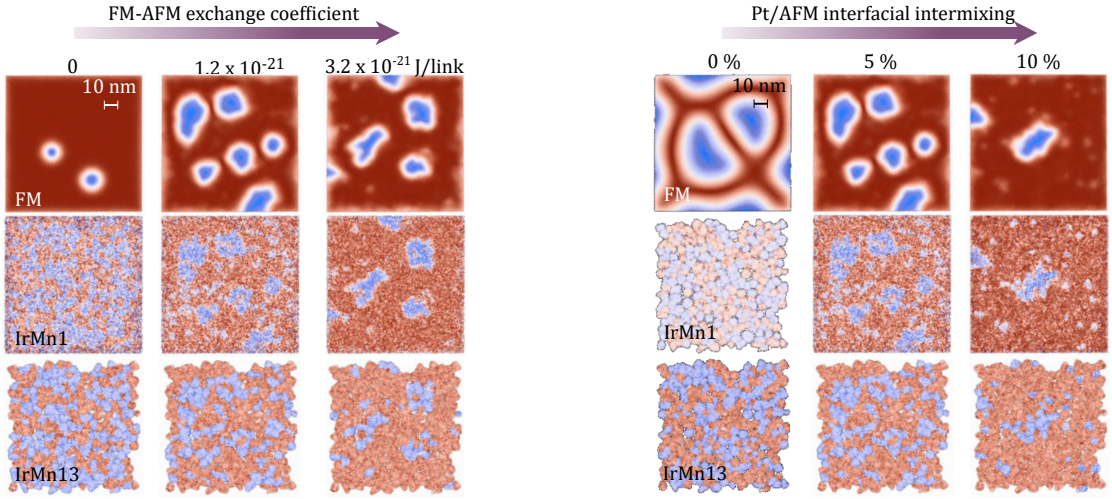

Figure 2.11: The effect of increasing the exchange coefficient strength (left) and the intermixing between the Pt and AFM layers (right) on the imprinting efficiency in terms of FM-AFM spin texture conformity and absence of discrepancies. Increasing the strength and number of exchange interactions between the FM and AFM spins can be seen to improve the imprinting efficiency.

effectively resulting in a stronger exchange interaction between the two layers and as a result, more efficient imprinting. On the other hand, no intermixing removes the direct contact, resulting in the absence of imprinting.

It should be noted that even with stronger interfacial exchange interaction between the FM and AFM layers, neither type of discrepancies is entirely removed. In case of i. type discrepancies, it is also possible that they are residual imprintings of FM Sks that moved or were annihilated during the field-cooling. In Figure 2.10c we see the trajectory of the FM Sks from the start until the end of the field-cooling step showing that they are not static over the course of the field-cooling. The trajectory of the FM Sk at the bottom right shows some additional imprinting that extends beyond the 0 K configuration, while for the FM Sk above it this is not as evident so we can conclude that while this is a possible explanation it doesn't explain all the discrepancies conclusively.

2.5 Microscopic details of the imprinted spin textures

In this Section we take a closer look at the microscopic details of the spin textures after the three simulation steps.

2.5.1 Ferromagnetic layer

First, we take a look at the morphology and the atomistic spin configuration of the FM layer: as shown in Figure 2.12a, FM Sk have radii of $\sim$ 10 to 20 nm and a highly irregular, asymmetric shape. Recalling that the FM layer is intermixed with the AFM layer, the non-circular shape can likely be explained by pinning by the AFM grain boundaries. Indeed,

overlaying the spin structure of the FM layer and the grain structure of the AFM layer, as shown in Figure 2.12b, shows that the two have a relatively good conformity. This explanation is also supported by Figure 2.11 of the previous Section, where increasing the interfacial exchange interaction results in increasingly irregular FM Sks, the shapes of which follow those of the AFM grains.

Taking a closer look at the spin configuration across the selected Sk, shown in Figure 2.12c, reveals characteristics of a Néel type Sk (spins rotate in the plane perpendicular to the domain wall plane). This is as expected based on the interfacial DMI in our system as well as its strength exceeding the critical strength for a Bloch to Néel domain wall transition given by $D_c = 4\mu_0 M_s^2 t \ln 2/2\pi^2$, where μ_0 is the vacuum permeability, M_s is the saturation magnetisation, and t is the film thickness (for our system $D_c = 0.14$ mJ m^{-2}). We extract the domain wall width by fitting the s_x and s_z components in Figure 2.12c using $\cosh^{-1}(\pi[x-x_0]/\Delta)$ and $\tanh(\pi[x-x_0]/\Delta)$ functions, respectively, where x_0 is the location of the domain wall centre and Δ is the domain wall width. For the Sk selected in Figure 2.12a, $\Delta \sim 7.9$ nm, which agrees with the analytical value of $\sim 7-10$ nm calculated using $\Delta = \pi D/4K$ [163], where D is the DMI strength and K is the anisotropy constant. Note that for the sake of simplicity, the analytical value is calculated assuming atomically sharp interfaces, which explains the slight deviation between the analytical and numerical values. Next, we calculate the winding number of an individual FM Sk

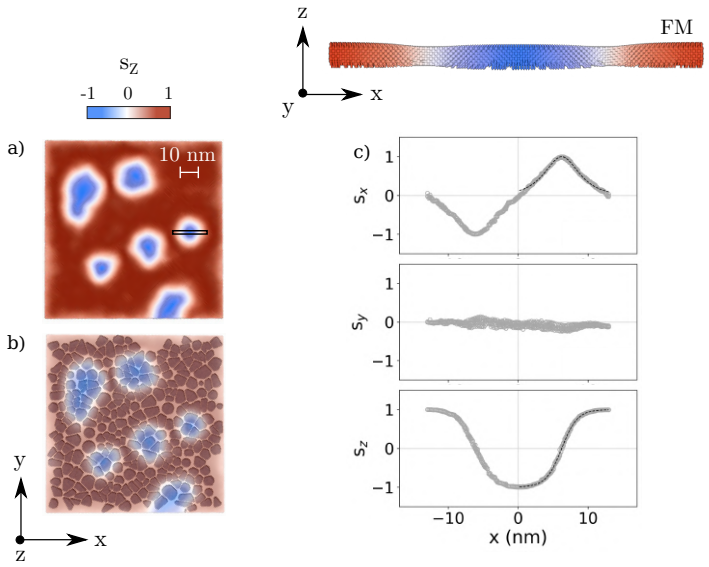

Figure 2.12: (a) Spin structure of the FM layer after the simulation described in Section 2.4.1. The atomistic spin structure of one of the FM Sk bubbles marked with a black rectangle is detailed in (c). b) The FM spin structure overlaid with the grain structure of the AFM layer shows that the former follows the latter relatively closely. c) Lateral dependencies of the spin components s_i in the FM layer across the cross-section marked in (a) showing the characteristic behaviour of a Néel Sk. The s_x and s_z components are fitted with a cosh and tanh functions, respectively, in order to extract the domain wall width.

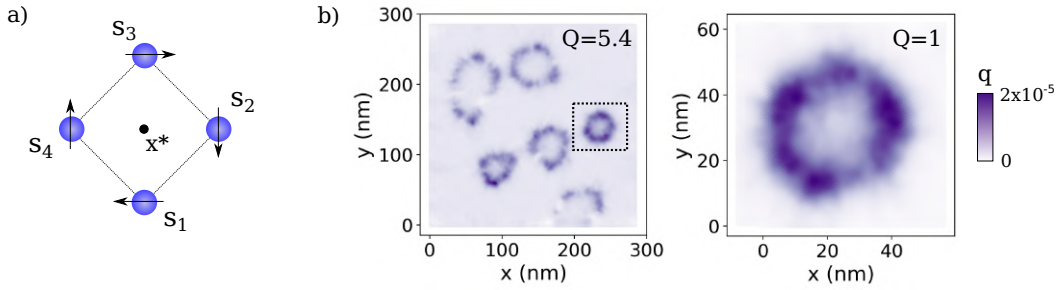

Figure 2.13: a) Illustration of a unit cell cornered by four spins in a square lattice. For each unit cell a topological charge density is calculated. b) Topological charge density q across the entire FM layer. Summing over the q of entire layer yields a topological charge Q of 5.4, which corresponds well to the presence of five entire and one fractional Sk bubbles. c) Topological charge density q across a single FM Sk denoted with a black square in b), yielding a topological charge $Q = 1$, as expected.

and the entire FM layer. The winding number for a continuous system was defined in Equation 2.1, but as we are dealing with a discrete atomic lattice we cannot assume a continuous variation of the magnetisation vector **m**. Instead, we adopt the approach of Berg and Lüscher for calculating a topological charge (i.e. the winding number) for a discrete, two-dimensional lattice [164]. For a square lattice illustrated in Figure 2.13a, we calculate the topological charge density q of each unit cell centered at x^* comprising of four spins $\mathbf{s}_{1-4}$ using:

$$q(x^*) = \frac{1}{4\pi}[\sigma A(s_1, s_2, s_3) + \sigma A(s_1, s_3, s_4)], \tag{2.11}$$

where $\sigma A(s_j, s_k, s_l)$ is the signed area of the triangle delimited by s_j, s_k, and s_l, defined by:

$$\sigma A(s_j, s_k, s_l) = 2\tan^{-1}\left(\frac{\mathbf{s}_j \cdot \mathbf{s}_k \times \mathbf{s}_l}{1 + \mathbf{s}_j \cdot \mathbf{s}_k + \mathbf{s}_j \cdot \mathbf{s}_l + \mathbf{s}_k \cdot \mathbf{s}_l}\right). \tag{2.12}$$

We can then calculate the total topological charge Q of the lattice as $Q = \sum_{x^*} q(x^*)$. As shown in Figure 2.13b, running this calculation for an individual FM skyrmion (note that we have run the calculation for a single monolayer within the FM layer) returns $Q = 1$, as expected, while for the entire FM layer we obtain $Q = 5.4$, which is well in-line with the presence of five entire skyrmions and a fraction of a sixth one. Moreover, the area outside the Sks is not perfectly uniform but contains some inhomogeneities, which also contributes to the winding number.

2.5.2 Antiferromagnetic layer

Next, we move on to the morphology and the atomistic spin configuration of the AFM layer shown in Figure 2.14. Due to the imprinting the average behavior of the spins in the topmost intermixed monolayer of IrMn follows that of the FM spins as seen quali-

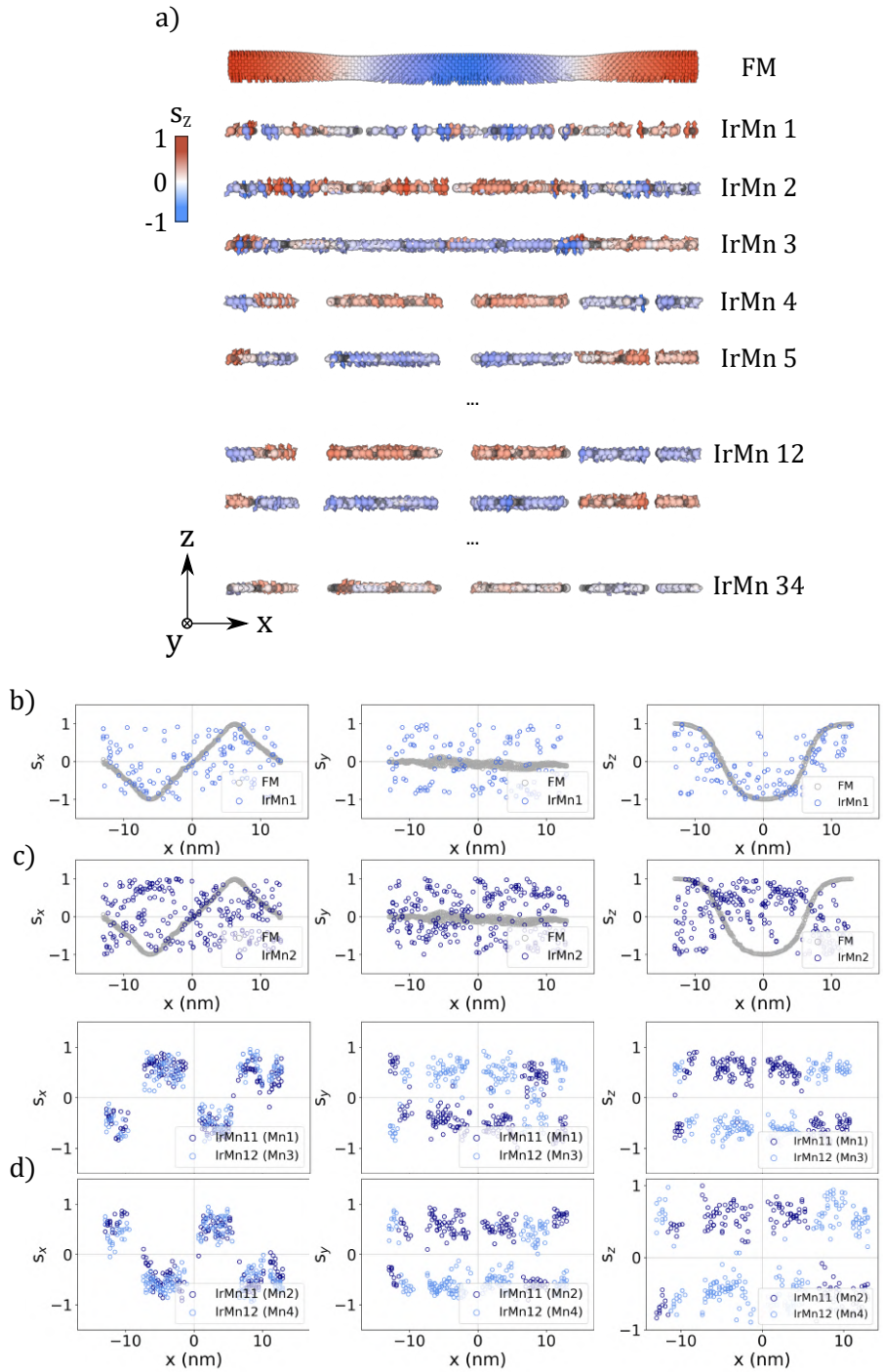

Figure 2.14: a) Layer-by-layer propagation of the imprinting of the Néel Sk from the FM layer into and through the AFM layer. The location of the cross-section is indicated in Figure 2.12a. Alternating AFM layers have an alternating polarity of the spin direction, which is well in line with its expected tetrahedral ground state with 3Q symmetry. b) Lateral dependencies of the spin components s_i in selected AFM monolayers, both at the interface (IrMn1,2) and in the bulk (IrMn11,12). The good correlation between the s_z of the FM and the IrMn layers shows quantitative support for the imprinting of the predefined, localised spin texture.

tatively in Figure 2.14a and more quantitatively in Figure 2.14b. The same is observed for the second topmost, still intermixed, monolayer in Figure 2.14c but with the polarity reversed, which is in line with the AFM ordering of γ-$IrMn_3$ [165] having a tetrahedral 3Q symmetry (recall Figure 2.5). From there the imprinted spin texture propagates further into the bulk of the AFM, as is exemplified by the spin configuration of IrMn4 and IrMn5 in Figure 2.14d: the s_z component of the AFM layers shows a good agreement with that of the FM layer although the domain walls are narrower and more abrupt as they are governed by the grain boundaries. In our system, the imprinting propagates from the interface all the way down to the bottom of the stack, giving a penetration depth of ~ 5 nm for the imprinting, which is well in line with experimental reports on vortice imprinting in CoO and NiO [152] and exchange springs in γ-$IrMn_3$ [166]. The noise (i.e. deviation from FM spin orientation) in the AFM spin orientations is expected and results mainly from the fact that the AFM spins have to abide by the magnetocrystalline anisotropy that drives the tetrahedral 3Q symmetry of the spins. This, for example, prevents the AFM spins from orienting along the film normal while in the FM layer with no anisotropy there is no such restriction. It should be noted that the intermixed interfacial AFM spins have more flexibility due to the reversible component that is coupled to the FM layer [27] but on the other hand the intermixing is introducing more randomness to the system so that overall the noise is not significantly reduced.

2.6 The external field stability of the imprinted spin textures

Next, we study the stability of the imprinted textures against field perturbations by applying an external field to the system. The field is oriented along the film normal and its magnitude is swept from +4 to -4 back to +4 T. Note that the fields are an order of magnitude larger than the typical experimental fields due to the fact that the measurement times accessible to simulations are significantly shorter than those accessible in typical experiments. Here, the sweeping rate is $\sim 7 \times 10^{-3}$ T ns^{-1} while in experiments a typical sweeping rate is $\sim 10^{-11}$ T ns^{-1}. The hysteresis loop resulting from the field-cycling is shown in Figure 2.15a and as expected, it exhibits a shift of ~ -0.7 T towards negative fields due to the exchange bias. As shown in Figure 2.15b-m, the evolution of the spin texture varies from layer to layer. The FM layer (Figure 2.15b-e) follows the field, nearly saturating at strong fields and gradually reversing at intermediate fields by the expansion of Sk bubbles. The AFM bulk (j-m), on the other hand, remains unchanged throughout the field cycle and this can also be seen in the fact that at remanence, the FM layer (Figure 2.15c,e) adopts a configuration that conforms with that of the AFM bulk. The AFM interface, in turn, comprises of a reversible component that follows the FM and an irreversible component that abides by the AFM bulk, and therefore shows a behaviour that is a mixture of the two (Figure 2.15f-l).

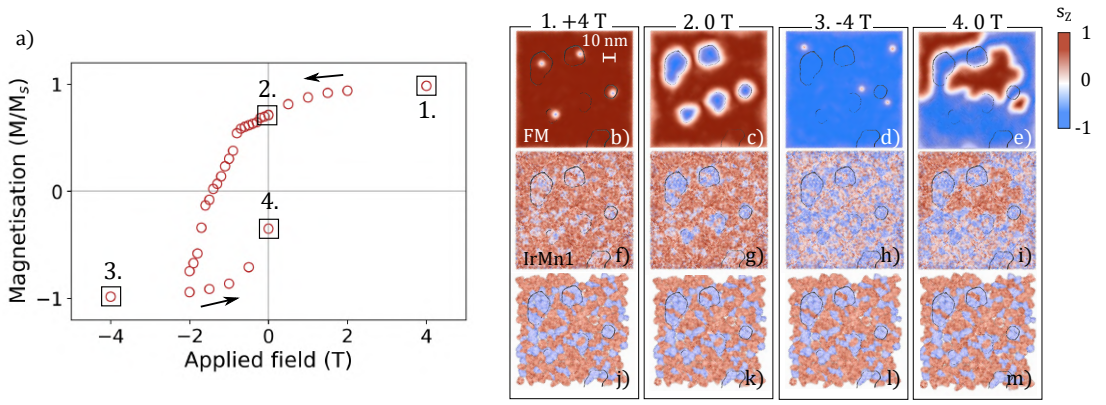

Figure 2.15: a) Field-dependence of the FM magnetisation, normalized (M/Ms), at 0 K and (b-m) snapshots of the evolution of the spin structures during the field-sweep, in the FM (b), interfacial AFM (IrMn1, f-l) and bulk AFM (IrMn13, j-m). The snapshots are taken at positive saturation (1.), forward remanence (2.), negative saturation (3.) and backward remanence (4.). The contours of the FM Sks in Figure 2.12a serve as visual guides.

Overall, this field-cycle shows that the imprinted local spin textures remain unaltered in the AFM bulk and partially at the interface even after the original Sks in the FM layer are annihilated. This means that we are able to transform a system with Sks in the FM layer and no spin textures in the AFM to a system (recall Figure 2.9i) with no Sk in the FM layer but pre-defined spin textures in the AFM layer using consecutive thermal and field cycling processes. It is important to note that the condition for the field stability of the imprinted spin textures is roughly given by $K_{AFM}t_{AFM} \gg J_{int}$, where K is the anisotropy constant, t is the thickness, and J_{int} is the interfacial exchange coefficient. Violation of this relation means that the AFM is no longer insensitive against the field and therefore the AFM spins will rotate along with the FM spins [27]. Here, the relation holds (1.7×10^{-11} $\mathrm{Jm}^{-1} \gg 3.5 \times 10^{-12}$ Jm^{-1}), but if J_{int} is increased significantly in order to improve the imprinting efficiency, it will complicate the ability to obtain isolated AFM spin textures through field-cycling. This, in effect, would complicate studying the isolated properties of these AFM spin textures decoupled from the properties of the FM skyrmions.

2.7 The impact of various simulation parameters on imprinting efficiency and morphology

We will now move on to showing additional simulations where we have slightly changed the simulation parameters or conditions. We will discuss how they influence the efficiency of the spin texture imprinting as well as the morphology of the imprinted textures.

2.7.1 Control simulation without interfacial exchange interaction

First, we show a control simulation on a system with no exchange interaction between the FM and AFM layers at the interface (same properties as the main simulation stack but $J_{ij,Mn-NiFe}$ and $J_{ij,Mn-Co}$ are set to zero). For this system we do not expect any imprinting to take place but instead the spin structures of the FM and AFM layers should evolve independently of each other during the field-cooling step. All other simulation parameters are identical to those of the system described before.

The magnetic states of the FM layer, AFM interface and AFM bulk after the three simulation steps described in Section 2.4.1 are shown in Figure 2.16a: the FM layer contains two SK bubbles while both the AFM interface and bulk show a random domain structure where the grains have set independently of the FM layer. As expected, we do not observe imprinting of the Sk bubbles into the AFM (see Figure 2.16b) and moreover, the FM Sks are smaller and more symmetric compared to those of the system with non-zero interfacial exchange interaction. Recall that the latter observation is due to the fact that removing the interfacial exchange allows the FM Sks to evolve independently of the AFM grain structure. Given the small and symmetric Sk shapes here, coupling to the AFM grains structure evidently stabilizes larger and more irregular Sks. This is also verified by an additional simulation where the average grain size of the AFM layer is increased to 8 nm and the interfacial exchange interaction is turned back on: as shown in Figure 2.16c, here the Sk sizes in the FM layer are significantly larger and the shapes more irregular as dictated by the underying grain structure.

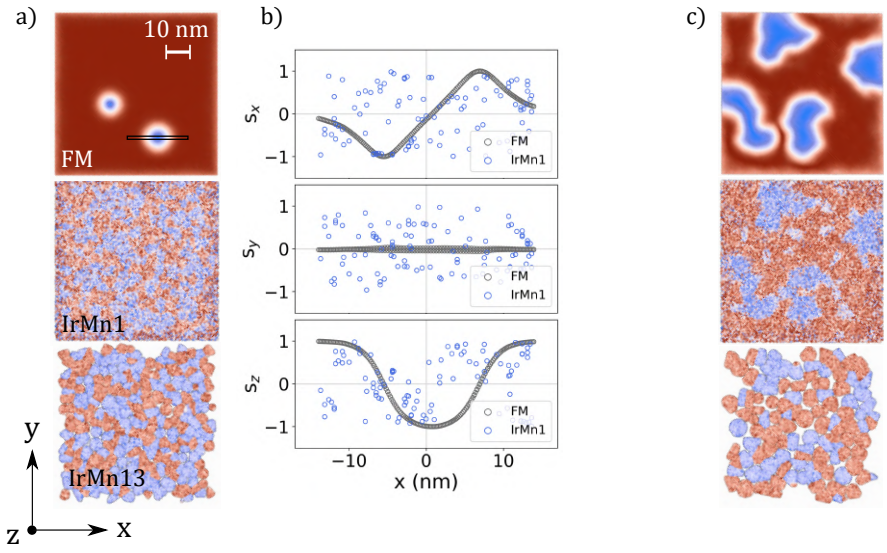

Figure 2.16: a) The magnetic state of the different layers of the simulation stack: FM, AFM interface (IrMn1) and AFM bulk (IrMn13). No imprinting is observed and the FM Sk shape is independent of the AFM grain structure. b) The lack of imprinting is further evidenced by the observation that the AFM spin components s_i show no correspondence to those of the FM layer. c) Increasing the average grain size of the AFM layer stabilizes larger and more irregular Sks in the FM layer.

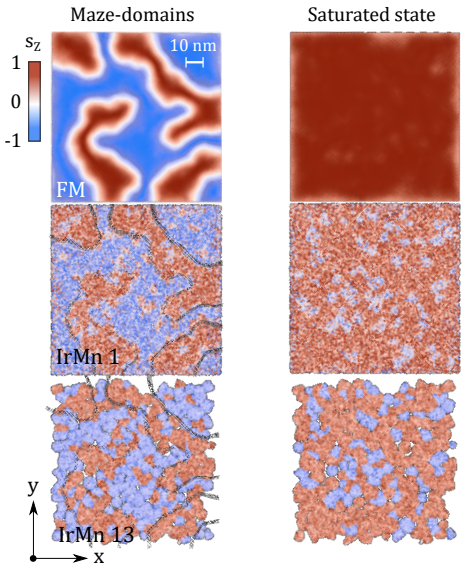

Figure 2.17: Imprinting of different magnetic states of the FM layer onto the AFM interface (IrMn1) and AFM bulk (IrMn13). Maze domains can be nucleated in the FM layer through zero-field cooling, while the saturated state can be realized through field-cooling with a 5 T out-of-plane field. Both states of the FM layer are successfully imprinted on the AFM layer where the grain structure governs the exact morphology of the textures. Some discrepancies are also oberved as discussed in the text.

2.7.2 Imprinting topological states beyond skyrmions

Here, we show that by changing the external field strength during the first and second simulation steps (setting FM and field-cooling, respectively) we can stabilize different spin configurations in the FM layer and consequently imprint them onto the AFM layer as shown in Figure 2.17. For example, when we initialize the system under zero-field we are able to nucleate maze domains in the FM layer and then the subsequent cooling down still under zero-field allows us to realize imprinting of these maze domains onto the AFM layer. Similarly, when the field strength during the initialization and cooling down is increased ten-fold, we nucleate and imprint a saturated magnetic state. As was the case with the FM Sks in Section 2.4.1, the imprinting takes place again throughout the AFM layer and the AFM bulk spin configuration is a superposition of the imprinted and random spin textures (discrepancies). Also, the exact morphology of the imprinted textures is again governed by the AFM grain boundaries, as we have already observed before. Note that here the other simulation parameters correspond to those of the main simulation stack described in Section 2.4.1. Overall, these additional simulations show that our method is not specific to FM Sks but instead shows universal imprinting ability across different real-space spin textures.

2.8 Summary and Outlook

In this Chapter we have introduced a universal and experimentally viable method for nucleating pre-defined, localised spin textures in real antiferromagnets. This method requires a heterostructure comprising of ferromagnetic and antiferromagnetic layers with a strong exchange interaction across the interface, and a thermal cycling procedure. Here, for the antiferromagnet we have used γ-$IrMn_3$ with a Néel temperature above 500 K, meaning that the imprinted spin textures are stable at room temperature. The depth of imprinting is shown to reach at least 5 nm, which is through the entire antiferromagnetic layer in our simulations. We have shown that the efficiency of the imprinting strongly depends on the strength of the exchange interaction across the interface, while the morphology of the imprinted as well as the original spin textures is governed by the grain structure of the antiferromagnetic layer. The original spin textures in the ferromagnet and the imprinted spin textures in the antiferromagnet can be decoupled by a field-cycling procedure, which allows for studies on the isolated antiferromagnetic spin textures. Finally, we have demonstrated the robustness and universality of this imprinting method by varying the original ferromagnetic spin textures from skyrmion bubbles to maze domains to saturated states, and observing that the outcome of the imprinting does not depend on the type of spin texture.

Having established a simulation system in which spin texture imprinting takes place successfully and that corresponds to a realistic experimental system, this work opens up various possibilities for follow-up simulations, a few of which are listed below. The interest is especially on devising further guidelines in terms of material properties on how to realize well-defined and isolated topological spin textures in antiferromagnets experimentally, because this would pave the way for further studies on real-space topology in antiferromagnets. This is an attractive research direction due to not only the industrially favorable properties of antiferromagnets [29][28][136] and their spin textures but also the novel fundamental phenomena that can arise due to the lowering of symmetry in these multisublattice systems [36][167]. In terms of spintronic applications, our results can also aid in the development of denser and faster spintronic devices, as localised spin textures in antiferromagnets are predicted to be small, stable, and fast information carries with straight trajectories of motion. However, the general challenge with using antiferromagnetic materials in spintronic devices is the reading of their magnetic states and therefore further fundamental research on the transport properties of these states, such as the topological spin Hall effect, is of significant importance.

2.9 Further research directions

- Finding the optimal conditions for efficient imprinting (minimum amount of discrepancies between the original and imprinted spin textures) and isolation of the

antiferromagnetic spin textures. We have shown in this Chapter that making the interfacial exchange interaction stronger generally improves the imprinting efficiency, but as was discussed in Section 2.6, the field-stability of the imprinted textures suffers when the interfacial exchange interaction is stronger, thereby complicating the decoupling of the ferromagnetic and antiferromagnetic spin textures. The relevant parameters to optimise here are for example the layer intermixing, thickness of the antiferromagnetic layer, and/or structure of the antiferromagnetic layer (granular vs. single crystal), which are all experimentally accessible parameters, too.

- Exploring imprinting onto different antiferromagnets. Here we have opted for γ-$IrMn_3$ with four magnetic sublattices and a strong crystalline anisotropy, which restricts the winding of the spins and in effect, might hinder the nucleation of topological antiferromagnetic states with a well-defined topological number. However, the spins of softer antiferromagnets are more susceptible to the dragging by the ferromagnetic layer during the field-cycling, meaning that again a careful optimisation of the material choice is necessary. It could also be interesting to extend this study to altermagnetic materials (discussed in detail in Chapter 1) as the impact of real-space topological structures on their transport properties could offer novel solutions to detecting these structures, while retaining the vanishing net magnetisation and topological charge.

- Studying the current-induced dynamics of the coupled and decoupled original and imprinted spin textures, especially skyrmions. Interesting research questions relate to for example the velocity and trajectory of the spin textures, and the presence or absence of the skyrmion Hall effect. Previous reports on skyrmions in self-standing antiferromagnets predict straight skyrmion trajectories with high longitudinal and vanishing transversal velocities [138][137], so it is interesting to study whether the adjacent ferromagnetic layer has any influence on these properties.

These research directions will be pursued in the AF spintronics team at SPINTEC in collaboration with the University of York in the framework of the PhD thesis of C. Thevenard, starting in October 2023.

Chapter 3

Spin fluctuations as a probe of unconventional magnetic phases and phase transitions

In this final Chapter we shift the focus from the direct discussion of spintronic properties specific to compensated magnetic structures and textures to describing a powerful experimental tool for probing spin transport properties in a variety of materials. This tool is the ferromagnetic resonance (FMR) induced spin pumping and we will illustrate its functionality by considering a specific example of studying linear and non-linear spin susceptibilities around magnetic phase transitions. To this end, in this Chapter we focus on the relativistic mechanisms of pure spin-current generation through FMR-induced spin pumping but we will finish by discussing how the spin-split band structure of altermagnets provides a unique platform for a non-relativistic pure spin-current generation [50]. The material of interest here is PdNi in thin film form and we will show that it shows complex magnetic behavior akin to that of spin/cluster glasses. This means that here we will turn our attention slightly away from compensated magnets but since this tool and the type of study are relevant for any magnetic materials, this Chapter can be viewed as a blueprint for future studies on analogous spintronic properties of antiferromagents and altermagnets. Thus, the main purpose of this Chapter is to highlight and optimize our set-ups ability to probe spin fluctuations through both magnetisation dynamics and spin-to-charge conversion, and since many of the results are preliminary, to serve as a foundation for future research efforts in this specific topic and material as well as other materials.

This work has been conducted in collaboration with the team of Dr. Serge Gambarelli (SYMMES laboratory), for assistance with the set-up used in this Chapter. Moreover, this work has resulted in an ongoing collaboration with the group of Prof. Yasuhiro Niimi at the University of Osaka and in this framework I also had an opportunity to do a short research visit at their facilities.

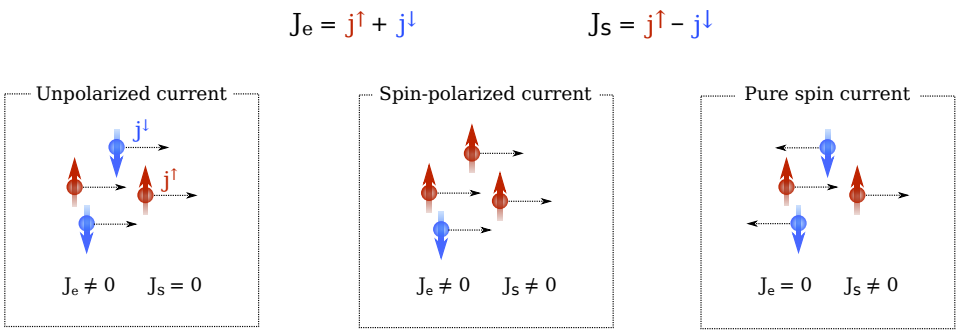

Figure 3.1: Electrons possess both a charge and a spin so that the movement of electrons can give rise to different types of currents depending on the net charge and spin flow during this motion.

3.1 Pure spin current generation through spin pumping

Electrons possess not only charge but also an angular momentum, which is referred to as a spin. Therefore a flow of electrons does not only give rise to a charge current but can also involve a net flow of angular momentum referred to as a spin current. The different types of currents that an electron flow can induce are summarized in Figure 3.1: in unpolarized current there is only a net flow of charge, in pure spin current there is only a net flow of spin, and spin-polarized current involves a net flow of both charge and spin. The advantage of using pure spin current over spin-polarized current in spintronic devices is founded on it having an improved efficiency of angular momentum transport as well as the diminished Joule heating. Moreover, as the angular momentum is also at the root of magnetism, interactions between pure spin current and magnetisation can harness spin current as a probe of the magnetic ordering, which is the research avenue pursued in this Chapter.

One way of generating a pure spin current is through ferromagnetic resonance (FMR) induced spin pumping in multilayered heterostructures comprising of a spin injector (SI) layer and a spin sink (SS) layer, where the former is typically a ferromagnet and the latter is a material that allows for an efficient spin-to-charge conversion. In the following sections we will first discuss the operational principles of FMR, then we will explain how the FMR can induce spin pumping that generates a pure spin current, and finally, how the spin current can be detected upon conversion to a charge current.

3.1.1 Magnetisation dynamics at the ferromagnetic resonance

In ferromagnetic resonance (FMR) experiments, the magnetisation dynamics are driven by externally applied microwaves, which continuously transfer angular momentum to the magnetisation, causing a steady magnetisation precession around an externally applied static magnetic field. The dynamics of this precession are given by the Landau-Lifshitz-

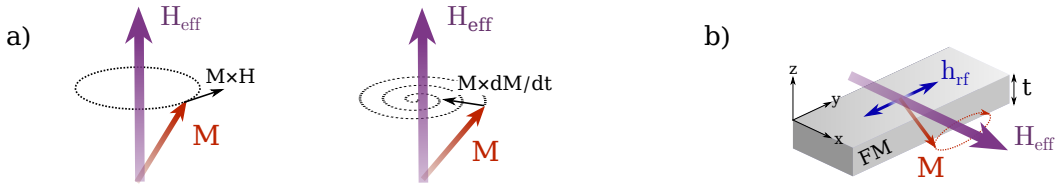

Figure 3.2: a) The two terms of the LLG-equation, one driving precession around an effective field H_{eff} and the other describing the damping of the precession so that the magnetisation M tends to align with the H_{eff}. b) A typical thin film system in FMR experiments where magnetisation precession around a static H_{eff} in the plane of the film is driven by a perpendicular rf magnetic field (h_{rf}), also in the plane of the film.

Gilbert (LLG) equation:

$$\frac{d\mathbf{M}}{dt} = -|\gamma|\mathbf{M} \times \mu_0 \mathbf{H}_{eff} + \frac{\alpha}{M_s}\mathbf{M} \times \frac{d\mathbf{M}}{dt}, \tag{3.1}$$

where the first term describes the magnetisation **M** precession around the effective field H_{eff} (includes the external and anisotropy fields) and the second term describes the damping of this precession, which drives the alignment of **M** with H_{eff}. Both terms are illustrated in Figure 3.2a. The other terms in Equation 3.1 are the gyromagnetic ratio γ, the Gilbert damping constant α, and the saturation magnetisation M_s. The amplitude of the **M** precession is maximum when the frequency of the applied microwave field equals to the resonance frequency (f_{res}) of the system, which is governed by factors such as the anisotropy of the sample and the strength of the applied field, as will be shown below.

Resonance condition

An expression for the resonance frequency can be obtained by solving the LLG equation for a ferromagnetic thin film with a thickness significantly smaller than the lateral dimensions, where **M** is aligned with a static field that is applied in the plane of the sample, and an rf-field applied perpendicular to the static field direction, as illustrated in Figure 3.2b. We assume that during the precession, **M** gains a small component along y- and z-axes (m_y and m_z, respectively) while along x-axis the magnetisation is virtually the same as in the equilibrium position (saturation magnetisation M_s) so that we can express **M** as:

$$\mathbf{M} = M_s\hat{\mathbf{x}} + m_y\hat{\mathbf{y}} + m_z\hat{\mathbf{z}} \tag{3.2}$$

The expression for the effective field is obtained by considering the contributions from the uniaxial anisotropy, demagnetizing field (recall that the demagnetising factors for a thin film are $N_x, N_y = 0$ and $N_z = 1$), applied static field, and the rf-magnetic field (h_{rf}):

$$\mathbf{H}_{eff} = (H_{ext} + H_{uni})\hat{\mathbf{x}} + h_{rf}\hat{\mathbf{y}} + \frac{M_{eff}}{M_s}m_z\hat{\mathbf{z}}, \tag{3.3}$$

where $H_{uni} = 2K_u/\mu_0 M_s$, $M_{eff} = M_s - 2K_u/\mu_0 M_s t$, K_u is the uniaxial anisotropy constant, and t is the film thickness. Substituting these equations in the LLG-equation (Equation 3.1) allows us to find an expression for the susceptibility in the same direction in which the rf-field is applied (we are interested in the absorption of the rf-power):

$$\chi_{yy} = \chi'_{yy} + i\chi''_{yy} = \frac{m_y}{h_{rf}} = M_s \frac{(A + \frac{i\alpha\omega}{\gamma})\left[AB - \frac{i\alpha\omega}{\gamma}(A+B) - \frac{\omega^2}{\gamma^2}(\alpha^2+1)\right]}{\left[AB - \frac{\omega^2}{\gamma^2}(\alpha^2+1)\right]^2 + \left[\alpha\frac{\omega}{\gamma}(A+B)\right]^2}, \tag{3.4}$$

where $A = M_{eff} + H_{ext} + H_u$ and $B = H_{ext} + H_u$.

The resonance condition can be obtained by considering that at resonance m_y is at maximum, which can be realized when the denominator of Equation 3.4 is minimum:

$$\left(\frac{\omega_{res}}{\gamma}\right)^2 = (M_{eff} + H_{ext} + H_u)(H_{ext} + H_u) \tag{3.5}$$

Assuming that $\alpha^2 \ll 1$, the real (dispersive) and imaginary (absorptive) parts of the susceptibility at resonance become

$$\chi'_{yy} = M_s \frac{A(\frac{\omega_{res}^2}{\gamma^2} - \frac{\omega^2}{\gamma^2})}{\left[\frac{\omega_{res}^2}{\gamma^2} - \frac{\omega^2}{\gamma^2}\right]^2 + \left[\alpha\frac{\omega}{\gamma}(A+B)\right]^2}, \tag{3.6}$$

and

$$\chi''_{yy} = M_s \frac{-\frac{\alpha\omega}{\gamma}\left(A^2 + \frac{\omega^2}{\gamma^2}\right)}{\left[\frac{\omega_{res}^2}{\gamma^2} - \frac{\omega^2}{\gamma^2}\right]^2 + \left[\alpha\frac{\omega}{\gamma}(A+B)\right]^2}, \tag{3.7}$$

respectively. At resonance, the $\chi'_{yy} = 0$ while χ''_{yy} is at maximum and a typical FMR spectrum will be shown later in Section 3.2, where the experimental set-up is discussed in more detail.

Intrinsic and extrinsic relaxation mechanisms

The angular momentum of the precessing magnetisation can be dissipated via various internal and external channels, which are all contained by the damping coefficient α in Equation 3.1. The intrinsic damping mechanisms include magnon-electron interactions, magnon-phonon interactions, and eddy currents in the SI layer, of which the second and the last are expected to be negligible in our system. The extrinsic channels include two-magnon scattering, magnetic inhomogeneities, eddy currents in the adjacent layers, and slow relaxation. These channels and their relevance to our system have been extensively discussed in the PhD thesis of Dr. Lamprini Frangou [168]. In this work, however, we are interested in the spin-to-charge conversion in the SS-layer and therefore less concerned in disentangling the different contributions to the magnetisation damping and more concerned on the spin injection efficiency, which depends on the global damping.

3.1.2 Pure spin current generation through spin pumping

Spin-pumping is an extrinsic and non-local channel for dissipating the angular momentum. In essence, in spin pumping magnetisation dynamics drive a spin-current generation [169], making it an inverse of the spin transfer torque effect where a spin-current drives magnetisation dynamics [12]. Typical spin pumping samples have two layers: spin injector (SI, typically a ferromagnet) and spin sink (SS, typically a normal metal). At the interface of the two layers, spin accumulation is naturally generated due to the mismatch in the chemical potentials of the two layers. As illustrated in Figure 3.3a, in the ferromagnetic SI layer the chemical potentials for the spin up and spin down electrons differ, while in the normal metal SS layer they are equal meaning that the average chemical potential across the interface will be discontinuous. This mismatch results in the majority spins diffusing from the SI into the SS layer, where they will propagate until the equilibrium condition is restored due to the spin-flip scattering events. This propagation distance is referred to as the spin diffusion length. Therefore, even for a static magnetisation a chemical imbalance at the interface is generated. For an oscillating magnetisation, where the instantaneous flipping of the spin-up and spin-down bands necessitates spin relaxation in order to restore the equilibrium condition, an a.c. spin current is emitted into the SS layer where it gets dissipated (or reflected back [170]), which explains the term spin sink.

Spin pumping contributes extrinsically and non-locally to the damping of the magnetisation precession in the SI layer, increasing the α in Equation 3.1. In fact, this significant enhancement of α was the initial clue on the additional angular momentum dissipation channel in these bilayered structures [171] and it was only later on that this observation was supplemented by a theoretical description of the spin pumping mechanism [172][173]. The expression for the injected spin current was derived by Tserkovnyak *et al.* as

$$I_s = \frac{\hbar}{4\pi} g_{eff}^{\uparrow\downarrow} \mathbf{M} \times \frac{d\mathbf{M}}{dt} [173], \tag{3.8}$$

where $g_{eff}^{\uparrow\downarrow}$ is the real part of the effective spin mixing conductance that describes how

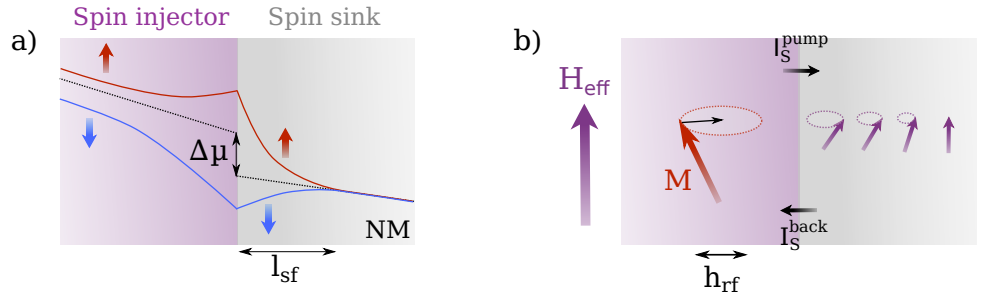

Figure 3.3: a) The chemical potential imbalance at the interface of a ferromagnetic SI and a normal metal SS causes a diffusion of the majority spins into the SS layer over the spin diffusion length (l_{sf}) during which the spin current is gradually dissipated due to spin-flip scattering. b) The precessing magnetisation driven by the rf-field pumps a.c. spin current into the SS layer.

efficiently the spins can be effectively transported across the interface (i.e. it accounts for both the spin current leaving SI due to spin pumping as well as the spin current returning back to SI due to back-reflection at the further interfaces). The non-local, extrinsic contribution to the Gilbert damping α, on the other hand, was obtained as:

$$\alpha_{sp} = g_{eff}^{\uparrow\downarrow} \frac{\gamma\hbar}{4\pi M_s V} [173] \tag{3.9}$$

In Section 3.3.1 we will discuss how the non-monotonous temperature-dependence of α_{sp} relating to spin-fluctuations can reveal an antiferromagnetic phase transition.

3.1.3 Spin-to-charge current conversion

The spin current pumped from the SI layer into the SS layer by the precessing magnetisation can be re-converted to a perpendicular charge current through the inverse spin Hall effect (ISHE). This requires that the SS layer has a sufficiently strong spin-orbit coupling (SOC) or alternatively supports another mechanism of spin-to-charge conversion [48][49]. The symmetry of the electric field generated by ISHE is given by:

$$E_{ISHE} \propto \mathbf{j}_s \times \boldsymbol{\sigma}, \tag{3.10}$$

where j_s is the spin current density and σ is the spin polarization vector. For future reference, in our spin pumping experiments we can manipulate σ by tuning the magnetisation orientation of the SI layer. Generally, ISHE is a useful tool for detecting and quantifying the spin current generated by spin pumping as the pure spin current in itself cannot be easily probed.

The microscopic mechanisms behind ISHE are analogous to those giving rise to AHE, which were discussed in Chapter 1 (Section 1.3). In this Chapter, however, the extrinsic mechanisms rather than the intrinsic one are of interest. The two extrinsic mechanisms, skew scattering and side jump, relate to the asymmetric impurity-scattering of the spin-up and spin-down conduction electrons. Skew-scattering is an inelastic scattering event

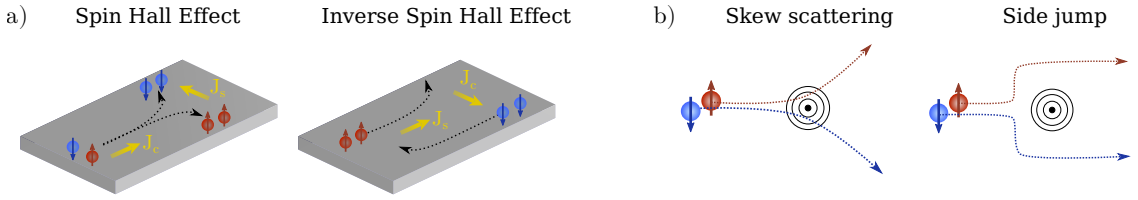

Figure 3.4: a) The spin Hall effect and its reciprocal effect, the inverse spin Hall effect. In the former a longitudinal charge current is converted to a transversal spin current while in the latter a longitudinal spin current is converted to a transversal charge current. b) The extrinsic microscopic mechanisms behind (I)SHE: the inelastic skew scattering involves asymmetric scattering of the spin-up and spin-down electrons while in the side jump they are deflected in opposite directions.

that results in the spin-up electron and spin-down electrons acquiring different k-vectors while the side-jump is an elastic scattering where the spin-up and spin-down electrons are deflected in opposite directions. Both mechanisms give a non-zero transversal resistivity component, yielding a pure transversal spin current in non-magnetic materials (SHE) and transversal spin-polarized current in ferromagnetic materials (AHE). The two mechanisms can be separated by the dependence of the transversal signal generated (ρ_{SHE}) on ρ_{xx}: if the mechanism behind SHE is skew scattering, $\rho_{SHE} \propto \rho_{xx}$ while if the mechanism is side jump, $\rho_{SHE} \propto \rho_{xx}^2$. Note that the intrinsic contribution also yields $\rho_{SHE} \propto \rho_{xx}^2$ so disentangling the two is challenging. In this Chapter our choice of material for the SS-layer is $Pd_{100-x}Ni_x$ alloy where skew scattering at the Ni sites has been assumed to dominate the SHE over the other mechanisms [174].

3.2 Experimental set-up

The experimental set-up that we use to realize the FMR-induced spin pumping measurements presented in this Chapter is described here. The main components of the set-up are a loop-gap resonator operating at a frequency of $\sim$ 9.75 GHz, a diode detector, and a benchtop voltmeter connected to the sample by electrical contacts. Thus it allows a simultaneously probing of the SI layer magnetisation dynamics through FMR and the spin-to-charge-conversion in the SS layer through ISHE measurement. The set-up is also connected to a helium cryostat so that the temperature range for its operation is from $\sim$ 4 to 300 K but in practice for stable measurements with sufficient signal-to-noise ratio the range is from 20 to 300 K.

The set-up (schematics shown in Figure 3.5) comprises of an rf-source, which generates microwaves that are passed through a circulator to the 3loop-2gap resonator inside

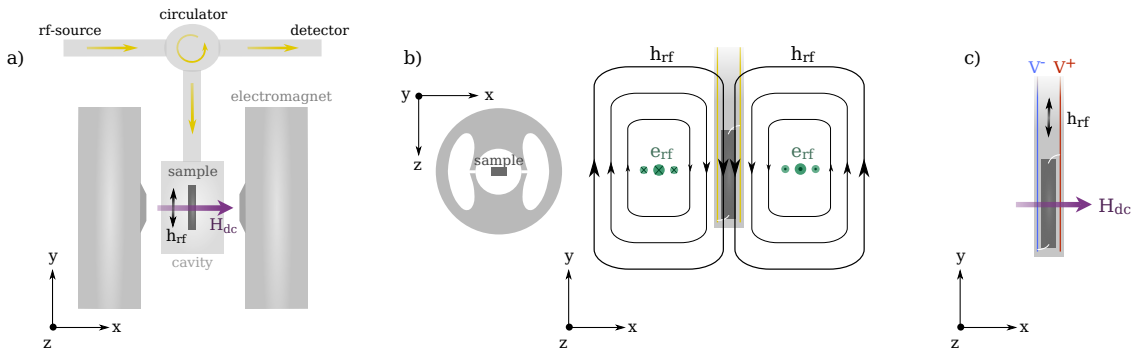

Figure 3.5: a) Schematics of the experimental set-up used for the FMR-induced spin pumping measurements. The sample is attached to a sample rod which for the sake of simplicity is omitted. b) The cavity used is a 3loop-2gap resonator (left) where the rf magnetic field is uniform and non-zero across the entire sample while the rf electric field on the sample is negligible as shown on the right. c) The sample is attached to a rod with electrical contacts, allowing for a measurement of voltage across the sample generated by ISHE.

which the sample (0.6x3.2 mm^2) attached to a sample rod can be placed. Inside the resonator the incident microwaves generate standing waves, resulting in electric and magnetic rf-fields (e_{rf} and h_{rf}, respectively, their distribution is shown in Figure 3.5b) at a resonance frequency defined by the properties of the resonator. The amplitude of the rf-magnetic field in our resonator is given by:

$$h_{rf} = 0.2\frac{PQ}{500}, \tag{3.11}$$

where P is the microwave power (typically 40 mW) and Q is the quality factor of the cavity (typically 700-1000). A part of the incident microwaves are absorbed by the cavity while the rest are reflected - the ratio of the two can be adjusted by the iris between the waveguide and the cavity. Prior to a measurement the system is tuned in such a way that none of the microwaves are absorbed by the cavity and all of them are reflected. The microwaves reflected by the cavity again pass through the circulator and they are directed towards the detector diode where they are converted to a voltage signal.

FMR-measurement

The bilayered SI/SS sample is placed inside the resonator and its position is adjusted so that it is under maximum rf-magnetic field and minimum (ideally vanishing) rf-electric field, as shown in Figure 3.5b. The sample will absorb the incident microwaves and the maximum absorption occurs when h_{rf} equals to the resonance frequency of the system, which in turn translates into the typical FMR signal at the detector as shown in Figure 3.6a. The signal-to-noise ratio of the FMR measurements is enhanced by a lock-in detection and modulating the H_{dc} with a small rf-component. For this reason, a typical measurement returns the field derivative of χ''_{yy} as a function of field rather than χ''_{yy} (recall that χ''_{yy} was defined in Section 3.1.1 in Equation 3.7).

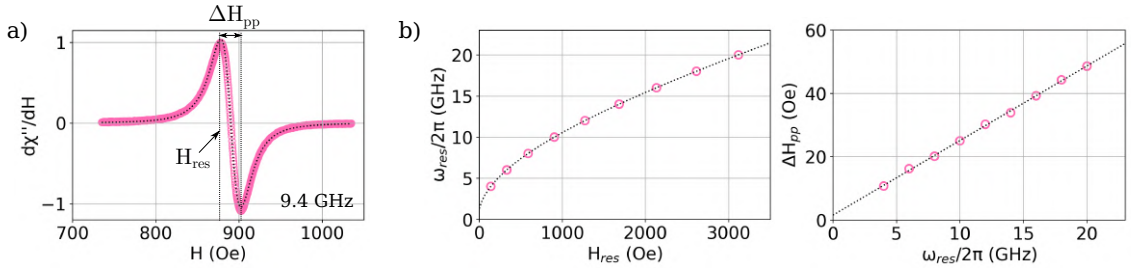

Figure 3.6: a) A typical FMR data obtained with the resonator-based FMR set-up at a fixed frequency, showing a change in the absorption of the rf-field as a function of field strength. The important information contained in this data is in the resonance field H_{res} and the peak-to-peak linewidth ΔH_{pp}. b) The variation of H_{res} and ΔH_{pp} with the resonance frequency measured at room temperature using a complementary broad-band FMR set-up. Equations 3.5 and 3.13 can be used to fit the variations, respectively. The FMR data at the different frequencies has the same shape as the one shown in a) for a narrow-band resonator-based FMR.

A typical data is shown in Figure 3.6a and fitted with

$$\frac{d\chi''_{yy}}{dH} = -2A_{sym}\frac{(\Delta H_{pp}\sqrt{3}/2)^2(H-H_{res})}{((\Delta H_{pp}\sqrt{3}/2)^2+(H-H_{res})^2)^2}, \tag{3.12}$$

where the two important fitting parameters are the resonance field H_{res} and the peak-to-peak linewidth ΔH_{pp}. The former yields information about the anisotropy of the FM layer (Equation 3.5) while the latter relates to the angular momentum dissipation through intrinsic and extrinsic channels. More explicitly,

$$\Delta H_{pp} = \Delta H_0 + \frac{2}{\sqrt{3}}\frac{\alpha\omega_{res}}{|\gamma|}, \tag{3.13}$$

where ΔH_0 is the inhomogeneous broadening that stems from the inhomogeneous sample properties and the consequent spread in resonance frequencies, and α is the total Gilbert damping.

We have conducted FMR measurements under different frequencies of the rf-field using a separate coplanar waveguide broadband FMR spectrometer (only operational at room temperature) and plotted H_{res} and ΔH_{pp} as a function of this frequency. This allows us to extract values for $\gamma, M_{eff}, H_u, \alpha$, and ΔH_0, as implied by Equations 3.5 and 3.13. In Figure 3.6b this is shown for a multilayer containing a 15 nm CoFeB layer (the other layers will be discussed later) where the fits yield $\gamma = 0.018$, $M_{eff} = 1.15$ kOe, $H_u = -18.7$ Oe, $\Delta H_0 = 0.42$ Oe and $\alpha = 0.0085$. We can see that ΔH_0 is vanishingly small compared to ΔH_{pp} meaning that the damping contribution from inhomogeneous broadening can be neglected.

When inside the resonator, the sample cannot be seen but its orientation relative to the applied dc-field H_{dc} can be changed by rotating the sample holder. The position of the sample can be read off the resonance field H_{res} because when the film plane is (anti)parallel to the H_{dc} the H_{res} ($\theta = \pm 90$ deg, see the definition of θ in Figure 1.16)

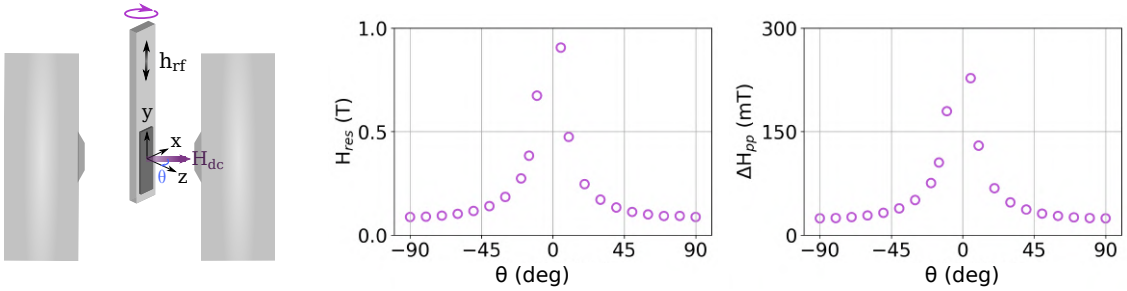

Figure 3.7: The sample orientation relative to the applied dc-field inside the cavity can be adjusted by rotating the sample holder. θ gives the angle between the film normal and the H_{dc}. H_{res} is maximized when the H_{dc} is along the film normal and minimized when H_{dc} is in the film plane. ΔH_{pp}, on the other hand, is minimum when H_{dc} is along the film normal and reaches maximum at intermediate angles. Here, the data for $\theta = 0$ deg is missing as the H_{dc} is limited to ~ 1.2 T in our set-up.

is minimized due to the FM layer magnetisation orienting along the in-plane easy axis. Conversely, when H_{dc} is perpendicular to the film plane ($\theta = 0$ deg), H_{res} is maximized. This behavior is shown in Figure 3.7 along with the variation of ΔH_{pp} with the sample orientation. The ΔH_{pp} is expected to reach a maximum slightly away from $\theta = 0$ deg and vanish when $\theta = 0$ deg [175]. Here, the data exactly at $\theta = 0$ deg is missing due to the H_{dc} on our measurement set-up being limited to ~ 1.2 T.

Measuring the spin-to-charge conversion

As shown in Figure 3.5c, the sample inside the cavity is connected to electrical contacts, allowing a measurement of the voltage signal across the sample generated by ISHE during the FMR. In the sample, the spin current flows from the SI layer to the SS-layer (z-direction, see Figure 3.8 for the coordinate system) and as the magnetisation of the spin injector is along the x-direction, the ISHE voltage (V_{ISHE}) is generated in the y-direction (recall Equation 3.10) as shown in Figure 3.8. The ISHE is expected to give a symmetric Lorentzian signal as the injection of a spin current into the SS depends on the precession amplitude of the SI magnetisation, which again depends on χ''_{yy}. Moreover, following from Equation 3.10, if the stacking order of the spin sink is reversed (i.e. $j_s \rightarrow -j_s$) or if the magnetisation of the spin injector is reversed ($\sigma \rightarrow -\sigma$), the signal changes sign.

A typical voltage signal showing these characteristic features of ISHE is demonstrated in Figure 3.8 for a sample with composition CoFeB(15)/Cu(3)/$Pd_{90}Ni_{10}$ (10 nm). Note that we typically convert the voltage signal into a charge current by dividing it by the two-point resistance (R_{2p}) and then normalize the signal to the incident rf-power h_{rf}^2. The electric signal can be fitted using a function

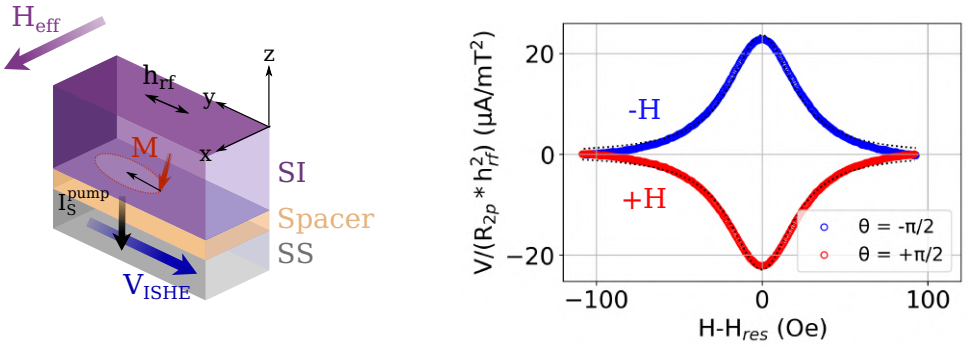

Figure 3.8: (Left) Typical sample for FMR-induced spin pumping experiments comprising of a spin injector (SI) and a spin sink (SS) separated by a spacer layer. SI injects spin current into the SS where it is converted into a voltage signal through ISHE. (Right) The voltage across the sample as a function of field strength shows symmetric Lorentzian signal around the resonance field H_{res}. Reversing the magnetisation direction reverses the sign of the signal as expected for the symmetry of ISHE. Here $\theta = -\pi/2$ and $+\pi/2$ indicate two magnetisation orientations antiparallel to each other, see Figure 3.7 for the definition of θ in our setup.

$$V = V_{sym}\frac{(\Delta H_{pp}\sqrt{3}/2)^2}{(\Delta H_{pp}\sqrt{3}/2)^2+(H-H_{res})^2} + V_{asym}\frac{(\Delta H_{pp}\sqrt{3}/2)(H-H_{res})}{(\Delta H_{pp}\sqrt{3}/2)^2+(H-H_{res})^2}. \quad (3.14)$$

The symmetric contribution (V_{sym}) can arise from ISHE [176] while the antisymmetric contribution (V_{asym}) can arise from AHE [176] or transverse AMR [177] (tAMR, sometimes referred to as planar Hall effect (PHE)), which contrary to ISHE depends on the phase of the precession. The parasitic contributions from the tAMR and AHE are collectively known as spin rectification effects (SRE) and they stem from the nonlinear coupling of an oscillating current and oscillating resistance of the magnetic material. In our experiments an oscillating rf-current could originate from a non-vanishing rf electric field on the sample but due to the geometry of the resonator used in this work this should be a minor concern. It is, however, noteworthy that if the phase shift at resonance is not exactly $\pi/2$ (for example eddy currents in the adjacent metallic layers can bring about such dephasing [178]), the SRE can also give a symmetric contribution and thus cause an overestimation of the ISHE. However, if the signal is primarily symmetric as is the case in our samples (shown in Figure 3.8) it is unlikely that the SRE effects are playing a major role.

One way to disentangle the contributions from ISHE and SRE is to measure the voltage signal under varying orientations of the external field, i.e. under varying orientations of the spin polarization axis (σ in Equation 3.10). In our set-up, we can vary the polar angle θ of the H_{dc} as shown in Figure 3.9 and for such a scan the behavior of ISHE, AHE, and tAMR are well known. Following from Equation 3.10, ISHE should have a sine-dependence on the magnetisation orientation (in effect, σ). However, in our set-up we are rotating the sample orientation relative to the external field and the magnetisation is not expected to follow the field smoothly due to the strong shape anisotropy of the thin films. Instead of the smooth sine-behavior we expect sharp switches of the magnetisation from one in-plane direction to the opposite one when the field is along the film normal, and this translates to a sharp reversal in the V_{ISHE} polarity at the same angle. A quantitative expression for this dependence has been derived by Ando *et al.* [179]. The polar angular

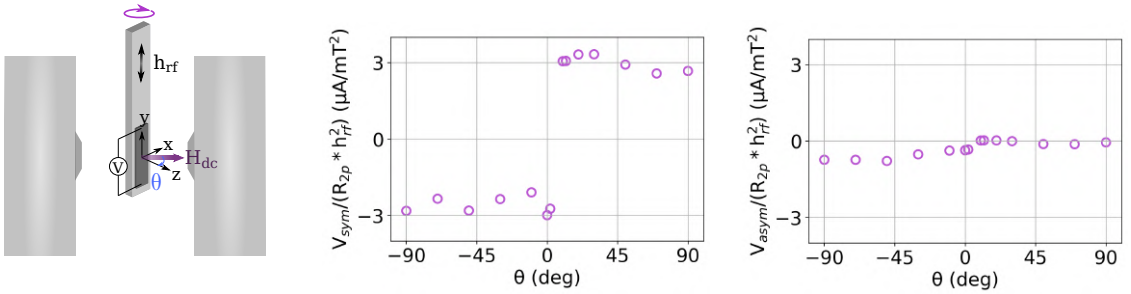

Figure 3.9: V_{sym} and V_{asym} (extracted using Equation 3.14) as a function of the polar angle of the H_{dc} (θ). As expected for a dc-voltage signal primarily originating from ISHE, V_{sym} is significantly larger than V_{asym} and the former shows the expected sign reversal corresponding to the magnetisation direction switching at $\theta = 0$, i.e. when the field is along the film normal.

dependencies of AHE and tAMR have been derived by Rojas-Sánchez *et al.* [180] where an additional angular dependence is introduced by the fact that not only σ but also the e_{rf} orientation changes when the sample is rotated. For the tAMR, the angular dependence shows local maxima slightly away from the angle at which the field is along the film normal. In Figure 3.9 we show the angular dependence of both V_{sym} and V_{asym} for a typical sample with PdNi as spin sink and it is apparent that V_{sym} is the dominant contribution, primarily originating from ISHE as indicated by the angular behavior.

Choice of the measurement configuration

The advantages of using a cavity resonator over a broadband strip-line for the FMR-induced spin pumping measurements are manifold. First, the resonator we are using (3loop-2gap) ensures that the e_{rf} on the sample is negligible, as was shown in Figure 3.5b, and therefore the spin rectification effects are negligible. As discussed before, a non-zero e_{rf} (common problem in e.g. in coplanar waveguide broadband FMR set-ups) would generate an alternating rf-current in the sample, which again would give rise to other parasitic effects that contribute to the voltage signal measured, complicating the disentangling of the ISHE contribution. Second, the h_{rf} on the sample is stronger ($\sim$ 0.5 Oe), resulting in a stronger ISHE signal. Finally, the h_{rf} is more uniform across the sample, resulting in a more uniform magnetisation precession in the entire sample. However, these advantages come at the expense of the set-up being narrowband, i.e. the excitation frequency cannot be changed. We have circumvented this problem by using a broadband strip-line set-up to obtain supplementary frequency-dependent data that was shown in Figure 3.6.

3.3 Spin pumping as a probe of magnetic fluctuations

The spin pumping experiments combine both FMR and ISHE measurements and in this Section we will show that this makes them an ideal tool for probing linear and non-linear spin fluctuations, which manifest as non-monotonous temperature-dependence of the corresponding spin susceptibilities across magnetic transition temperatures. We will first briefly recap the previous work conducted in the AF spintronics team at SPINTEC on how linear spin fluctuations acting on the linear susceptibility of the spin sink (SS) result in an enhanced damping of the spin injector (SI) dynamics around a magnetic phase transition. We will then move on to discussing our recent work on studying how the non-linear spin fluctuations around magnetic phase transitions can alter the spin-to-charge conversion efficiency of the SS layer.

3.3.1 Probing linear fluctuations in IrMn around the magnetic phase transition

The spin pumping efficiency strongly depends on the spin mixing conductance $g_{eff}^{\uparrow\downarrow}$, as was indicated by Equation 3.8. The $g_{eff}^{\uparrow\downarrow}$ is essentially a measure of how efficiently the spin current can cross the FM/NM interface. This quantity is not constant but has been shown to depend on the imaginary part of the dynamic spin susceptibility of the spin sink:

$$g_{SI/SS}^{\uparrow\downarrow} \propto \sum_k \frac{1}{\omega_{rf}} Im\chi_k^R(\omega_{rf}) [181], \tag{3.15}$$

where ω_{rf} is the (angular) resonance frequency of the FM layer and $\chi_k^R(\omega_{rf})$ is the *transverse* dynamic linear spin susceptibility (i.e. the rf-field is perpendicular to the detection direction). Recall that the non-local extrinsic damping contribution from spin pumping is given by

$$\alpha_{sp} = g_{eff}^{\uparrow\downarrow} \frac{\gamma\hbar}{4\pi M_s V} [173], \tag{3.16}$$

linking α_{sp} to $Im\chi_k^R(\omega_{rf})$. It is known that around the critical temperatures (T_c) of magnetic materials their order parameter undergoes the strongest linear fluctuations, significantly enhancing the $Im\chi_k^R(\omega_{rf})$ [182]. Qualitatively, this can be understood as follows: at $T \gg T_c$ the spins are not interacting so that collective fluctuations cannot be excited while at $T \ll T_c$ parallel alignment of the spins is strongly favored and therefore exciting spin fluctuations is more challenging. Due to this temperature-dependence of the $Im\chi_k^R(\omega_{rf})$ we would also expect to observe an enhancement in α_{sp} at the magnetic phase transition of the SS layer [181].

The temperature dependence of α_{sp} in a system with an antiferromagnetic SS-layer

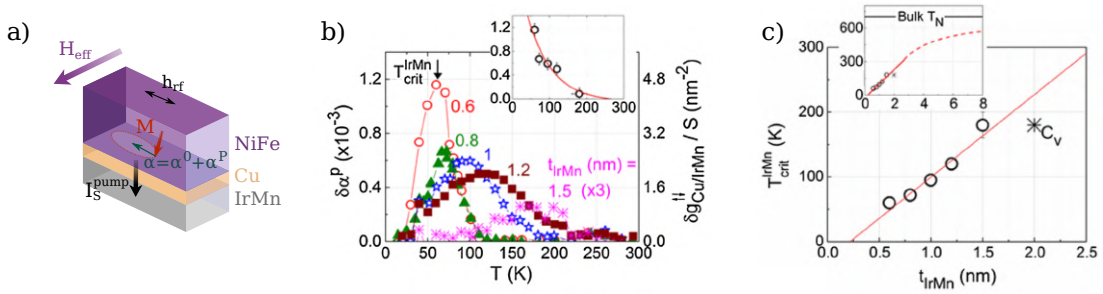

Figure 3.10: a) The active layers of the stack used by Frangou *et al.* [162] for spin pumping measurements from which the spin-pumping related non-local extrinsic damping α_{sp} was obtained. b) The temperature-dependence of α_{sp} shows a maximum at a temperature coinciding with the Néel temperature of the IrMn-layer (T_{crit}^{IrMn}). Note that the T_{crit}^{IrMn} depends on the thickness of the IrMn layer (t_{IrMn}) as shown in c) where the dependence is fitted with a function obtained from Ref [183]. The inset in b) shows α_{sp} as a function of T_{crit}^{IrMn} while the inset in c) shows a wider range of t_{IrMn}. Both b) and c) are extracted from Ref. [162].

was measured by our AF-spintronics team [162]. The stack used by Frangou *et al.* was NiFe (8)/Cu (3)/γ-IrMn$_3$ (t$_{IrMn}$)/Al (2 nm) as illustrated in Figure 3.10a, where t_{IrMn} ranged from 0 to 1.5 nm. The Cu spacer layer magnetically decoupled the SI and SS layers, preventing magnon spin transport, without influencing the interfacial electronic spin transport (spin diffusion length of Cu is > 300 nm). Due to cancellation of the other terms, in this trilayer system $g_{eff}^{\uparrow\downarrow} \sim g_{Cu/SS}^{\uparrow\downarrow}$ [184]. The temperature-dependence of the total α was extracted from the temperature-dependence of ΔH_{pp} assuming that ΔH_0 was negligible over the entire temperature range (as verified experimentally at room temperature). The local intrinsic contribution α_0 was disentangled from the spin pumping contribution α_{sp} by measuring α as a function of temperature when $t_{IrMn} = 0$ and removing this background from the measurements where $t_{IrMn} \neq 0$. The remaining signal is then α_{sp} as a function of temperature, which is shown in Figure 3.10b for varying t_{IrMn}. The signal shows a clear maximum at a specific temperature that increases with increasing t_{IrMn} - in fact, this temperature coincides with the thickness-dependent Néel temperature T_N of the IrMn layer as shown in Figure 3.10c. This experimental observation is in a good agreement with the theoretical prediction of enhanced α_{sp} at a magnetic phase transition temperature relating to stronger linear transverse spin fluctuations at this temperature. In case of an antiferromagnetic phase transition, this is an especially useful tool for detecting the typically experimentally elusive T_N in thin films, where techniques relying on large magnetic volumes (like neutron diffraction) reach their limit.

In the following sections we show a continuation for this work on detecting spin fluctuations with the FMR spin pumping setup but rather than probing the linear spin fluctuations through the damping of the FM dynamics (SI layer) we probe the non-linear spin fluctuations acting on the non-linear susceptibility through the spin-to-charge conversion in the SS layer. Instead of using γ-IrMn$_3$ as the spin sink, we have opted for $Pd_{100-x}Ni_x$ as the SS layer as it is expected to show enhanced spin fluctuations, which facilitates their detection.

3.3.2 Probing non-linear fluctuations around the magnetic phase transition

We will now discuss how the pure spin current generated by spin pumping can be used as a probe of the non-linear spin fluctuations of the SS-layer. In short, this is because the conduction electron spins can interact with the localised spins in the magnetic spin sink, thereby giving rise to novel spin-dependent transport phenomena. Gu *et al.* have linked these transport properties to the non-linear spin susceptibilities and hence to non-linear spin fluctuations by extending the Kondo model [185]. In order to do so, they have made a number of assumptions: 1) the number of spin-up and spin-down electrons is equal as we are near T_c, 2) the skew-scattering events only take place at the Ni-impurity sites, 3) only on-site spin correlations are considered while spin-spin interactions from the neighboring

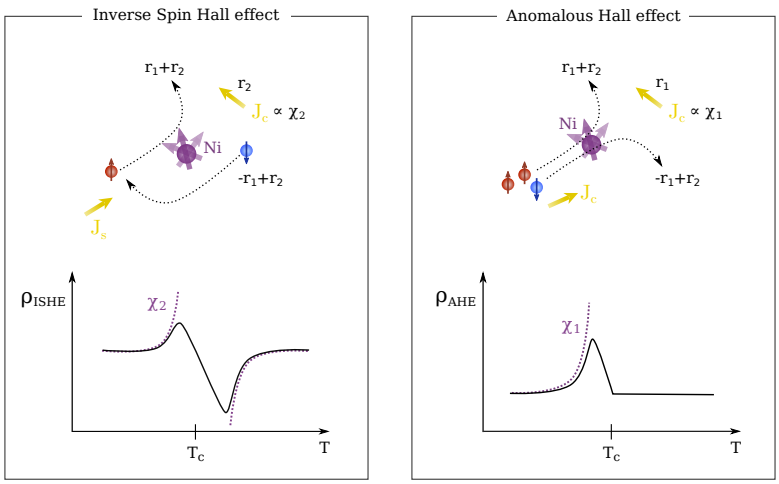

Figure 3.11: In inverse Spin Hall effect (ISHE) the spin-up and spin-down electrons are scattered to the same side so that the transverse current is proportional to r_2, which is again proportional to χ_2. In anomalous Hall effect (AHE) the scattering is to the opposite sides so that the transverse current is proportional to r_1 and thus to χ_1. The temperature-dependences of AHE and ISHE across a magnetic phase transition temperature T_c show anomalous behavior originating from the anomalous behavior of χ_2 and χ_2, respectively, across T_c. Figure modified from Refs. [185] and [186].

sites are ignored [186][185]. In the framework of this model, the scattering amplitudes for the spin-up and spin-down electrons are obtained as $r_1 + r_2$ and $-r_1 + r_2$, respectively. Here $r_1 \approx \frac{\chi_1}{\mu_B^3 \beta^2}$ and $r_2 \approx \frac{\chi_2}{\mu_B^3 \beta^2}$, where χ_1 and χ_2 are the first and second-order non-linear spin susceptibilities, respectively, and $\beta = 1/k_B T$.

As illustrated in Figure 3.11 in ISHE the spin-up and spin-down electrons are scattered to the same side so the signal measured is a sum of the scattering amplitudes, i.e. proportional to r_2 and thus to χ_2. On the other hand, as also illustrated in Figure 3.11, in AHE the scattering is to the opposite sides so that the signal will be a difference of the scattering amplitudes, i.e. proportional to r_1 and thus to χ_1. Similarly to the linear spin susceptibility χ_0, both χ_1 and χ_2 show characteristic divergent behavior across magnetic phase transitions as illustrated in Figure 3.11 for a ferromagnetic material. The behavior of non-linear spin susceptibilities have been calculated for a ferromagnet using mean-field approximations [187] but note that different behavior is expected for antiferromagnets and spin glasses [188]. Consequently, we would expect the ρ_{AHE} and ρ_{ISHE} to follow this characteristic behavior, as also illustrated in Figure 3.11. In this Chapter we will focus on the temperature-dependence of ρ_{ISHE} as we can access this effect conveniently with the FMR spin pumping set-up as discussed earlier.

The anomaly in ρ_{ISHE} with the expected peak-and-dip shape has been already demonstrated using lateral spin valve devices [186] that are illustrated in Figure 3.12a where a pure spin current is generated at the interface of a permalloy ($Ni_{81}Fe_{19}$, Py) and Cu wires, transmitted through the Cu wire and finally absorbed by PdNi wire where it is converted to a charge current through ISHE. Conducting a field-sweep while measuring the R_{ISHE}

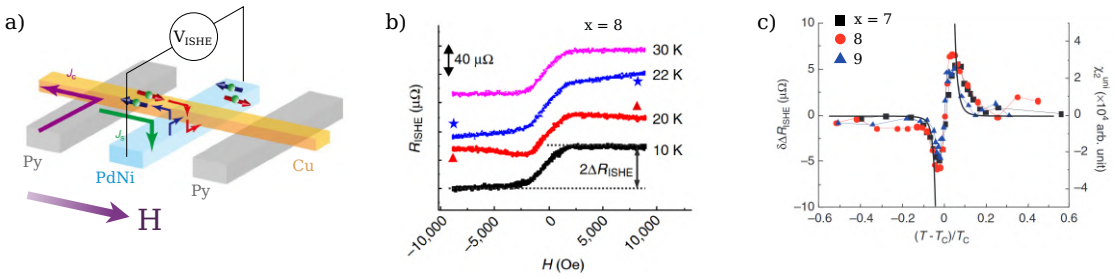

Figure 3.12: All figures are adapted from Ref. [186]. a) Schematics of a lateral spin valve device. A pure spin current is generated at Py/Cu interface and injected to PdNi wire where it is converted to a charge current via ISHE and detected electrically. b) R_{ISHE} as a function of field for different temperatures for $Pd_{92}Ni_8$ with $T_c = 21$ K. Anomalous behavior (i.e. no saturation) is observed around T_c. c) ΔR_{ISHE} extracted from b) as a function of temperature (normalized to T_c) shows the characteristic dip-and-peak behavior of χ_2.

reveals a switching behavior shown in Figure 3.12b (characterised by ΔR_{ISHE}) relating to the switching of the magnetisation direction of the Py wire and effectively switching of the polarization direction of the spin current. Plotting ΔR_{ISHE} as a function of temperature (Figure 3.12c) reveals the expected anomaly around the T_c of $Pd_{100-x}Ni_x$, where T_c increases with increasing x [186]. In this study the $Pd_{100-x}Ni_x$ with $x = 7,8,9$ is behaving like a weak ferromagnet with a $T_c = 16,21,32$ K, respectively [186]. Note that these T_c are significantly lower than those reported previously for bulk PdNi [189][190] but the authors attributed this to the non-homogeneous distribution of Ni as a result of the ion implantation method used for fabricating the PdNi wires. Moreover, only the top 10 nm of the 20 nm Pd wires contain Ni, which could affect the T_c.

In this Chapter the aim is to study the temperature-dependence of R_{ISHE} using the spin-pumping method instead of lateral spin valves. The advantages of our method are that it does not require complicated nanofabrication process to prepare the samples (cutting the samples into a rectangular shape with a diamond saw is sufficient) and ideally it could allow for a simultaneous probing of linear and non-linear fluctuations (we will discuss the sample requirements later on in this Chapter). Initially, the intention was to continue on using the antiferromagnetic IrMn as the spin sink but due to the low signal-to-noise ratio and inconclusive preliminary attempts we first sought to verify the viability of our method by using a spin sink with presumably stronger spin fluctuations. For this purpose we selected $Pd_{100-x}Ni_x$ as a spin sink due to its reported weak ferromagnetic nature above critical x [191][192] implying stronger spin fluctuations as well as the previous reports on second-order non-linear spin fluctuations [186] discussed above.

3.4 Characterization of the $Pd_{100-x}Ni_x$ thin film properties

This section is dedicated to the characterization of the structural, magnetic, and magnetotransport properties of the $Pd_{100-x}Ni_x$ thin films (10 nm) grown at SPINTEC by dc magnetron sputtering by Patrick Warin. The concentrations of Ni in this work are primarily on the low side (x = 6-12), so we can consider the system to be a dilute alloy, i.e. to comprise of the non-magnetic Pd host with magnetic Ni impurities. Identifying the magnetic phase transition temperature(s) and the magnetic nature of the phases of these films is essential for the follow-up spin pumping studies on the non-linear spin fluctuations in this material.

3.4.1 Structural characterization

The structure of our $Pd_{100-x}Ni_x$ thin films was probed by Eric Gautier at SPINTEC using a high-resolution scanning tunneling electron microscope (HR-STEM). We have characterised the sample with $x = 12$ to verify the structure and thickness of the thin films and to get a preliminary indication of the Ni-atom clustering.

The HR-STEM images show a cross-section of the films and allow identifying the atom positions as well as the distribution of the different elements within the film as shown in Figure 3.13. The films are polycrystalline as expected from films grown by sputtering, and two layers of ∼10 nm and ∼2 nm corresponding to $Pd_{88}Ni_{12}$ and Al layer can be distinguished. The thicknesses are in line with the nominal ones of 10 and 3 nm, respectively. The distribution of Ni atoms within the Pd host appears relatively uniform, so that large Ni clusters are not observed. However, due to the statistical fluctuations in the Ni distribution, some small clusters of a few Ni atoms are found. Note that in STEM the elements are distinguished based on their atomic number Z and therefore oxygen having Z close to that of Al can give rise to a spurious signal. Therefore, the seeming presence

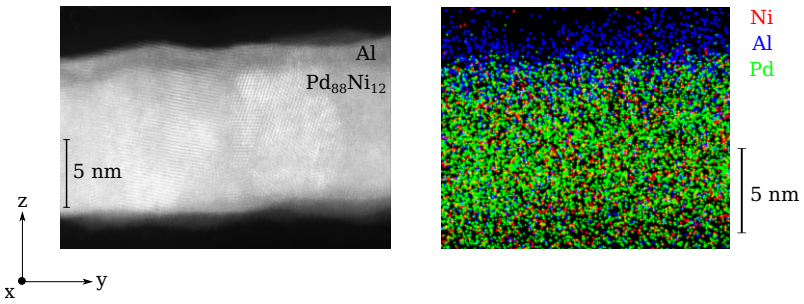

Figure 3.13: (HR-STEM images of the $Pd_{88}Ni_{12}$/Al thin film showing a cross-section perpendicular to the film plane. The left side image shows the atomic positions and the right side image shows the elemental distribution. These images reveal the polycrystalline structure of our 10 nm $Pd_{88}Ni_{12}$ thin films and a random distribution of Ni atoms inside the Pd matrix.

of Al in the PdNi matrix as implied by Figure 3.13 is more likely the presence of oxygen.

3.4.2 Magnetic characterization

The highly non-trivial magnetic properties of bulk $Pd_{100-x}Ni_x$ (PdNi) alloys have been extensively studied. They show a paramagnetic to ferromagnetic phase transition when the Ni concentration x reaches a critical value of $x \sim 2.3$ [191] at which the local spin fluctuations at the isolated Ni atoms begin to interact in order to form a long-range magnetic ordering [192]. It has been shown through neutron scattering experiments that this phase transition is not uniform, i.e. the Ni atoms do not each gain an equal magnetic moment but rather depending on their immediate environment either form a giant polarization cloud (Ni-rich local environment) or remain non-magnetic (Ni-poor local environment) [191][193]. There are also reports on a large orbital moment on the Ni-atoms in dilute PdNi [194] and the Ni atoms polarizing the host matrix around them over a distance of $\sim$ 1 nm [193]. Behavior similar to the bulk samples has also been demonstrated in relatively thick films ($\sim$ 50 nm) of $Pd_{86}Ni_{14}$ [195].

We have measured the magnetisation of our $Pd_{100-x}Ni_x$ thin films ($\sim$ 10 nm) as a function of (increasing) temperature following from either zero-field (ZFC) or +1 T field-cooling (FC) protocol. For the field-cooling measurements, both cases of field perpendicular (out-of-plane, oop) and parallel (in-plane, ip) to the film surface were considered. The measurements were conducted as follows: the system was first cooled down under the specified field-condition and then the magnetisation was measured while warming the system up under a small measuring field of 500 Oe applied in the same direction as the cooling field. A typical measurement outcome is shown in Figure 3.14a for $Pd_{92}Ni_8$,

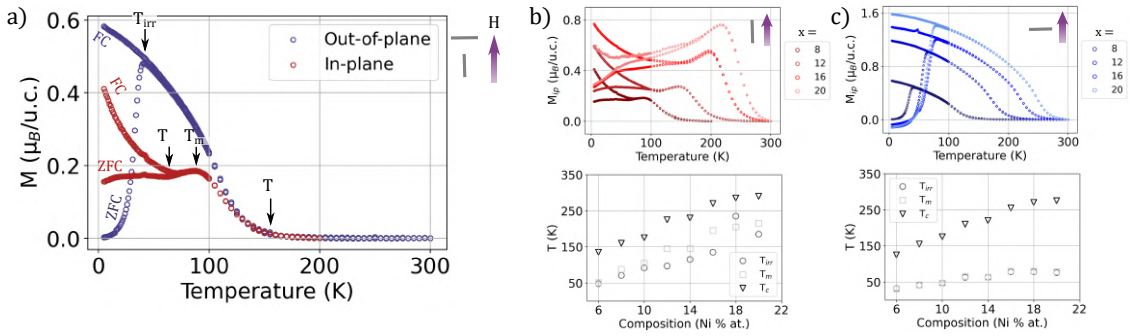

Figure 3.14: a) Magnetisation as a function of temperature in bare $Pd_{92}Ni_8$ (10 nm) after zero-field cooling (ZFC) and field-cooling (FC). Out-of-plane signifies that field is perpendicular to the film plane while in-plane signifies that it is in the plane of the film. The three different critical temperatures are denoted with arrows. b) Composition dependence of the magnetisation as a function of temperature when the external field is in-plane. Each critical temperature denoted in a) increases with increasing Ni-content. c) Composition dependence of the magnetisation as a function of temperature when the external field is out-of-plane. Again the critical temperatures increase with increasing Ni-content. In b) and c), for the sake of clarity, not all x measured are shown in the top figure.

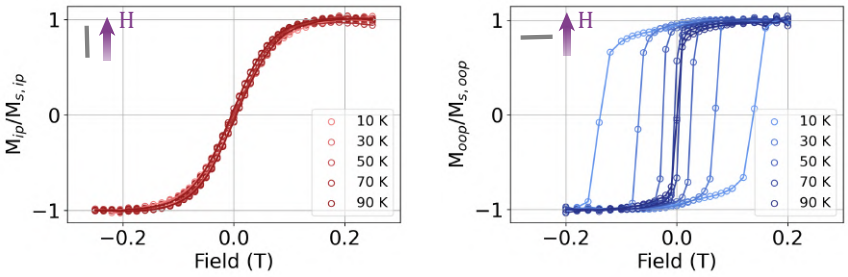

Figure 3.15: Magnetisation as a function of an external field at various temperatures when the field is applied in the plane of the film (right plot) or along the film normal (left plot). The square hysteresis loop in the latter case reveals strong PMA in the system.

where two prominent features can be observed: i) out-of-plane magnetisation is more stable than the in-plane one (we note that extrapolating the FC data in Figure 3.14a to 0 K indicates the same magnetisation for both field orientations, as expected) and ii) for both orientations there are more critical temperatures than the expected weak ferromagnetic Curie temperature T_c.

The first feature suggests perpendicular magnetic anisotropy (PMA) where the film normal is the easy axis of magnetisation. This is also confirmed by the field-dependent magnetisation measurements as shown in Figure 3.15 where square-shaped hysteresis loops with large coercivity are observed for oop field while for ip field the coercivity vanishes. PMA in PdNi has been observed also in thin films with thicknesses of 35 [196] and 100 nm [197] but for bulk samples in-plane anisotropy (easy axis along [100]) has been typically reported [198][199]. The origin of the PMA in our thin films is not clear but one possibility is the strong magnetostriction in PdNi [200] that has been proposed to emerge from pseudo-dipole interactions between the Ni moments and the induced Pd moments [201]. Magnetostriction has been reported to contribute for example to PMA of Co/Pd multilayers [202]. Identifying the exact origin of the PMA is beyond the scope of this thesis as we are more interested in the criticial temperatures of the magnetic phase transitions, but it would definitely be an interesting topic for further studies using e.g. atomistic simulations.

The second feature of various critical temperatures indicates that our PdNi films have a magnetic phase that is more complex than the expected weak ferromagnetic phase. The T_c indicating the ferromagnetic transition does not depend on the field orientation and follows the composition dependence previously reported for bulk samples [189]. Increase in the T_c with increasing Ni-content results from the distances between Ni atoms/clusters decreasing and as a result the exchange interactions becoming stronger. However, below T_c, both the oop and ip measurements reveal another critical temperature relating to the bifurcation point of the ZFC and FC measurements, here referred to as T_{irr} after the irreversible behavior. In the case of oop-field, T_{irr} is at lower temperature than in the ip-case and the magnetisation during ZFC vanishes at very low temperatures, while in the case of ip-field the ZFC measurement plateaus at low temperatures. Furthermore, for the ip-

orientation, there seems to be a third critical temperature between T_c and T_{irr} indicating a local maximum in magnetisation (T_M), which is absent for the oop-orientation.

T_{irr} is a characteristic feature of spin/cluster glass materials where it indicates magnetic frustration in the system, which results in the spins freezing in random orientations and having a multitude of equivalent ground states [203]. Frustration can arise for example from competing ferromagnetic and antiferromagnetic interactions that cannot be mutually satisfied. The fact that we are observing T_{irr} in our system could imply (reentrant) spin or cluster glass behavior, which hasn't been observed in PdNi before. It is known from bulk PdNi that the long-range magnetic ordering arises from the clustering of few Ni atoms that also polarize the surrounding Pd atoms. Competing interactions between these clusters, such as ferromagnetic, dipole-dipole, and RKKY interactions could cause frustration and in effect, cluster glass -like behavior. For example, T_M could be explained by dipole-dipole interactions favoring antiparallel alignment of the clusters that have gained a magnetic moment. However, further modeling using e.g. atomistic simulations has to be carried out in order to understand whether this model can explain the other features such as different T_{irr} and ZFC behaviors deviating for the ip- and oop-fields, as well as the absence of T_M for the oop-field. It should be also noted that T_{irr} is not a unique feature of spin/cluster glasses but is also observed in superparamagnetic systems. In order to distinguish between the two, ac-susceptibility measurements could be carried out because the behavior of susceptibility at T_{irr} differs for spin glasses, cluster glasses, and superparamagnets, as does the frequency-dependence of T_{irr}. We have attempted such measurements during this work but due to the small magnetic signal of our samples the signal-to-noise ratio was poor. Further attempts would therefore require increasing the magnetic signal while maintaining the magnetic nature of the samples, which is not a trivial task.

3.4.3 Magnetotransport properties

We have patterned bare $Pd_{100-x}Ni_x$ films (grown simultaneously with the spin pumping samples that also have CoFeB and Cu layers) into Hall bars ($w = 24$ nm, $l = 120$ nm) using optical lithography and subsequent ion beam etching. Illustration of the Hall bar geometry as well as an optical image of the patterned device is shown in Figure 3.16a. Note that in these measurements the field is always along the film normal (out-of-plane, oop).

The temperature dependence of ρ_{xx} for $Pd_{92}Ni_8$ ($T_c \sim 150$ K, $T_{irr} \sim 50$ K for oop field) is shown in Figure 3.16b. It shows typical metallic behavior with no apparent anomalies relating to the two critical temperatures identified in the magnetic measurements with the oop field (Figure 3.14c). This is in contrast with the similar measurement on 60 nm $Pd_{86}Ni_{14}$ where a local maximum coincided with the onset of the weak ferromagnetism [195]. However, their measurement was conducted with the field in-plane and moreover, their magnetisation as a function of temperature is dissimilar to that of our PdNi films.

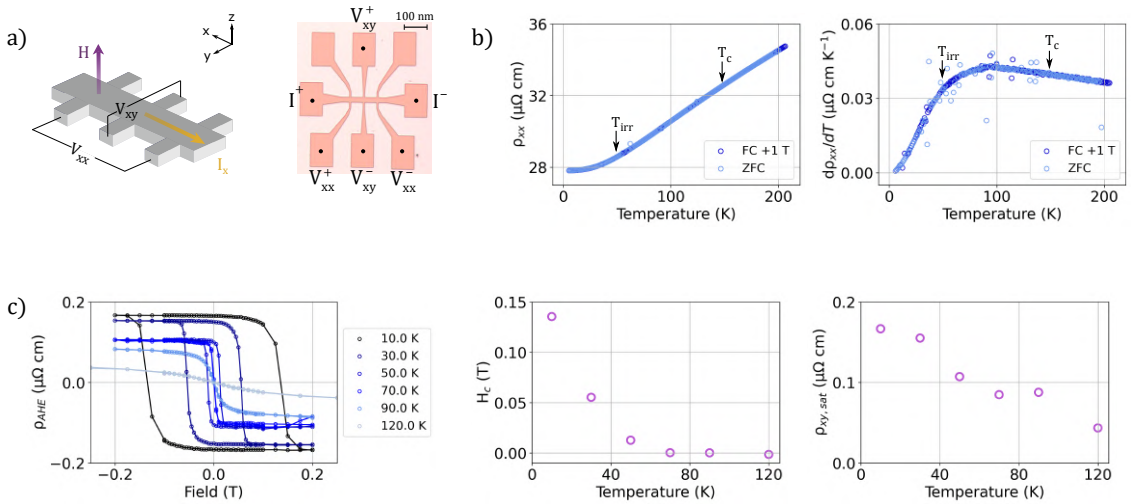

Figure 3.16: a) Illustration of the typical Hall bar geometry and an optical image of the patterned devices. b) Temperature dependence of ρ_{xx} and its derivative during +1 T field-cooling and zero-field cooling for $Pd_{92}Ni_8$. The critical temperatures identified from the magnetic measurements (with field out-of-plane) are denoted with arrows. c) The field-dependence of ρ_{xy} at various temperatures. A sizable AHE with a large coercivity can be observed with the amplitude vanishing when going towards T_c.

Measuring the ρ_{xx} as a function of temperature of our system with the field in-plane could provide a more direct comparison with the previous reports. Nevertheless, this discrepancy further hints towards our PdNi thin films having a more complex magnetic state going beyond the previously reported weak ferromagnetism.

The field-dependence of ρ_{xy} for $Pd_{92}Ni_8$ at varying temperatures reveals strong, square-shaped hysteresis behavior (Figure 3.16c) originating from AHE. The AHE amplitude gradually vanishes when T_c is approached, as expected for a system where the AHE is allowed due to the $\mathscr{T}$-symmetry being broken by the net magnetisation. The coercive field (H_c), on the other hand, vanishes already at around 60 K, which is well below T_c. This is well in line with the magnetic measurements in Figure 3.15 where at and above 70 K the hysteresis loops have a vanishing coercivity. Moreover, the temperature at which the H_c vanishes seems to coincide with T_{irr} and whether it is a coincidence or there is a correlation requires further investigation and could provide further hints about the irreversible transition.

In order to probe the anisotropy of the magnetotransport properties, we have measured the dependence of ρ_{xx} (through $AMR_{||}$, which was defined by Equation 1.7) and ρ_{xy} on the external field orientation defined by angle θ as illustrated in Figure 3.17. Note that the field is rotated in the plane perpendicular to the current channel, meaning that the non-crystalline contributions to the anisotropy are suppressed. The angular dependencies are shown in Figure 3.17. The ρ_{AHE} shows cosine-like behavior but the maxima and minima are widened and the transitions between them are sharper. This is another demonstration of the PMA present in our system: the out-of-plane direction is the easy axis and therefore the magnetisation lags behind the rotating external field by staying along the film

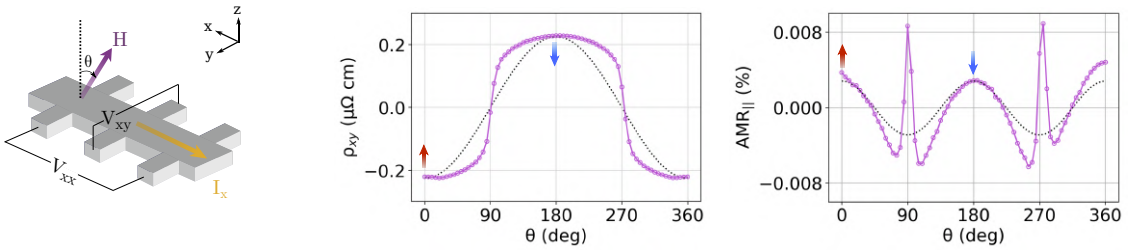

Figure 3.17: The angular dependence of the magnetotransport properties. A field of 0.4 T is rotated in the plane perpendicular to the current channel and the field orientation is defined by the polar angle θ. ρ_{AHE} shows characteristic behavior for a system with strong anisotropy causing the magnetisation to lag behind the external field and therefore to deviate from the expected cosine-dependence (dotted line). $\text{AMR}_{||}$ shows $\cos 2\theta$ behavior (black dotted line) with superimposed sharp peaks at the field orientation where the magnetisation reverses.

normal as long as possible. The $\text{AMR}_{||}$, on the other hand, shows sharp maxima when the field is aligned in-plane (the point at which the magnetisation reverses as observed in the angular dependence of ρ_{xy}) and broader local maxima when the field is out-of-plane. In our measurement configuration we are rotating the field in the plane perpendicular to the current channel, meaning that the non-crystalline AMR component should be minimum (the different contributions of AMR were discussed earlier in Chapter 1, Section 1.5.4). On the other hand, our films are polycrystalline as we have demonstrated using TEM in Section 3.4, so that also the crystalline component to AMR should cancel out. It is therefore peculiar that in this sample and configuration we are observing a clear θ-dependence of the $\text{AMR}_{||}$. Qualitatively, the data seems two have two contributions: a $\cos 2\theta$ background with sharp peaks coinciding with the reversal of the magnetisation. The $\cos 2\theta$ background has the form of a conventional non-crystalline AMR, which can here result from the fact that the rotation plane is not strictly perpendicular to the current channel due to a manual alignment of the Hall bar relative to the external field rotation plane. The peaks, on the other hand, seem to relate to the $\text{AMR}_{||}$ becoming stronger when the magnetisation is in the plane of the film and the reason for this is requires further investigation.

3.5 Probing non-linear fluctuations in $\text{Pd}_{100-x}\text{Ni}_x$ at the glassy transition

We will now move on to the experimental demonstration on how FMR-induced spin pumping measurements can be used to probe the second-order non-linear spin fluctuations as was discussed in terms of theory in Section 3.3.2. The operating principle of our FMR set-up was discussed in Section 3.2. In this Section we conduct temperature-dependent spin pumping measurements on a sample comprising of a CoFeB spin injector (SI) and $\text{Pd}_{100-x}\text{Ni}_x$ spin sink (SS), separated by a thin spacer layer (here Al or Cu). The choice of

CoFeB over the typical NiFe as the SI is based on the elimination of a non-monotonous temperature-dependence of ρ_{ISHE} originating from the self-induced ISHE in the SI layer - spin pumping measurements on a bare FM layer have revealed this non-monotony to be strong in NiFe and negligible in CoFeB due to its smaller spin-orbit coupling [204]. The spacer layer in turn is essential for magnetically decoupling the SI and SS (thus inhibiting the magnonic spin transport) [205][206] but it has to have a long spin diffusion length in order to maintain the transparency of the interface for spin current. We will discuss two choices of spacers later in this Section.

3.5.1 Global detection of a magnetic phase transition through non-linear spin fluctuations

First, we measured a wide range of temperatures in order to understand the global dependence of V_{ISHE} on temperature. For this purpose, the temperature was changed using an external temperature controller and by adjusting the He-flow. At each new temperature, the resonator was given $\sim$ 10 min to reach a thermal equilibrium before conducting the FMR-measurement. After equilibration, a field-scan was conducted around H_{res} for two orientations $\theta = +\pi/2$ and $-\pi/2$ (recall the definition of θ in Figure 3.18a). The measurement time and the scan width were optimized for obtaining enough data points for a smooth plot.

For the first set of measurements we used Al spacer between the CoFeB SI and PdNi SS and sample dimensions of 0.4 x 2.4 mm^2. For one of these samples with $Pd_{92}Ni_8$ ($T_c \sim$ 160 K, $T_M \sim$ 70 K, $T_{irr} \sim$ 60 K), the measured voltage signal at 300 K, fitted with Equation 3.14, showed a large symmetric contribution (V_{sym}) and a small antisymmetric contribution (V_{asym}) as shown in Figure 3.18a for both sample orientations. The temperature-dependence of the V_{sym}, which relates to ISHE and therefore to non-linear spin fluctuations through χ_2 as discussed in Section 3.3.2, is shown here in Figure 3.18b. The behavior is largely monotonous down to $\sim$ 60 K, below which a small bump is ob-

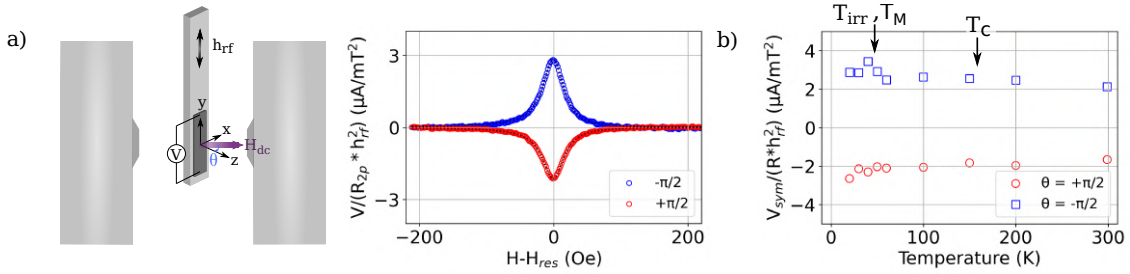

Figure 3.18: a) Voltage signal around the resonance field H_{res} of sample CoFeB/Al/$Pd_{92}Ni_8$ for two orientations of the sample where the spin polarization direction σ has been reversed, resulting in the reversal of the signal. b) A wide temperature-dependence of V_{sym} for the two sample orientations showing largely monotonous behavior and a small anomaly around 60 K, coinciding with the T_{irr} and T_M of $Pd_{92}Ni_8$.

served for the $\theta = -\pi/2$ orientation while for the $\theta = +\pi/2$ a slight decrease is observed below $\sim$ 25 K. These changes in the charge current induced by V_{ISHE} occur in the temperature range at which T_M and T_{irr} were observed in the magnetic measurements. Around T_c, however, there are not sufficient data points to observe any anomalies. We have decided to first focus on the anomalous behaviour around T_M and T_{irr} by conducting a higher resolution temperature scan around this temperature.

3.5.2 High-resolution temperature scan in search of correlation between anomalous spin-to-charge conversion and non-linear spin fluctuations

For a high-resolution temperature-scan we have adopted a different way of changing the temperature of the sample. Following the method developed by Noël *et al.* [207], we set a fixed cavity temperature with the external temperature controller and then increase the power of the microwave excitation in order to increase the sample temperature and finally read out the temperature from the two-point resistance. We have repeated this measurement various times for the two orientations $\theta = +\pi/2$ and $-\pi/2$, as shown in Figure 3.19. We observe a clear anomalous signal for both orientations that despite being noisy appears to be robust across the different measurement occasions.

For $-\pi/2$ the shape of the anomaly is peak-and-dip while for $-\pi/2$ mostly a peak (or a dip in absolute value) is observed. The peak-and-dip shape is reminiscent of the

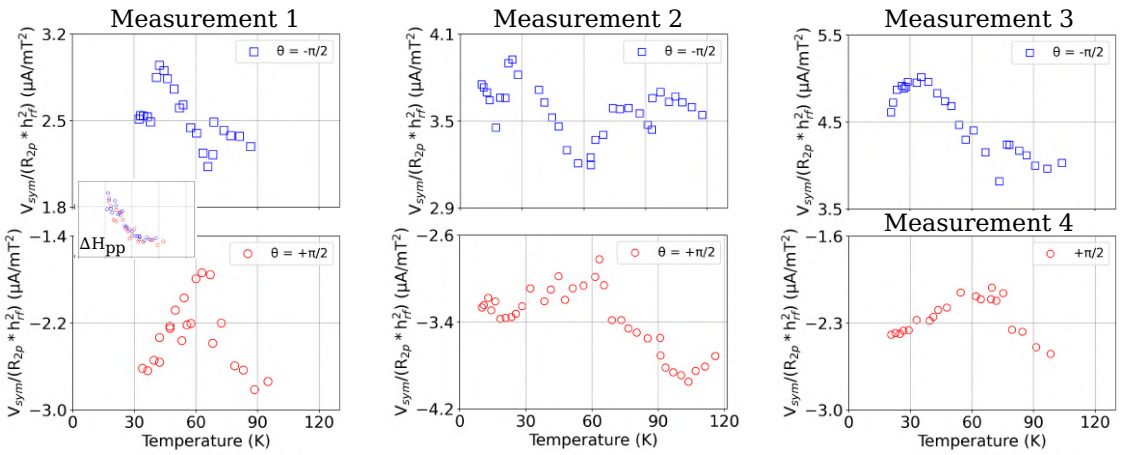

Figure 3.19: A higher-resolution temperature-dependence of V_{ISHE} around 60 K to study the anomaly that coincides with T_{irr} and T_M of $Pd_{92}Ni_8$. The anomaly is small yet robust across the different measurement occasions in terms of shape and location. Note that both $\theta = +\pi/2$ and $-\pi/2$ were measured during Measurement 1 and 2, while during Measurement 3 and 4 only one of them was measured in order to ensure identical sample conditions during the temperature scan. The inset of Measurement 1 shows the dependence of the peak-to-peak linewidth as a function of temperature, where no signature of the linear fluctuation can be observed at the critical temperatures. The temperature range of the inset is identical to that of the other plots and the y-range is 2.2-2.35 mT.

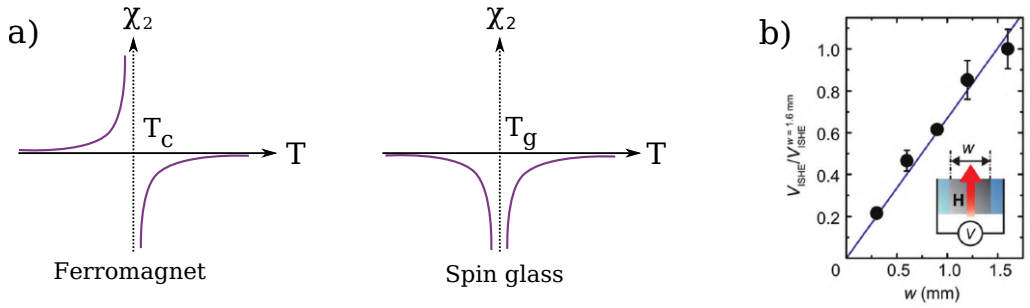

Figure 3.20: a) The different behaviors of second order spin susceptibility across a critical temperature for a ferromagnet and spin glass. Figure modified from Ref. [188]. b) The dependence of V_{ISHE} on the sample length. The linear increase implies homogeneous spin-to-charge conversion across the sample length. Figure extracted from [208].

temperature-dependence of χ_2 in ferromagnets while the peak shape is closer to that of spin glasses [188], as shown in Figure 3.20a. Coinciding with the T_{irr} and T_M, these anomalies could relate to the non-linear spin fluctuations but the meager signal-to-noise ratio renders the results preliminary and subject to further investigation. It is also interesting to note that some reports have also shown suppressed spin-to-charge conversion in CuMnBi spin glass below the critical temperature, but there the electrons scattered at the Bi sites while the Mn moments acted to dephase the spin current, reducing V_{ISHE} [209]. In PdNi, however, the Ni atoms are both the scattering site and carriers of the magnetic moment, while the heavy Pd atoms are also scatterers, so different behavior can be expected. Overall, understanding the magnetic nature of the PdNi layer would significantly aid in assigning the anomaly to the non-linear spin fluctuations as we would know from the shape of χ_2 what shape of V_{ISHE} anomaly to anticipate. This, however, is beyond the scope of this thesis so instead here we have focused on improving the signal-to-noise ratio of our sample.

Note that we do not observe a peak in ΔH_{pp} at the critical temperature as shown in Figure 3.19, which would have been a fingerprint of the linear spin fluctuations as discussed in Section 3.3.1. This is because enhancement of the spin mixing conductance is an interface effect and here the PdNi thickness is of the order of 10 nm while in Section 3.3.1 the film thicknesses were $\sim$ 1 nm. In order to simultaneously probe both the linear and non-linear fluctuations with our set-up, the samples must be very thin, but for samples that are thinner than the spin diffusion length the back-reflection of the spin current will become an issue [170]. A way to circumvent this issue would be to place a second, non-magnetic, good spin sink below the first one. Moreover, as the distance over which the spin-to-charge conversion is taking place, the conversion efficiency has to be high for the observation of a strong non-linear spin fluctuation signal.

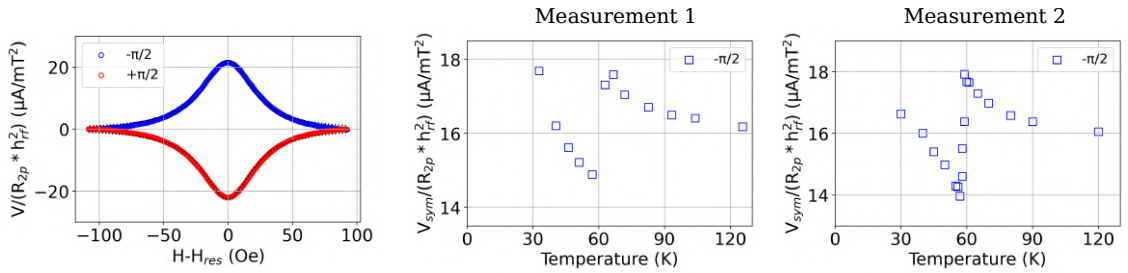

Figure 3.21: Voltage signal around the resonance field H_{res} of sample CoFeB/Cu/$Pd_{90}Ni_{10}$ for two orientations of the sample and a high-resolution temperature-dependence of V_{ISHE} around 60 K. Again, a peak-and-dip anomaly is observed but with a reversed polarity (dip-and-peak) and the anomaly occurs at a temperature coincident with neither T_{irr} nor T_M.

3.5.3 Optimization of the measurement protocol

We have taken two approaches to improving the signal-to-noise ratio. First, we have increased the length of the sample as this increases the distance over which spin-to-charge conversion can take place and therefore results in a larger V_{ISHE} as demonstrated by Ando *et al.* [208] whose results are shown in Figure 3.20b. However, we cannot increase the length infinitely as we also have to ensure a homogeneous distribution of h_{rf} across the sample length and a vanishing e_{rf}. We have found sample dimensions of 0.6x3.2 mm^2 to be a good compromise. Second, we have changed the Al spacer between the spin injector and the spin sink to a Cu spacer, which is known to have a good spin transparency. Based on Figure 3.21 it seems that the Cu spacer is indeed allowing more efficient transmission of the spin current compared to the Al spacer as the normalized V_{ISHE} has increased by a factor of ~ 5. The temperature-dependence of the V_{ISHE} in the same range and conducted with the same method of changing the temperature as the previous measurements is shown in Figure 3.21 for a sample CoFeB(15)/Cu(3)/$Pd_{90}Ni_{10}$ (10 nm). Note that here the Ni concentration is higher than before so that the expected critical temperatures are slightly higher: $T_c \sim 180$ K, $T_M \sim 110$ K, and $T_{irr} \sim 90$ K. Here we only show the measurement for the orientation $\theta = -\pi/2$. Surprisingly, we now observe a similar peak-and-dip anomaly around 60 K, but with a reversed polarity (dip-and-peak shape). This in is an unexpected result that requires further measurements in order to make more conclusive interpretation of the result. It should be noted, however, that for $Pd_{90}Ni_{10}$ the T_M or T_{irr} are more spread out from each other than for $Pd_{92}Ni_8$, which could influence the shape of the anomaly. In order to obtain more information, the temperature dependence of V_{ISHE} for the $\theta = +\pi/2$ orientation has to be measured, as well as more samples with Cu spacer and varying Ni concentration, especially $x = 8$ to have a direct comparison to the measurements with Al sample. Moreover, the anomaly does not correspond to either T_M or T_{irr}, which seems contradictory to the anomaly stemming from the non-linear spin fluctuations. However, it should be noted that in our FMR spin-pumping set-up the temperature probe is on the bottom of the cavity rather than on the sample so that the converting the

two-point resistance of the sample to temperature is an approximation rather than an exact conversion. A more exact conversion could be realized by measuring the two-point resistance on a set-up with a more local thermometer in order to see the exact temperatures at which the anomalies are occurring.

These results are preliminary and a subject of ongoing studies in the AF spintronics team at SPINTEC. Currently, complementary studies on the temperature-dependent spin-to-charge conversion in our PdNi films are being conducted in collaboration with the group of Professor Yasuhiro Niimi in the University of Osaka, where the PdNi films grown at SPINTEC are fabricated into lateral spin valve devices similar to the ones discussed in Section 3.3.2. In a more long-term, the current acquisition of a new cavity FMR-spin pumping set-up in the framework of combined PEPR SPIN/PEPR LUMA/UGA-GINP/ANR MATHEEIAS project will allow continuing this study at SPINTEC and SYMMES with an improved sensitivity and fewer experimental uncertainties (e.g. accurately determining the Q-factor of the cavity) that proved challenging with the current set-up.

3.6 Conclusions and outlook

In this Chapter we have introduced the operation principle of the cavity-based ferromagnetic resonance spin pumping set-up that is a versatile tool for studying spin transport properties of various materials. Here we have illustrated the power of this tool through a specific example of probing the effect of spin fluctuations on spin pumping and spin-to-charge conversion around critical temperatures. The main material of focus was $Pd_{100-x}Ni_x$ with varying concentrations of Ni x. We have characterized the structural, magnetic, and magnetotransport properties of the thin films and observed that they show complex magnetic behavior beyond the previously reported weak ferromagnetism. The exact nature of this magnetic phase will be a subject of further investigations. We have also showed that the spin-to-charge conversion in $Pd_{92}Ni_8$ and $Pd_{90}Ni_{10}$ shows robust, anomalous behavior at or close to some of their critical temperatures. Further experimental verifications of the reproducibility of the anomaly are currently under investigation, and combined with the future efforts on understanding the magnetic nature of the PdNi thin films could allow association of the anomaly to non-linear spin fluctuations. In addition to the preliminary results on the non-linear fluctuations, we have made significant progress in optimizing this experimental method and the sample for realizing temperature-scans with sufficiently small steps to resolve the anomalous behavior and with an improved signal-to-noise ratio.

Despite (or because of) the lack of conclusive results, this project has opened up various interesting fundamental research questions relating to the magnetic interactions prevailing in thin PdNi films and to the magnetic phase that they give rise to. Addressing these questions will necessitate further experimental characterization along with theoretical modeling. On the other hand, optimization of the measurement technique will serve

as a strong foundation for future non-linear spin fluctuation studies on both PdNi and other magnetic materials such as altermagnets and antiferromagnets that are of particular interest to the AF spintronics team.

3.7 Further research directions

- Further TEM imaging of the films with different Ni concentrations and with both side-view and top-view considered. This might aid in understanding the magnetic phase and its evolution with the Ni concentration in terms of the Ni distribution within the films.
- Atomistic simulations on PdNi films to model the different scenarios that could give rise to the complex magnetic behavior of the films. For example, the homogeneity of the Ni distribution, polarization of the Pd atoms around the Ni atoms, dipolar interactions between possible Ni clusters (or Ni-Pd 'polarization clouds'), RKKY interactions, and the strong magnetostriction could be factors worth considering.
- ac-susceptibility measurements as a function of temperature in order to identify the nature of the critical temperature signifying irreversibility in the field-cooled and zero-field cooled magnetisation measurements. The shape and frequency-dependence of any anomalies at this critical temperature could reveal whether the behavior stems from spin/cluster glass or superparamagnetic phase. This kind of measurements, however, are largely non-trivial due to the small magnetic volume of our samples, and therefore will require significant efforts in increasing the signal strength.
- Further temperature-dependent spin pumping measurements on the samples with Cu spacer. Necessary additional measurements include for example the Ni-concentration dependence of the anomaly location and shape, sample orientation dependence of the anomaly (both $\theta = \pm\pi/2$), and checking the reproducibility of the anomaly across different sample pieces.

3.8 Encore: Spin-to-charge conversion in altermagnetic materials

In this final Section we will briefly comment on the possible use of d-wave altermagnets, of which the epitaxial films of Mn_5Si_3 discussed in Chapter 1 are a candidate, as the spin sink layer where the spin-to-charge conversion takes place. Due to the alternating spin-splitting of the bands in altermagnetic materials, it has been recently proposed that they could generate a pure spin current given an appropriate alignment of the electric field relative to the crystal structure [49]. This is illustrated in Figure 3.22 for the simplified

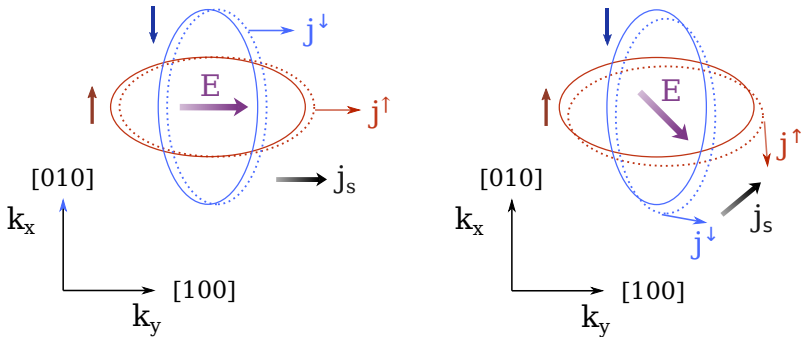

Figure 3.22: The spin-split, alternating band structure of altermagnets allows a spin-splitter phenomenon to arise where pure spin current can be generated. This effect is inherently anisotropic in terms of the orientation of the electric field relative to the crystal structure. Figure adapted from Ref. [49].

band structure of RuO_2, an altermagnet in which pure spin current generation was recently observed experimentally [50][210].

Probing the inverse of this spin splitter phenomenon could be possible in our FMR spin-pumping set-up using epitaxial Mn_5Si_3 as the spin sink layer. Growing a ferromagnetic epilayer (e.g. $Mn_5Si_3C_x$, Co) in-situ on top of the Mn_5Si_3 layer can be realized by the group of Prof. Lisa Michez and therefore appropriate samples for this kind of measurements are accessible. However, the geometry of the spin pumping measurements is such that the spin current will flow in the direction perpendicular to the spin sink film. For our current films, this direction is the crystal axis [0001], which unfortunately is a direction along which the spin-splitter phenomenon does not take place. Therefore, we would need samples with different crystal orientations, which is challenging due to the various constraints for epitaxial growth [2]. Probably a more fruitful avenue would be to seek out other altermagnets, such as RuO_2, where the crystal orientation can be controlled more easily. We have recently received RuO_2 samples from the group of Prof. Simon Moron from the University of Würzburg. FMR-spin pumping measurements on altermagnets would not only provide further experimental support for the spin-splitter phenomenon but could also be used to study various spintronic properties of altermagnets, such as critical temperatures through the spin fluctuations, spin diffusion length, anisotropy of the spin-to-charge conversion etc.

Conclusions

The current limitations of contemporary spintronic devices concern the net magnetisation of the ferromagnetic materials they typically comprise of. This limits the scalability, stability, as well as the operation speed. Overcoming these limitations has pushed the field of spintronics towards an active search for magnetic materials with vanishing net magnetisation and spintronic functionalities. This thesis is a part of this research effort.

First, we have investigated the unique and anisotropic magnetotransport properties of epitaxial Mn_5Si_3. These films exhibit both a negligible net magnetisation implying a compensated magnetic ordering along and magnetotransport effects associated with spin-splitting of the electronic band structure. The combination of these properties and their nuances in terms of anisotropy leads us to propose epitaxial Mn_5Si_3 as a candidate material of the so-called altermagnetic phase characterized by zero net magnetisation in the real space and alternating spin-splitting in the momentum space. We have also demonstrated that the emergence of the novel magnetotransport properties allows us to extend experimental techniques designed to study the static and dynamic properties of the order parameter in ferromagnets to compensated magnets.

Next, we have demonstrated the nucleation of localised, topological spin textures in antiferromagnets, which are compensated magnets with spin-degenerate bands in the momentum space. This nucleation is realized through an imprinting method where during a thermal cycling procedure topological spin textures, such as skyrmions, are transferred from a ferromagnetic layer to an antiferromagnetic layer via interfacial exchange interaction. We demonstrate the viability of this method by using atomistic simulations and subsequently study the various properties of the imprinted textures. The local symmetries (i.e. the compensated spin configuration) of the imprinted spin textures are a premise for the emergence of novel transport properties that could be of interest in future fundamental studies on topological antiferromagnetics or in designing spintronic devices where these textures serve as information carriers.

The final chapter was dedicated to discussing the ferromagnetic resonance induced spin pumping method and its utility in studying magnetisation dynamics and spin transport properties. Our interest in this method relates to its ability to probe both linear and non-linear spin susceptibilities and their evolution across magnetic phase transitions. We have previously shown that the linear susceptibility can reveal an antiferromagnetic phase transition, which is often experimentally elusive for thin films. Here we discuss how

the non-linear susceptibility acting on the spin-to-charge conversion efficiency is also expected to reveal different magnetic phase transitions through its anomalous, temperature-dependent behavior. We show preliminary results on $Pd_{100-x}Ni_x$ thin films, where we have observed a number of magnetic phase transitions of complex nature likely characterized by some degree of frustration. These results call for further investigations on the different magnetic interactions playing a role in these films and on how they give rise to the observed complex behavior. Another important outcome of this Chapter was also the optimization of the signal-to-noise ratio and resolution of the temperature-scan, which will facilitate future studies on the phase transitions in both antiferromagnetic and altermagnetic materials.

Overall, we have highlighted the unique spintronic properties of antiferromagnets and altermagnets (both belonging to the group of magnetic materials with a vanishing net magnetisation) and simultaneously introduced large toolbox of both experimental and theoretical methods for probing these properties. Ultimately, the work presented here contributes to the fundamental research that is necessary for a thorough understanding of the spintronic functionalities of compensated magnetic materials, which in turn will serve as a solid foundation for eventual development of spintronic devices where compensated magnets take the leading role.

Bibliography

[1] H. Reichlová, R. L. Seeger, R. González-Hernández, I. Kounta, R. Schlitz, D. Kriegner, P. Ritzinger, M. Lammel, M. Leiviskä, V. Petříček, P. Doležal, E. Schmoranzerová, A. Bad'ura, A. Thomas, V. Baltz, L. Michez, J. Sinova, S. T. B. Goennenwein, T. Jungwirth, and L. Šmejkal, "Macroscopic time reversal symmetry breaking by staggered spin-momentum interaction," *arXiv 2012.15651*, 2021.

[2] I. Kounta, H. Reichlová, D. Kriegner, R. Lopes Seeger, A. Bad'ura, M. Leiviskä, A. Boussadi, V. Heresanu, S. Bertaina, M. Petit, E. Schmoranzerova, L. Šmejkal, J. Sinova, T. Jungwirth, V. Baltz, S. T. B. Goennenwein, and L. Michez, "Competitive actions of MnSi in the epitaxial growth of Mn_5Si_3 thin films on Si(111)," *Phys. Rev. Mater.*, vol. 7, p. 024416, Feb 2023.

[3] M. Leiviskä, R. L. Seeger, I. Kounta, H. Reichlová, A. Bad'ura, J. Rial, S. Beckert, D. Kriegner, I. Joumard, E. Schmoranzerová, J. Sinova, T. Jungwirth, S. T. B. Goennenwein, L. Michez, L. Šmejkal, H. Gomonay, and V. Baltz, "Anisotropic anomalous Hall effect in the unconventional compensated d-wave magnet candidate Mn_5Si_3 films," *In preparation*.

[4] M. Leiviskä, S. Jenkins, R. F. L. Evans, D. Gusakova, and V. Baltz, "Dynamic imprinting of nanoscale topological phases into an antiferromagnet," *arXiv 2302.08842*, 2023.

[5] A. Hirohata, K. Yamada, Y. Nakatani, I.-L. Prejbeanu, B. Diény, P. Pirro, and B. Hillebrands, "Review on spintronics: Principles and device applications," *Journal of Magnetism and Magnetic Materials*, vol. 509, p. 166711, 2020.

[6] M. N. Baibich, J. M. Broto, A. Fert, F. N. Van Dau, F. Petroff, P. Etienne, G. Creuzet, A. Friederich, and J. Chazelas, "Giant magnetoresistance of (001) Fe/(001) Cr magnetic superlattices," *Phys. Rev. Lett.*, vol. 61, pp. 2472–2475, Nov 1988.

[7] G. Binasch, P. Grünberg, F. Saurenbach, and W. Zinn, "Enhanced magnetoresistance in layered magnetic structures with antiferromagnetic interlayer exchange," *Phys. Rev. B*, vol. 39, pp. 4828–4830, Mar 1989.

[8] M. Julliere, "Tunneling between ferromagnetic films," *Physics Letters A*, vol. 54, pp. 225–226, Sept. 1975.

[9] J. S. Moodera, L. R. Kinder, T. M. Wong, and R. Meservey, "Large magnetoresistance at room temperature in ferromagnetic thin film tunnel junctions," *Phys. Rev. Lett.*, vol. 74, pp. 3273–3276, Apr 1995.

[10] W. H. Butler, X.-G. Zhang, T. C. Schulthess, and J. M. MacLaren, "Spin-dependent tunneling conductance of Fe/MgO/Fe sandwiches," *Phys. Rev. B*, vol. 63, p. 054416, Jan 2001.

[11] J. Mathon and A. Umerski, "Theory of tunneling magnetoresistance of an epitaxial Fe/MgO/Fe(001) junction," *Phys. Rev. B*, vol. 63, p. 220403, May 2001.

[12] D. Ralph and M. Stiles, "Spin transfer torques," *Journal of Magnetism and Magnetic Materials*, vol. 320, pp. 1190–1216, Apr. 2008.

[13] S. Bhatti, R. Sbiaa, A. Hirohata, H. Ohno, S. Fukami, and S. Piramanayagam, "Spintronics based random access memory: a review," *Materials Today*, vol. 20, pp. 530–548, Nov. 2017.

[14] N. Mott, "Electrons in transition metals," *Advances in Physics*, vol. 13, pp. 325–422, July 1964.

[15] I. A. Campbell, A. Fert, and R. Pomeroy, "Evidence for two current conduction Iron," *Philosophical Magazine*, vol. 15, pp. 977–983, May 1967.

[16] P. M. Tedrow and R. Meservey, "Spin-dependent tunneling into ferromagnetic Nickel," *Phys. Rev. Lett.*, vol. 26, pp. 192–195, Jan 1971.

[17] G. Busch, M. Campagna, and H. C. Siegmann, "Spin-polarized photoelectrons from Fe, Co, and Ni," *Phys. Rev. B*, vol. 4, pp. 746–750, Aug 1971.

[18] W. Gleich, G. Regenfus, and R. Sizmann, "Spin polarization of field-emitted electrons from monocrystalline Nickel," *Phys. Rev. Lett.*, vol. 27, pp. 1066–1069, Oct 1971.

[19] P. M. Tedrow and R. Meservey, "Spin polarization of electrons tunneling from films of Fe, Co, Ni, and Gd," *Phys. Rev. B*, vol. 7, pp. 318–326, Jan 1973.

[20] R. Karplus and J. M. Luttinger, "Hall effect in ferromagnetics," *Phys. Rev.*, vol. 95, pp. 1154–1160, Sep 1954.

[21] M. Dyakonov and V. Perel, "Possibility of orienting electron spins with current," *Soviet Journal of Experimental and Theoretical Physics Letters*, vol. 13, p. 467, 05 1971.

[22] I. M. Miron, K. Garello, G. Gaudin, P.-J. Zermatten, M. V. Costache, S. Auffret, S. Bandiera, B. Rodmacq, A. Schuhl, and P. Gambardella, "Perpendicular switching of a single ferromagnetic layer induced by in-plane current injection," *Nature*, vol. 476, pp. 189–193, Aug. 2011.

[23] L. Liu, C.-F. Pai, Y. Li, H. W. Tseng, D. C. Ralph, and R. A. Buhrman, "Spin-torque switching with the giant spin Hall effect of Tantalum," *Science*, vol. 336, pp. 555–558, May 2012.

[24] Q. Shao, P. Li, L. Liu, H. Yang, S. Fukami, A. Razavi, H. Wu, K. Wang, F. Freimuth, Y. Mokrousov, M. D. Stiles, S. Emori, A. Hoffmann, J. Akerman, K. Roy, J.-P. Wang, S.-H. Yang, K. Garello, and W. Zhang, "Roadmap of spin–orbit torques," *IEEE Transactions on Magnetics*, vol. 57, pp. 1–39, July 2021.

[25] L. Néel, "Antiferromagnetism and ferrimagnetism," *Proceedings of the Physical Society. Section A*, vol. 65, pp. 869–885, Nov. 1952.

[26] C. G. Shull, W. A. Strauser, and E. O. Wollan, "Neutron diffraction by paramagnetic and antiferromagnetic substances," *Phys. Rev.*, vol. 83, pp. 333–345, Jul 1951.

[27] J. Nogués and I. K. Schuller, "Exchange bias," *Journal of Magnetism and Magnetic Materials*, vol. 192, pp. 203–232, Feb. 1999.

[28] T. Jungwirth, X. Marti, P. Wadley, and J. Wunderlich, "Antiferromagnetic spintronics," *Nature Nanotechnology*, vol. 11, pp. 231–241, Mar. 2016.

[29] V. Baltz, A. Manchon, M. Tsoi, T. Moriyama, T. Ono, and Y. Tserkovnyak, "Antiferromagnetic spintronics," *Rev. Mod. Phys.*, vol. 90, p. 015005, Feb 2018.

[30] J. Železný, H. Gao, K. Výborný, J. Zemen, J. Mašek, A. Manchon, J. Wunderlich, J. Sinova, and T. Jungwirth, "Relativistic Néel-order fields induced by electrical current in antiferromagnets," *Phys. Rev. Lett.*, vol. 113, p. 157201, Oct 2014.

[31] P. Wadley, B. Howells, J. Železný, C. Andrews, V. Hills, R. P. Campion, V. Novák, K. Olejník, F. Maccherozzi, S. S. Dhesi, S. Y. Martin, T. Wagner, J. Wunderlich, F. Freimuth, Y. Mokrousov, J. Kuneš, J. S. Chauhan, M. J. Grzybowski, A. W. Rushforth, K. W. Edmonds, B. L. Gallagher, and T. Jungwirth, "Electrical switching of an antiferromagnet," *Science*, vol. 351, pp. 587–590, Feb. 2016.

[32] X. Marti, I. Fina, C. Frontera, J. Liu, P. Wadley, Q. He, R. J. Paull, J. D. Clarkson, J. Kudrnovský, I. Turek, J. Kuneš, D. Yi, J.-H. Chu, C. T. Nelson, L. You, E. Arenholz, S. Salahuddin, J. Fontcuberta, T. Jungwirth, and R. Ramesh, "Room-temperature antiferromagnetic memory resistor," *Nature Materials*, vol. 13, pp. 367–374, Jan. 2014.

[33] A. V. Kimel, A. Kirilyuk, A. Tsvetkov, R. V. Pisarev, and T. Rasing, "Laser-induced ultrafast spin reorientation in the antiferromagnet $TmFeO_3$," *Nature*, vol. 429, pp. 850–853, June 2004.

[34] N. P. Duong, T. Satoh, and M. Fiebig, "Ultrafast manipulation of antiferromagnetism of NiO," *Phys. Rev. Lett.*, vol. 93, p. 117402, Sep 2004.

[35] H. Yan, Z. Feng, S. Shang, X. Wang, Z. Hu, J. Wang, Z. Zhu, H. Wang, Z. Chen, H. Hua, W. Lu, J. Wang, P. Qin, H. Guo, X. Zhou, Z. Leng, Z. Liu, C. Jiang, M. Coey, and Z. Liu, "A piezoelectric, strain-controlled antiferromagnetic memory insensitive to magnetic fields," *Nature Nanotechnology*, vol. 14, pp. 131–136, Jan. 2019.

[36] H. Chen, Q. Niu, and A. H. MacDonald, "Anomalous Hall effect arising from noncollinear antiferromagnetism," *Phys. Rev. Lett.*, vol. 112, p. 017205, Jan 2014.

[37] S. Hayami, Y. Yanagi, and H. Kusunose, "Momentum-dependent spin splitting by collinear antiferromagnetic ordering," *Journal of the Physical Society of Japan*, vol. 88, p. 123702, Dec. 2019.

[38] L.-D. Yuan, Z. Wang, J.-W. Luo, and A. Zunger, "Prediction of low-z collinear and noncollinear antiferromagnetic compounds having momentum-dependent spin splitting even without spin-orbit coupling," *Phys. Rev. Mater.*, vol. 5, p. 014409, Jan 2021.

[39] L. Šmejkal, J. Sinova, and T. Jungwirth, "Beyond conventional ferromagnetism and antiferromagnetism: A phase with nonrelativistic spin and crystal rotation symmetry," *Phys. Rev. X*, vol. 12, p. 031042, Sep 2022.

[40] J. Kübler and C. Felser, "Non-collinear antiferromagnets and the anomalous Hall effect," *EPL (Europhysics Letters)*, vol. 108, p. 67001, Dec. 2014.

[41] S. Nakatsuji, N. Kiyohara, and T. Higo, "Large anomalous Hall effect in a non-collinear antiferromagnet at room temperature," *Nature*, vol. 527, pp. 212–215, Oct. 2015.

[42] L. Šmejkal, R. González-Hernández, T. Jungwirth, and J. Sinova, "Crystal time-reversal symmetry breaking and spontaneous hall effect in collinear antiferromagnets," *Science Advances*, vol. 6, no. 23, p. eaaz8809, 2020.

[43] Z. Feng, X. Zhou, L. Šmejkal, L. Wu, Z. Zhu, H. Guo, R. González-Hernández, X. Wang, H. Yan, P. Qin, X. Zhang, H. Wu, H. Chen, Z. Meng, L. Liu, Z. Xia, J. Sinova, T. Jungwirth, and Z. Liu, "An anomalous Hall effect in altermagnetic Ruthenium Dioxide," *Nature Electronics*, vol. 5, pp. 735–743, Nov. 2022.

[44] L. Šmejkal, A. B. Hellenes, R. González-Hernández, J. Sinova, and T. Jungwirth, "Giant and tunneling magnetoresistance in unconventional collinear antiferromagnets with nonrelativistic spin-momentum coupling," *Phys. Rev. X*, vol. 12, p. 011028, Feb 2022.

[45] J. Dong, X. Li, G. Gurung, M. Zhu, P. Zhang, F. Zheng, E. Y. Tsymbal, and J. Zhang, "Tunneling magnetoresistance in noncollinear antiferromagnetic tunnel junctions," *Phys. Rev. Lett.*, vol. 128, p. 197201, May 2022.

[46] X. Chen, T. Higo, K. Tanaka, T. Nomoto, H. Tsai, H. Idzuchi, M. Shiga, S. Sakamoto, R. Ando, H. Kosaki, T. Matsuo, D. Nishio-Hamane, R. Arita, S. Miwa, and S. Nakatsuji, "Octupole-driven magnetoresistance in an antiferromagnetic tunnel junction," *Nature*, vol. 613, pp. 490–495, Jan. 2023.

[47] P. Qin, H. Yan, X. Wang, H. Chen, Z. Meng, J. Dong, M. Zhu, J. Cai, Z. Feng, X. Zhou, L. Liu, T. Zhang, Z. Zeng, J. Zhang, C. Jiang, and Z. Liu, "Room-temperature magnetoresistance in an all-antiferromagnetic tunnel junction," *Nature*, vol. 613, pp. 485–489, Jan. 2023.

[48] J. Železný, Y. Zhang, C. Felser, and B. Yan, "Spin-polarized current in noncollinear antiferromagnets," *Phys. Rev. Lett.*, vol. 119, p. 187204, Nov 2017.

[49] R. González-Hernández, L. Šmejkal, K. Výborný, Y. Yahagi, J. Sinova, T. c. v. Jungwirth, and J. Železný, "Efficient electrical spin splitter based on nonrelativistic collinear antiferromagnetism," *Phys. Rev. Lett.*, vol. 126, p. 127701, Mar 2021.

[50] A. Bose, N. J. Schreiber, R. Jain, D.-F. Shao, H. P. Nair, J. Sun, X. S. Zhang, D. A. Muller, E. Y. Tsymbal, D. G. Schlom, and D. C. Ralph, "Tilted spin current generated by the collinear antiferromagnet Ruthenium Dioxide," *Nature Electronics*, vol. 5, pp. 267–274, May 2022.

[51] L. Šmejkal, A. Marmodoro, K.-H. Ahn, R. Gonzalez-Hernandez, I. Turek, S. Mankovsky, H. Ebert, S. W. D'Souza, O. Šipr, J. Sinova, and T. Jungwirth, "Chiral magnons in altermagnetic RuO_2," *arXiv 2211.13806*, 2022.

[52] K.-R. Jeon, B. K. Hazra, K. Cho, A. Chakraborty, J.-C. Jeon, H. Han, H. L. Meyerheim, T. Kontos, and S. S. P. Parkin, "Long-range supercurrents through a chiral non-collinear antiferromagnet in lateral Josephson junctions," *Nature Materials*, vol. 20, pp. 1358–1363, Aug. 2021.

[53] R. L. Seeger, *Exploring novel spin and charge transport mechanisms in ferromagnetic and antiferromagnetic spin structures and spin textures*. PhD thesis, University of Grenoble Alpes, 2021.

[54] R. Birss, *Symmetry and Magnetism*. North-Holland Publishing Company, 1964.

[55] C. Malgrange, C. Ricolleau, and M. Schlenker, *Symmetry and Physical Properties of Crystals*. Springer Netherlands, 2014.

[56] A. V. Shubnikov and N. V. Belov, *Colored symmetry*. Macmillan, 1964.

[57] C. J. BRADLEY and B. L. DAVIES, "Magnetic groups and their corepresentations," *Rev. Mod. Phys.*, vol. 40, pp. 359–379, Apr 1968.

[58] W. F. Brinkman and R. J. Elliott, "Theory of spin-space groups," *Proceedings of the Royal Society of London. Series A. Mathematical and Physical Sciences*, vol. 294, pp. 343 – 358, 1966.

[59] P. Liu, J. Li, J. Han, X. Wan, and Q. Liu, "Spin-group symmetry in magnetic materials with negligible spin-orbit coupling," *Phys. Rev. X*, vol. 12, p. 021016, Apr 2022.

[60] M. Naka, S. Hayami, H. Kusunose, Y. Yanagi, Y. Motome, and H. Seo, "Spin current generation in organic antiferromagnets," *Nature Communications*, vol. 10, p. 4305, Sept. 2019.

[61] R. D. Gonzalez Betancourt, J. Zubáč, R. Gonzalez-Hernandez, K. Geishendorf, Z. Šobáň, G. Springholz, K. Olejník, L. Šmejkal, J. Sinova, T. Jungwirth, S. T. B. Goennenwein, A. Thomas, H. Reichlová, J. Železný, and D. Kriegner, "Spontaneous anomalous Hall effect arising from an unconventional compensated magnetic phase in a semiconductor," *Phys. Rev. Lett.*, vol. 130, p. 036702, Jan 2023.

[62] T. Jungwirth, "Online SPICE-SPIN+X seminar: Altermagnetism - an emerging basic magnetic phase."

[63] H. Reichlová, "Online SPICE-SPIN+X seminar: Spontaneous anomalous Hall response and altermagnetism explored in MnTe and Mn_5Si_3."

[64] L. Šmejkal, A. H. MacDonald, J. Sinova, S. Nakatsuji, and T. Jungwirth, "Anomalous Hall antiferromagnets," *Nature Reviews Materials*, vol. 7, pp. 482–496, Mar. 2022.

[65] N. Nagaosa, J. Sinova, S. Onoda, A. H. MacDonald, and N. P. Ong, "Anomalous Hall effect," *Rev. Mod. Phys.*, vol. 82, pp. 1539–1592, May 2010.

[66] A. K. Nayak, J. E. Fischer, Y. Sun, B. Yan, J. Karel, A. C. Komarek, C. Shekhar, N. Kumar, W. Schnelle, J. Kübler, C. Felser, and S. S. P. Parkin, "Large anomalous Hall effect driven by a nonvanishing berry curvature in the noncollinear antiferromagnet Mn_3Ge," *Science Advances*, vol. 2, p. e1501870, Apr. 2016.

[67] M. Berry, "Quantal phase factors accompanying adiabatic changes," *Proceedings of the Royal Society of London. A. Mathematical and Physical Sciences*, vol. 392, pp. 45–57, Mar. 1984.

[68] G. H. Lander, P. J. Brown, and J. B. Forsyth, "The antiferromagnetic structure of Mn_5Si_3," *Proceedings of the Physical Society*, vol. 91, pp. 332–340, June 1967.

[69] A. Z. Menshikov, A. P. Vokhmyanin, and Y. A. Dorofeev, "Magnetic structure and phase transformations in Mn_5Si_3," *physica status solidi (b)*, vol. 158, pp. 319–328, Mar. 1990.

[70] P. J. Brown, J. B. Forsyth, V. Nunez, and F. Tasset, "The low-temperature antiferromagnetic structure of Mn_5Si_3 revised in the light of neutron polarimetry," *Journal of Physics: Condensed Matter*, vol. 4, pp. 10025–10036, Dec. 1992.

[71] P. J. Brown and J. B. Forsyth, "Antiferromagnetism in Mn_5Si_3: the magnetic structure of the AF2 phase at 70 K," *Journal of Physics: Condensed Matter*, vol. 7, pp. 7619–7628, Sept. 1995.

[72] F. J. dos Santos, N. Biniskos, S. Raymond, K. Schmalzl, M. dos Santos Dias, P. Steffens, J. Persson, S. Blügel, S. Lounis, and T. Brückel, "Spin waves in the collinear antiferromagnetic phase of Mn_5Si_3," *Phys. Rev. B*, vol. 103, p. 024407, Jan 2021.

[73] N. Biniskos, F. J. dos Santos, K. Schmalzl, S. Raymond, M. dos Santos Dias, J. Persson, N. Marzari, S. Blügel, S. Lounis, and T. Brückel, "Complex magnetic structure and spin waves of the noncollinear antiferromagnet Mn_5Si_3," *Phys. Rev. B*, vol. 105, p. 104404, Mar 2022.

[74] M. Gottschilch, O. Gourdon, J. Persson, C. de la Cruz, V. Petricek, and T. Brueckel, "Study of the antiferromagnetism of Mn_5Si_3: an inverse magnetocaloric effect material," *Journal of Materials Chemistry*, vol. 22, no. 30, p. 15275, 2012.

[75] B. Aronsson, D. H. Templeton, S. Rundqvist, E. Varde, and G. Westin, "A note on the compositions and crystal structures of MnB_2, Mn_3Si, Mn_5Si_3, and $FeSi_2$.," *Acta Chemica Scandinavica*, vol. 14, pp. 1414–1418, 1960.

[76] H. Wada, H. Nakamura, K. Yoshimura, M. Shiga, and Y. Nakamura, "Stability of Mn moments and spin fluctuations in RMn_2 (R: Rare earth)," *Journal of Magnetism and Magnetic Materials*, vol. 70, pp. 134–136, Dec. 1987.

[77] J. B. Forsyth and P. J. Brown, "The spatial distribution of magnetisation density in Mn_5Si_3," *Journal of Physics: Condensed Matter*, vol. 2, pp. 2713–2720, Mar. 1990.

[78] C. Sürgers, T. Wolf, P. Adelmann, W. Kittler, G. Fischer, and H. v. Löhneysen, "Switching of a large anomalous Hall effect between metamagnetic phases of a non-collinear antiferromagnet," *Scientific Reports*, vol. 7, p. 42982, Feb. 2017.

[79] C. Sürgers, G. Fischer, P. Winkel, and H. v. Löhneysen, "Large topological Hall effect in the non-collinear phase of an antiferromagnet," *Nature Communications*, vol. 5, p. 3400, Mar. 2014.

[80] Z. Istomina, L. Andreeva, S. Zadvorkin, and A. Andreev, "Fizicheskie svoistva metallov i splavov, izd," *Ural Polytechnic Institute, Sverdlovsk*, p. 13, 1983.

[81] B. A. Joyce, "Molecular beam epitaxy," *Reports on Progress in Physics*, vol. 48, pp. 1637–1697, Dec. 1985.

[82] E. Karhu, S. Kahwaji, T. L. Monchesky, C. Parsons, M. D. Robertson, and C. Maunders, "Structure and magnetic properties of MnSi epitaxial thin films," *Phys. Rev. B*, vol. 82, p. 184417, Nov 2010.

[83] M. A. Garcia, E. F. Pinel, J. de la Venta, A. Quesada, V. Bouzas, J. F. Fernández, J. J. Romero, M. S. M. González, and J. L. Costa-Krämer, "Sources of experimental errors in the observation of nanoscale magnetism," *Journal of Applied Physics*, vol. 105, p. 013925, Jan. 2009.

[84] R. Haug, G. Kappel, and A. Jaéglé, "Electrical resistivity studies of the system Mn_5Ge_3-Mn_5Si_3," *Physica Status Solidi (a)*, vol. 55, pp. 285–290, Sept. 1979.

[85] C. Sürgers, W. Kittler, T. Wolf, and H. v. Löhneysen, "Anomalous Hall effect in the noncollinear antiferromagnet Mn_5Si_3," *AIP Advances*, vol. 6, p. 055604, May 2016.

[86] A. Badura, D. Kriegner, E. Schmoranzerov, K. Výborný, M. Leiviskä, R. L. Seeger, V. Baltz, D. Scheffler, I. Kounta, L. Michez, L. Šmejkal, J. Sinova, S. T. B. Goennenwein, J. Zelezný, and H. Reichlová, "Even-in-magnetic-field part of transverse resistivity as a quantitative probe of magnetic order: application to Mn_5Si_3 thin films," *In preparation*.

[87] A. Gerber, "Interpretation of experimental evidence of the topological Hall effect," *Phys. Rev. B*, vol. 98, p. 214440, Dec 2018.

[88] E. Roman, Y. Mokrousov, and I. Souza, "Orientation dependence of the intrinsic anomalous Hall effect in hcp Cobalt," *Phys. Rev. Lett.*, vol. 103, p. 097203, Aug 2009.

[89] A. Bogdanov and D. Yablonskii, "Thermodynamically stable vortices in magnetically ordered crystals. The mixed state of magnets," *Soviet Journal of Experimental and Theoretical Physics*, vol. 68, p. 101, Jan. 1989.

[90] A. V. Kimel, B. A. Ivanov, R. V. Pisarev, P. A. Usachev, A. Kirilyuk, and T. Rasing, "Inertia-driven spin switching in antiferromagnets," *Nature Physics*, vol. 5, pp. 727–731, Aug. 2009.

[91] M. J. Grzybowski, P. Wadley, K. W. Edmonds, R. Beardsley, V. Hills, R. P. Campion, B. L. Gallagher, J. S. Chauhan, V. Novak, T. Jungwirth, F. Maccherozzi, and S. S. Dhesi, "Imaging current-induced switching of antiferromagnetic domains in CuMnAs," *Phys. Rev. Lett.*, vol. 118, p. 057701, Jan 2017.

[92] X. F. Zhou, J. Zhang, F. Li, X. Z. Chen, G. Y. Shi, Y. Z. Tan, Y. D. Gu, M. S. Saleem, H. Q. Wu, F. Pan, and C. Song, "Strong orientation-dependent spin-orbit torque in thin films of the antiferromagnet Mn_2Au," *Phys. Rev. Appl.*, vol. 9, p. 054028, May 2018.

[93] S. Y. Bodnar, L. Šmejkal, I. Turek, T. Jungwirth, O. Gomonay, J. Sinova, A. A. Sapozhnik, H.-J. Elmers, M. Kläui, and M. Jourdan, "Writing and reading antiferromagnetic Mn_2Au by Néel spin-orbit torques and large anisotropic magnetoresistance," *Nature Communications*, vol. 9, p. 348, Jan. 2018.

[94] X. Z. Chen, R. Zarzuela, J. Zhang, C. Song, X. F. Zhou, G. Y. Shi, F. Li, H. A. Zhou, W. J. Jiang, F. Pan, and Y. Tserkovnyak, "Antidamping-torque-induced switching in biaxial antiferromagnetic insulators," *Phys. Rev. Lett.*, vol. 120, p. 207204, May 2018.

[95] A. N. Bazhan and C. Bazan, "Weak ferromagnetism in CoF_2 and NiF_2," *Zh. Eksp. Teor. Fiz.*, pp. 898–904, 1975.

[96] R. S. Lee and S. Legvold, "Hall effect of Gadolinium, Lutetium, and Yttrium single crystals," *Phys. Rev.*, vol. 162, pp. 431–435, Oct 1967.

[97] A. Hirsch and Y. Weissman, "Anisotropy of the Hall effect in Iron," *Physics Letters A*, vol. 44, pp. 239–240, June 1973.

[98] L. Šmejkal, J. Železný, J. Sinova, and T. Jungwirth, "Electric control of Dirac quasiparticles by spin-orbit torque in an antiferromagnet," *Phys. Rev. Lett.*, vol. 118, p. 106402, Mar 2017.

[99] P. K. Rout, I. Agireen, E. Maniv, M. Goldstein, and Y. Dagan, "Six-fold crystalline anisotropic magnetoresistance in the (111) $LaAlO_3/SrTiO_3$ oxide interface," *Phys. Rev. B*, vol. 95, p. 241107, Jun 2017.

[100] D. Kriegner, H. Reichlová, J. Grenzer, W. Schmidt, E. Ressouche, J. Godinho, T. Wagner, S. Y. Martin, A. B. Shick, V. V. Volobuev, G. Springholz, V. Holý, J. Wunderlich, T. Jungwirth, and K. Výborný, "Magnetic anisotropy in antiferromagnetic hexagonal MnTe," *Phys. Rev. B*, vol. 96, p. 214418, Dec 2017.

[101] C. S. King, *Magnetotransport and magnetocrystalline anisotropy studies of Gallium Manganese Arsenide thin films*. PhD thesis, University of Nottingham, 2008.

[102] D. V. Nomokonov, A. V. Goran, and A. A. Bykov, "Anisotropic Corbino conductivity in a magnetic field," *Journal of Applied Physics*, vol. 125, p. 164301, Apr. 2019.

[103] A. W. Rushforth, K. Výborný, C. S. King, K. W. Edmonds, R. P. Campion, C. T. Foxon, J. Wunderlich, A. C. Irvine, P. Vašek, V. Novák, K. Olejník, J. Sinova, T. Jungwirth, and B. L. Gallagher, "Anisotropic magnetoresistance components in (Ga,Mn)As," *Phys. Rev. Lett.*, vol. 99, p. 147207, Oct 2007.

[104] X. M. Cheng, V. I. Nikitenko, A. J. Shapiro, R. D. Shull, and C. L. Chien, "Unusual magnetization reversal in $[Co/Pt]_4$ multilayers with perpendicular anisotropy," *Journal of Applied Physics*, vol. 99, p. 08C905, Apr. 2006.

[105] A. Berger, S. Mangin, J. McCord, O. Hellwig, and E. E. Fullerton, "Cumulative minor loop growth in Co/Pt and Co/Pd multilayers," *Phys. Rev. B*, vol. 82, p. 104423, Sep 2010.

[106] D.-T. Quach, D.-T. Pham, D.-T. Ngo, T.-L. Phan, S.-Y. Park, S.-H. Lee, and D.-H. Kim, "Minor hysteresis patterns with a rounded/sharpened reversing behavior in ferromagnetic multilayer," *Scientific Reports*, vol. 8, Mar. 2018.

[107] S.-W. Cheong, M. Fiebig, W. Wu, L. Chapon, and V. Kiryukhin, "Seeing is believing: visualization of antiferromagnetic domains," *npj Quantum Materials*, vol. 5, p. 3, Jan. 2020.

[108] D. Kan, T. Moriyama, and Y. Shimakawa, "Field-sweep-rate and time dependence of transverse resistivity anomalies in ultrathin $SrRuo_3$ films," *Phys. Rev. B*, vol. 101, p. 014448, Jan 2020.

[109] Q. Peng and H. Richter, "Field sweep rate dependence of media dynamic coercivity," *IEEE Transactions on Magnetics*, vol. 40, pp. 2446–2448, July 2004.

[110] D. Dickson, N. Reid, C. Hunt, H. Williams, M. El-Hilo, and K. O'Grady, "Determination of f_0 for fine magnetic particles," *Journal of Magnetism and Magnetic Materials*, vol. 125, pp. 345–350, Aug. 1993.

[111] G. Vallejo-Fernandez, N. P. Aley, J. N. Chapman, and K. O'Grady, "Measurement of the attempt frequency in antiferromagnets," *Applied Physics Letters*, vol. 97, p. 222505, Nov. 2010.

[112] C. Tannous and J. Gieraltowski, "The Stoner-Wohlfarth model of ferromagnetism," *European Journal of Physics*, vol. 29, pp. 475–487, Mar. 2008.

[113] N. Caçoilo, S. Lequeux, B. Teixeira, B. Dieny, R. Sousa, N. Sobolev, O. Fruchart, I. Prejbeanu, and L. Buda-Prejbeanu, "Spin-torque-triggered magnetization reversal in magnetic tunnel junctions with perpendicular shape anisotropy," *Phys. Rev. Appl.*, vol. 16, p. 024020, Aug 2021.

[114] R. L. Seeger, G. Forestier, O. Gladii, M. Leiviskä, S. Auffret, I. Joumard, C. Gomez, M. Rubio-Roy, A. I. Buzdin, M. Houzet, and V. Baltz, "Penetration depth of Cooper pairs in the IrMn antiferromagnet," *Phys. Rev. B*, vol. 104, p. 054413, Aug 2021.

[115] H.-B. Braun, "Solitons in real space: Domain walls, vortices, hedgehogs, and skyrmions," in *Springer Series in Solid-State Sciences*, pp. 1–40, Springer International Publishing, 2018.

[116] B. Göbel, I. Mertig, and O. A. Tretiakov, "Beyond skyrmions: Review and perspectives of alternative magnetic quasiparticles," *Physics Reports*, vol. 895, pp. 1–28, Feb. 2021.

[117] S. S. P. Parkin, M. Hayashi, and L. Thomas, "Magnetic domain-wall racetrack memory," *Science*, vol. 320, pp. 190–194, Apr. 2008.

[118] A. Fert, N. Reyren, and V. Cros, "Magnetic skyrmions: advances in physics and potential applications," *Nature Reviews Materials*, vol. 2, p. 17031, June 2017.

[119] M. Hoffmann, B. Zimmermann, G. P. Müller, D. Schürhoff, N. S. Kiselev, C. Melcher, and S. Blügel, "Antiskyrmions stabilized at interfaces by anisotropic Dzyaloshinskii-Moriya interactions," *Nature Communications*, vol. 8, p. 308, Aug. 2017.

[120] L. Shen, J. Xia, G. Zhao, X. Zhang, M. Ezawa, O. A. Tretiakov, X. Liu, and Y. Zhou, "Dynamics of the antiferromagnetic skyrmion induced by a magnetic anisotropy gradient," *Phys. Rev. B*, vol. 98, p. 134448, Oct 2018.

[121] A. Bogdanov and A. Hubert, "The properties of isolated magnetic vortices," *physica status solidi (b)*, vol. 186, pp. 527–543, Dec. 1994.

[122] I. Dzyaloshinsky, "A thermodynamic theory of weak ferromagnetism of antiferromagnetics," *Journal of Physics and Chemistry of Solids*, vol. 4, pp. 241–255, Jan. 1958.

[123] T. Moriya, "Anisotropic superexchange interaction and weak ferromagnetism," *Phys. Rev.*, vol. 120, pp. 91–98, Oct 1960.

[124] H. Yang, A. Thiaville, S. Rohart, A. Fert, and M. Chshiev, "Anatomy of Dzyaloshinskii-Moriya interaction at Co/Pt interfaces," *Phys. Rev. Lett.*, vol. 115, p. 267210, Dec 2015.

[125] S. Emori, E. Martinez, K.-J. Lee, H.-W. Lee, U. Bauer, S.-M. Ahn, P. Agrawal, D. C. Bono, and G. S. D. Beach, "Spin Hall torque magnetometry of Dzyaloshinskii domain walls," *Phys. Rev. B*, vol. 90, p. 184427, Nov 2014.

[126] S. Pizzini, J. Vogel, S. Rohart, L. D. Buda-Prejbeanu, E. Jué, O. Boulle, I. M. Miron, C. K. Safeer, S. Auffret, G. Gaudin, and A. Thiaville, "Chirality-induced asymmetric magnetic nucleation in Pt/Co/AlOx ultrathin microstructures," *Phys. Rev. Lett.*, vol. 113, p. 047203, Jul 2014.

[127] M. Belmeguenai, J.-P. Adam, Y. Roussigné, S. Eimer, T. Devolder, J.-V. Kim, S. M. Cherif, A. Stashkevich, and A. Thiaville, "Interfacial Dzyaloshinskii-Moriya interaction in perpendicularly magnetized Pt/Co/Alo$_x$ ultrathin films measured by Brillouin light spectroscopy," *Phys. Rev. B*, vol. 91, p. 180405, May 2015.

[128] K. Everschor-Sitte and M. Sitte, "Real-space Berry phases: Skyrmion soccer (invited)," *Journal of Applied Physics*, vol. 115, p. 172602, May 2014.

[129] P. Bruno, V. K. Dugaev, and M. Taillefumier, "Topological Hall effect and Berry phase in magnetic nanostructures," *Phys. Rev. Lett.*, vol. 93, p. 096806, Aug 2004.

[130] G. Chen, "Skyrmion Hall effect," *Nature Physics*, vol. 13, pp. 112–113, Jan. 2017.

[131] B. Göbel, A. Mook, J. Henk, and I. Mertig, "Overcoming the speed limit in skyrmion racetrack devices by suppressing the skyrmion Hall effect," *Phys. Rev. B*, vol. 99, p. 020405, Jan 2019.

[132] T. Dohi, S. DuttaGupta, S. Fukami, and H. Ohno, "Formation and current-induced motion of synthetic antiferromagnetic skyrmion bubbles," *Nature Communications*, vol. 10, p. 5153, Nov. 2019.

[133] W. Legrand, D. Maccariello, F. Ajejas, S. Collin, A. Vecchiola, K. Bouzehouane, N. Reyren, V. Cros, and A. Fert, "Room-temperature stabilization of antiferromagnetic skyrmions in synthetic antiferromagnets," *Nature Materials*, vol. 19, pp. 34–42, Sept. 2019.

[134] R. Juge, N. Sisodia, J. U. Larrañaga, Q. Zhang, V. T. Pham, K. G. Rana, B. Sarpi, N. Mille, S. Stanescu, R. Belkhou, M.-A. Mawass, N. Novakovic-Marinkovic, F. Kronast, M. Weigand, J. Gräfe, S. Wintz, S. Finizio, J. Raabe, L. Aballe, M. Foerster, M. Belmeguenai, L. D. Buda-Prejbeanu, J. Pelloux-Prayer, J. M. Shaw, H. T. Nembach, L. Ranno, G. Gaudin, and O. Boulle, "Skyrmions in synthetic antiferromagnets and their nucleation via electrical current and ultra-fast laser illumination," *Nature Communications*, vol. 13, p. 4807, Aug. 2022.

[135] W. Jiang, X. Zhang, G. Yu, W. Zhang, X. Wang, M. B. Jungfleisch, J. E. Pearson, X. Cheng, O. Heinonen, K. L. Wang, Y. Zhou, A. Hoffmann, and S. G. E. te Velthuis, "Direct observation of the skyrmion Hall effect," *Nature Physics*, vol. 13, pp. 162–169, Sept. 2016.

[136] M. B. Jungfleisch, W. Zhang, and A. Hoffmann, "Perspectives of antiferromagnetic spintronics," *Physics Letters A*, vol. 382, pp. 865–871, Apr. 2018.

[137] X. Zhang, Y. Zhou, and M. Ezawa, "Antiferromagnetic skyrmion: Stability, creation and manipulation," *Scientific Reports*, vol. 6, p. 24795, Apr. 2016.

[138] J. Barker and O. A. Tretiakov, "Static and dynamical properties of antiferromagnetic skyrmions in the presence of applied current and temperature," *Phys. Rev. Lett.*, vol. 116, p. 147203, Apr 2016.

[139] P. M. Buhl, F. Freimuth, S. Blügel, and Y. Mokrousov, "Topological spin Hall effect in antiferromagnetic skyrmions," *physica status solidi (RRL) - Rapid Research Letters*, vol. 11, p. 1700007, Feb. 2017.

[140] C. A. Akosa, O. A. Tretiakov, G. Tatara, and A. Manchon, "Theory of the topological spin Hall effect in antiferromagnetic skyrmions: Impact on current-induced motion," *Phys. Rev. Lett.*, vol. 121, p. 097204, Aug 2018.

[141] S. Mühlbauer, B. Binz, F. Jonietz, C. Pfleiderer, A. Rosch, A. Neubauer, R. Georgii, and P. Böni, "Skyrmion lattice in a chiral magnet," *Science*, vol. 323, pp. 915–919, Feb. 2009.

[142] W. Münzer, A. Neubauer, T. Adams, S. Mühlbauer, C. Franz, F. Jonietz, R. Georgii, P. Böni, B. Pedersen, M. Schmidt, A. Rosch, and C. Pfleiderer, "Skyrmion lattice in the doped semiconductor $Fe_{1-x}Co_xSi$," *Phys. Rev. B*, vol. 81, p. 041203, Jan 2010.

[143] N. Romming, C. Hanneken, M. Menzel, J. E. Bickel, B. Wolter, K. von Bergmann, A. Kubetzka, and R. Wiesendanger, "Writing and deleting single magnetic skyrmions," *Science*, vol. 341, pp. 636–639, Aug. 2013.

[144] W. Jiang, P. Upadhyaya, W. Zhang, G. Yu, M. B. Jungfleisch, F. Y. Fradin, J. E. Pearson, Y. Tserkovnyak, K. L. Wang, O. Heinonen, S. G. E. te Velthuis, and A. Hoffmann, "Blowing magnetic skyrmion bubbles," *Science*, vol. 349, pp. 283–286, July 2015.

[145] R. Khoshlahni, A. Qaiumzadeh, A. Bergman, and A. Brataas, "Ultrafast generation and dynamics of isolated skyrmions in antiferromagnetic insulators," *Phys. Rev. B*, vol. 99, p. 054423, Feb 2019.

[146] S. Gao, H. D. Rosales, F. A. G. Albarracín, V. Tsurkan, G. Kaur, T. Fennell, P. Steffens, M. Boehm, P. Čermák, A. Schneidewind, E. Ressouche, D. C. Cabra, C. Rüegg, and O. Zaharko, "Fractional antiferromagnetic skyrmion lattice induced by anisotropic couplings," *Nature*, vol. 586, pp. 37–41, Sept. 2020.

[147] H. Jani, J.-C. Lin, J. Chen, J. Harrison, F. Maccherozzi, J. Schad, S. Prakash, C.-B. Eom, A. Ariando, T. Venkatesan, and P. G. Radaelli, "Antiferromagnetic half-skyrmions and bimerons at room temperature," *Nature*, vol. 590, pp. 74–79, Feb. 2021.

[148] R. F. L. Evans, W. J. Fan, P. Chureemart, T. A. Ostler, M. O. A. Ellis, and R. W. Chantrell, "Atomistic spin model simulations of magnetic nanomaterials," *Journal of Physics: Condensed Matter*, vol. 26, p. 103202, Feb. 2014.

[149] S. Jenkins, W. J. Fan, R. Gaina, R. W. Chantrell, T. Klemmer, and R. F. L. Evans, "Atomistic origin of exchange anisotropy in noncollinear $IrMn_3$-CoFe bilayers," *Phys. Rev. B*, vol. 102, p. 140404, Oct 2020.

[150] J. Sort, K. S. Buchanan, V. Novosad, A. Hoffmann, G. Salazar-Alvarez, A. Bollero, M. D. Baró, B. Dieny, and J. Nogués, "Imprinting vortices into antiferromagnets," *Phys. Rev. Lett.*, vol. 97, p. 067201, Aug 2006.

[151] G. Salazar-Alvarez, J. J. Kavich, J. Sort, A. Mugarza, S. Stepanow, A. Potenza, H. Marchetto, S. S. Dhesi, V. Baltz, B. Dieny, A. Weber, L. J. Heyderman, J. Nogués, and P. Gambardella, "Direct evidence of imprinted vortex states in the antiferromagnet of exchange biased microdisks," *Applied Physics Letters*, vol. 95, p. 012510, July 2009.

[152] J. Wu, D. Carlton, J. S. Park, Y. Meng, E. Arenholz, A. Doran, A. T. Young, A. Scholl, C. Hwang, H. W. Zhao, J. Bokor, and Z. Q. Qiu, "Direct observation of imprinted antiferromagnetic vortex states in CoO/Fe/Ag(001) discs," *Nature Physics*, vol. 7, pp. 303–306, Jan. 2011.

[153] K. G. Rana, R. L. Seeger, S. Ruiz-Gómez, R. Juge, Q. Zhang, K. Bairagi, V. T. Pham, M. Belmeguenai, S. Auffret, M. Foerster, L. Aballe, G. Gaudin, V. Baltz, and O. Boulle, "Imprint from ferromagnetic skyrmions in an antiferromagnet via exchange bias," *Applied Physics Letters*, vol. 119, p. 192407, Nov. 2021.

[154] S. Jenkins, *Spin Dynamics Simulations of Iridium Manganese Alloys*. PhD thesis, University of York, 2020.

[155] L. Szunyogh, B. Lazarovits, L. Udvardi, J. Jackson, and U. Nowak, "Giant magnetic anisotropy of the bulk antiferromagnets IrMn and $IrMn_3$ from first principles," *Phys. Rev. B*, vol. 79, p. 020403, Jan 2009.

[156] G. Vallejo-Fernandez, N. P. Aley, L. E. Fernandez-Outon, and K. O'Grady, "Control of the setting process in CoFe/IrMn exchange bias systems," *Journal of Applied Physics*, vol. 104, p. 033906, Aug. 2008.

[157] J. M. D. Coey, *Magnetism and Magnetic Materials*. Cambridge University Press, Jan. 2001.

[158] J. D. Alzate-Cardona, D. Sabogal-Suárez, R. F. L. Evans, and E. Restrepo-Parra, "Optimal phase space sampling for Monte Carlo simulations of Heisenberg spin systems," *Journal of Physics: Condensed Matter*, vol. 31, p. 095802, Jan. 2019.

[159] P. F. Carcia, "Perpendicular magnetic anisotropy in Pd/Co and Pt/Co thin-film layered structures," *Journal of Applied Physics*, vol. 63, pp. 5066–5073, May 1988.

[160] K. O'Grady, L. Fernandez-Outon, and G. Vallejo-Fernandez, "A new paradigm for exchange bias in polycrystalline thin films," *Journal of Magnetism and Magnetic Materials*, vol. 322, pp. 883–899, Apr. 2010.

[161] R. J. Wakelin and E. L. Yates, "A study of the order-disorder transformation in iron-nickel alloys in the region $FeNi_3$," *Proceedings of the Physical Society. Section B*, vol. 66, no. 3, p. 221, 1953.

[162] L. Frangou, S. Oyarzún, S. Auffret, L. Vila, S. Gambarelli, and V. Baltz, "Enhanced spin pumping efficiency in antiferromagnetic IrMn thin films around the magnetic phase transition," *Phys. Rev. Lett.*, vol. 116, p. 077203, Feb 2016.

[163] X. S. Wang, H. Y. Yuan, and X. R. Wang, "A theory on skyrmion size," *Communications Physics*, vol. 1, p. 31, July 2018.

[164] B. Berg and M. Lüscher, "Definition and statistical distributions of a topological number in the lattice O(3) σ-model," *Nuclear Physics B*, vol. 190, pp. 412–424, Aug. 1981.

[165] A. Sakuma, K. Fukamichi, K. Sasao, and R. Y. Umetsu, "First-principles study of the magnetic structures of ordered and disordered Mn-Ir alloys," *Phys. Rev. B*, vol. 67, p. 024420, Jan 2003.

[166] H. Reichlová, V. Novák, Y. Kurosaki, M. Yamada, H. Yamamoto, A. Nishide, J. Hayakawa, H. Takahashi, M. Maryško, J. Wunderlich, X. Marti, and T. Jungwirth, "Temperature and thickness dependence of tunneling anisotropic magnetoresistance in exchange-biased Py/IrMn/MgO/Ta stacks," *Materials Research Express*, vol. 3, p. 076406, July 2016.

[167] L. Šmejkal, Y. Mokrousov, B. Yan, and A. H. MacDonald, "Topological antiferromagnetic spintronics," *Nature Physics*, vol. 14, pp. 242–251, Mar. 2018.

[168] L. Frangou, *Spin injection, transmission and detection in antiferromagnets*. PhD thesis, Université de Grenoble, 2017.

[169] A. Brataas, Y. Tserkovnyak, G. E. W. Bauer, and P. J. Kelly, *Spin pumping and spin transfer*. Oxford University Press, Dec. 2017.

[170] K. Harii, Z. Qiu, T. Iwashita, Y. Kajiwara, K. Uchida, K. Ando, T. An, Y. Fujikawa, and E. Saitoh, "Spin pumping in a ferromagnetic/nonmagnetic/spin-sink trilayer film: Spin current termination," *Key Engineering Materials*, vol. 508, pp. 266–270, Mar. 2012.

[171] S. M. S. Mizukami, Y. A. Y. Ando, and T. M. T. Miyazaki, "The study on ferromagnetic resonance linewidth for NM/80NiFe/NM (NM=Cu, Ta, Pd and Pt) films," *Japanese Journal of Applied Physics*, vol. 40, p. 580, Feb. 2001.

[172] Y. Tserkovnyak, A. Brataas, and G. E. W. Bauer, "Enhanced Gilbert damping in thin ferromagnetic films," *Phys. Rev. Lett.*, vol. 88, p. 117601, Feb 2002.

[173] Y. Tserkovnyak, A. Brataas, and G. E. W. Bauer, "Spin pumping and magnetization dynamics in metallic multilayers," *Phys. Rev. B*, vol. 66, p. 224403, Dec 2002.

[174] Y. Niimi, D. Wei, and Y. Otani, "Effect of magnetic fluctuations on spin current," *Journal of the Physical Society of Japan*, vol. 86, p. 011004, Jan. 2017.

[175] X. Liu, W. Zhang, M. J. Carter, and G. Xiao, "Ferromagnetic resonance and damping properties of CoFeB thin films as free layers in MgO-based magnetic tunnel junctions," *Journal of Applied Physics*, vol. 110, p. 033910, Aug. 2011.

[176] H. Chen, X. Fan, H. Zhou, W. Wang, Y. S. Gui, C.-M. Hu, and D. Xue, "Spin rectification enabled by anomalous Hall effect," *Journal of Applied Physics*, vol. 113, p. 17C732, May 2013.

[177] K. He, J. Cheng, M. Yang, Y. Zhang, L. Yu, Q. Liu, L. Sun, B. Miao, C. Hu, and H. Ding, "Spin rectification effect induced by planar Hall effect and its strong impact on spin-pumping measurements," *Phys. Rev. B*, vol. 105, p. 104406, Mar 2022.

[178] V. Flovik, F. Macià, A. D. Kent, and E. Wahlström, "Eddy current interactions in a ferromagnet-normal metal bilayer structure, and its impact on ferromagnetic resonance lineshapes," *Journal of Applied Physics*, vol. 117, p. 143902, Apr. 2015.

[179] K. Ando, Y. Kajiwara, S. Takahashi, S. Maekawa, K. Takemoto, M. Takatsu, and E. Saitoh, "Angular dependence of inverse spin Hall effect induced by spin pumping investigated in a $Ni_{81}Fe_{19}$/Pt thin film," *Phys. Rev. B*, vol. 78, p. 014413, Jul 2008.

[180] J.-C. Rojas-Sánchez, M. Cubukcu, A. Jain, C. Vergnaud, C. Portemont, C. Ducruet, A. Barski, A. Marty, L. Vila, J.-P. Attané, E. Augendre, G. Desfonds, S. Gambarelli, H. Jaffrès, J.-M. George, and M. Jamet, "Spin pumping and inverse spin Hall effect in Germanium," *Phys. Rev. B*, vol. 88, p. 064403, Aug 2013.

[181] Y. Ohnuma, H. Adachi, E. Saitoh, and S. Maekawa, "Enhanced dc spin pumping into a fluctuating ferromagnet near T_C," *Phys. Rev. B*, vol. 89, p. 174417, May 2014.

[182] P. C. Hohenberg and B. I. Halperin, "Theory of dynamic critical phenomena," *Rev. Mod. Phys.*, vol. 49, pp. 435–479, Jul 1977.

[183] R. Zhang and R. F. Willis, "Thickness-dependent curie temperatures of ultrathin magnetic films: Effect of the range of spin-spin interactions," *Phys. Rev. Lett.*, vol. 86, pp. 2665–2668, Mar 2001.

[184] A. Ghosh, S. Auffret, U. Ebels, and W. E. Bailey, "Penetration depth of transverse spin current in ultrathin ferromagnets," *Phys. Rev. Lett.*, vol. 109, p. 127202, Sep 2012.

[185] B. Gu, T. Ziman, and S. Maekawa, "Theory of the spin Hall effect, and its inverse, in a ferromagnetic metal near the Curie temperature," *Phys. Rev. B*, vol. 86, p. 241303, Dec 2012.

[186] D. Wei, Y. Niimi, B. Gu, T. Ziman, S. Maekawa, and Y. Otani, "The spin Hall effect as a probe of nonlinear spin fluctuations," *Nature Communications*, vol. 3, p. 1058, Sept. 2012.

[187] Y. Bitla and S. N. Kaul, "Mean-field treatment of nonlinear susceptibilities for a ferromagnet of arbitrary spin," *EPL (Europhysics Letters)*, vol. 96, p. 37012, Oct. 2011.

[188] S. Fujiki and S. Katsura, "Nonlinear susceptibility in the spin glass," *Progress of Theoretical Physics*, vol. 65, pp. 1130–1144, Apr. 1981.

[189] E. Wohlfarth, "The magnetic properties of alloys of Cobalt and Nickel with Palladium and Platinum," *The London, Edinburgh, and Dublin Philosophical Magazine and Journal of Science*, vol. 45, pp. 647–649, June 1954.

[190] J. Crangle and W. R. Scott, "Dilute ferromagnetic alloys," *Journal of Applied Physics*, vol. 36, pp. 921–928, Mar. 1965.

[191] A. P. Murani, A. Tari, and B. R. Coles, "Critical concentration for the onset of ferromagnetism in Pd-Ni alloys," *Journal of Physics F: Metal Physics*, vol. 4, pp. 1769–1781, Oct. 1974.

[192] J. Ododo, "The onset of ferromagnetism in PdFe and PdNi alloys," *Solid State Communications*, vol. 25, pp. 25–29, Jan. 1978.

[193] A. T. Aldred, B. D. Rainford, and M. W. Stringfellow, "Giant moments in PdNi alloys near the critical composition," *Phys. Rev. Lett.*, vol. 24, pp. 897–900, Apr 1970.

[194] S. Senoussi, I. Campbell, and A. Fert, "Evidence for local orbital moments on Ni and Co impurities in Pd," *Solid State Communications*, vol. 21, pp. 269–271, Jan. 1977.

[195] G. Iannone, D. Zola, A. A. Armenio, M. Polichetti, and C. Attanasio, "Electrical resistivity and magnetic behavior of PdNi and CuNi thin films," *Phys. Rev. B*, vol. 75, p. 064409, Feb 2007.

[196] D. Pham, R. Sugimoto, K. Oba, Y. Takeshita, F. Li, M. Tanaka, T. Yamashita, and A. Fujimaki, "Weak spin-flip scattering in $Pd_{89}Ni_{11}$ interlayer of NbN-based ferromagnetic Josephson junctions," *Scientific Reports*, vol. 12, p. 6863, Apr. 2022.

[197] T. S. Khaire, W. P. Pratt, and N. O. Birge, "Critical current behavior in Josephson junctions with the weak ferromagnet PdNi," *Phys. Rev. B*, vol. 79, p. 094523, Mar 2009.

[198] D. Bagguley and J. Robertson, "Ferromagnetic resonance and magnetic anisotropy in PdNi ($\sim$ 5 at %)," *Physics Letters A*, vol. 28, pp. 729–730, Mar. 1969.

[199] D. M. S. Bagguley and J. A. Robertson, "Resonance and magnetic anisotropy in dilute alloys of Pd, Pt with Fe, Co and Ni," *Journal of Physics F: Metal Physics*, vol. 4, pp. 2282–2296, Dec. 1974.

[200] E. Fawcett and R. C. Sherwood, "Magnetostriction of dilute magnetic alloys," *Phys. Rev. B*, vol. 1, pp. 4361–4367, Jun 1970.

[201] T. Harumoto, J. Shi, Y. Nakamura, and A. Takahashi, "Origin of large magnetostriction in Palladium Cobalt and Palladium Nickel alloys: Strong pseudo-dipole interactions between Palladium-Cobalt and Palladium-Nickel atomic pairs," *Applied Physics Letters*, vol. 118, p. 102401, Mar. 2021.

[202] S. Hashimoto, Y. Ochiai, and K. Aso, "Perpendicular magnetic anisotropy and magnetostriction of sputtered Co/Pd and Co/Pt multilayered films," *Journal of Applied Physics*, vol. 66, pp. 4909–4916, Nov. 1989.

[203] K. Binder and A. P. Young, "Spin glasses: Experimental facts, theoretical concepts, and open questions," *Rev. Mod. Phys.*, vol. 58, pp. 801–976, Oct 1986.

[204] O. Gladii, L. Frangou, A. Hallal, R. L. Seeger, P. Noël, G. Forestier, S. Auffret, M. Rubio-Roy, P. Warin, L. Vila, S. Wimmer, H. Ebert, S. Gambarelli, M. Chshiev, and V. Baltz, "Self-induced inverse spin Hall effect in ferromagnets: Demonstration through nonmonotonic temperature dependence in Permalloy," *Phys. Rev. B*, vol. 100, p. 174409, Nov 2019.

[205] O. Gladii, L. Frangou, G. Forestier, R. L. Seeger, S. Auffret, I. Joumard, M. Rubio-Roy, S. Gambarelli, and V. Baltz, "Unraveling the influence of electronic and magnonic spin-current injection near the magnetic ordering transition of IrMn metallic antiferromagnets," *Phys. Rev. B*, vol. 98, p. 094422, Sep 2018.

[206] S. Varotto, M. Cosset-Chéneau, C. Grèzes, Y. Fu, P. Warin, A. Brenac, J.-F. m. c. Jacquot, S. Gambarelli, C. Rinaldi, V. Baltz, J.-P. Attané, L. Vila, and P. Noël, "Independence of the inverse spin Hall effect with the magnetic phase in thin NiCu films," *Phys. Rev. Lett.*, vol. 125, p. 267204, Dec 2020.

[207] P. Nöel, *Dynamical spin injection and spin to charge current conversion in oxide-based Rashba interfaces and topological insulators*. PhD thesis, Université Grenoble Alpes,, 2019.

[208] K. Ando, S. Takahashi, J. Ieda, Y. Kajiwara, H. Nakayama, T. Yoshino, K. Harii, Y. Fujikawa, M. Matsuo, S. Maekawa, and E. Saitoh, "Inverse spin-Hall effect induced by spin pumping in metallic system," *Journal of Applied Physics*, vol. 109, p. 103913, May 2011.

[209] Y. Niimi, M. Kimata, Y. Omori, B. Gu, T. Ziman, S. Maekawa, A. Fert, and Y. Otani, "Strong suppression of the spin Hall effect in the spin glass state," *Phys. Rev. Lett.*, vol. 115, p. 196602, Nov 2015.

[210] S. Karube, T. Tanaka, D. Sugawara, N. Kadoguchi, M. Kohda, and J. Nitta, "Observation of spin-splitter torque in collinear antiferromagnetic RuO_2," *Phys. Rev. Lett.*, vol. 129, p. 137201, Sep 2022.

Résumé

Dans le domaine de la spintronique, au cours des dernières décennies, les aimants compensés sont passés d'un rôle passif à un rôle plus actif. Les progrès récents ont en effet permis de tirer profit de l'ensemble des propriétés spécifiques de ces matériaux uniques. Ils sont insensibles aux champs magnétiques, n'en créent pas, possèdent une dynamique magnétique ultra-rapide et génèrent de forts effets de transport électronique dépendant du spin. Par ailleurs, la présence des deux sous réseaux de spins qui composent les aimants compensés permet de nouvelles combinaisons de symétries et, de fait, de nouveaux phénomènes physiques, riches et souvent inattendus. Dans cette thèse, nous avons exploré en premier lieu les propriétés de magnétotransport de films épitaxiés de l'aimant compensé Mn_5Si_3. Il s'agit d'un possible matériau dit 'alter'magnétique - une nouvelle classe d'aimants compensés et colinéaires avec un décalage Zeeman de la structure de bande alternativement positif et négatif dans l'espace réciproque. La combinaison globale des symétries spatiales et temporelle de ce matériau permet l'émergence de nouvelles propriétés de magnétotransport que l'on pensait auparavant exclues pour les matériaux magnétiques compensés. Nous nous sommes focalisés sur l'étude de l'anisotropie non conventionnelle de ces propriétés, qui découle du lien complexe avec les symétries cristallines. Dans un deuxième temps, nous avons étudié les matériaux antiferromagnétiques, c'est-à-dire les aimants compensés avec une structure de bande dégénérée en spin. Plus spécifiquement, nous avons étudié leurs textures de spin, à savoir les skyrmions antiferromagnétiques. Ces textures de spin compensées présentent des symétries locales dans l'espace réel qui leur confèrent de nombreuses propriétés avantageuses par rapport à leurs analogues ferromagnétiques. À l'aide de simulations atomistiques, nous avons montré comment ces textures de spin locales peuvent être nucléées dans l'antiferromagnétique IrMn, par impression à partir d'un ferromagnétique. Enfin, nous avons utilisé une technique expérimentale, le pompage de spin, permettant d'étudier les propriétés spintroniques des aimants compensés et d'autres matériaux magnétiques au-delà des ferromagnétiques. Nous avons obtenus des résultats préliminaires sur l'étude des transitions de phase magnétiques à travers les fluctuations de spin non linéaires sur des films minces de PdNi montrant un comportement magnétique complexe. De manière générale, les résultats présentés dans cette thèse mettent en évidence des propriétés spintroniques uniques des aimants compensés qui vont au-delà de celles des ferromagnétiques conventionnels. Cette contribution ouvre des perspectives pour leur intégration dans les prochaines générations de dispositifs spintroniques.

Summary

In recent decades, the role of compensated magnets in the field of spintronics has shifted from a passive to more active one. This is due to the recent progress in harnessing the various beneficial and unique properties of compensated magnets, which include the vanishing net magnetization (robustness against perturbations by magnetic fields and production of no stray fields), ultrafast dynamics, and often large magneto-transport effects. Moreover, the sublattices with different magnetization orientations allow for novel combinations of symmetries and, in effect, for rich and often unexpected physical phenomena. In this thesis we first explore the magnetotransport properties of epitaxial films of Mn_5Si_3, which are a candidate material for altermagnets - a new class of compensated, collinear magnets with spin-split band structure. The global spatial symmetries of this material allow novel magnetotransport properties to emerge that were previously considered forbidden by the compensated magnetic ordering. Here, we study the unconventional anisotropy of these properties that arises from their intricate link to the crystal symmetries. We then shift focus to antiferromagnets, i.e. compensated magnets with spin-degenerate band structure, and their localized spin textures, namely antiferromagnetic skyrmions. These compensated spin textures have local symmetries that bring about numerous favorable properties. With the aid of atomistic simulations, we demonstrate how these local spin textures can be nucleated in a real antiferromagnet IrMn through imprinting from a ferromagnet. Finally, we discuss ferromagnetic resonance spin pumping - an experimental technique that allows studying the spintronic properties of compensated magnets and other magnetic materials beyond ferromagnets. We show preliminary results on probing magnetic phase transitions through non-linear spin fluctuations on thin films of PdNi showing complex magnetic behavior. The results presented in this thesis highlight the unique spintronic properties of compensated magnets that extend beyond those of conventional ferromagnets and can therefore adds to the growing support for their integration in a more active role the next generation spintronic devices.